Image Registration for Radiotherapy Applications

by
Niranjan Venugopal

Department of Physics

Submitted to the Faculty of Graduate Studies
in partial fulfillment of the requirements for the degree of
Master of Science

Faculty of Graduate Studies
University of Manitoba
Winnipeg, Manitoba, Canada

THE UNIVERSITY OF MANITOBA

FACULTY OF GRADUATE STUDIES

*****

COPYRIGHT PERMISSION

Image Registration for Radiotherapy Applications

BY

Niranjan Venugopal

A Thesis/Practicum submitted to the Faculty of Graduate Studies of The University of Manitoba in partial fulfillment of the requirement of the degree

Of

MASTER OF SCIENCE

UNIVERSITY OF MANITOBA
DEPARTMENT OF PHYSICS

CERTIFICATE OF EXAMINATION

Examining Committee

- Dr. John Lewis
- Dr. Gabriel Thomas
- Dr. Lawrence Ryner
- Dr. Gerald Gwinner
- Dr. Boyd McCurdy

The report by
Niranjan Venugopal

Entitled
Image Registration for Radiotherapy Applications

Is accepted in partial fulfillment of the
Requirements for the degree of
Master of Science

Date: June 18th, 2004 Chief Adviser: Dr. Boyd McCurdy

Abstract

Image registration is currently being used to assist in tumour target delineation in radiotherapy. Accurate delineation of the tumour volume ensures that the prescribed dose to the tumour volume is delivered correctly. Errors that are introduced in the image registration step will be propagated forward into the treatment planning, and ultimately into the patient's treatment. This thesis investigates three aspects of the image registration process as used in radiation treatment planning at CancerCare Manitoba: 1) Retrospective analysis of image registration methods, 2) Geometric uniformity measurements of computed tomography and magnetic resonance images of a quality assurance phantom, and 3) Implementation of a non-rigid registration technique to incorporate magnetic resonance spectroscopic (MRS) imaging data into clinical treatment planning.

In the retrospective analysis, digital image registration methods are compared to non-digital image registration methods and reveal that geometric misses of up to 35mm may occur. This is a significant result, considering treatment margins typically range from 5mm to 25mm. Significant improvement in the accuracy of the target delineation is observed using the digital image registration.

The geometric uniformity and fiducial registration errors are quantified to assess the image registration process currently used in radiation treatment planning. An acrylic phantom containing regularly spaced acrylic rods is used to assess these values for the computed tomography (CT) and magnetic resonance (MR) phantom image data. Average separation values of 3.00±0.02cm in the CT data set, and 2.98±0.10cm in the MR data set in the transverse direction compares closely to the 3.0cm design parameter. The fiducial registration error in the transverse direction was calculated to be 1.0±0.6mm. These results indicate sub-voxel accuracy of the image registration procedure.

Lastly, the use of a non-rigid registration algorithm is investigated to introduce MRS imaging into the radiation treatment planning of the prostrate. The average prostate volume reproduced by the algorithm was 99.5±0.8 cc, only 3.5 cc different than the gold standard (103.1cc). The variability in the algorithm application (±0.8 cc) is smaller than the intra-operator variability (±1.5cc). These results indicate that the proposed method is robust and demonstrates the feasibility of incorporating MRSI data into routine radiation treatment planning of the prostate.

Acknowledgements

I would like to take this opportunity to thank those people who have helped me along the way.

Firstly, I give my humble salutations to my spiritual teacher Bhagavan Sri Sathya Sai Baba. Without Him I would not have become the person that I have become today.

Equally, I give my highest regards to Dr. Boyd McCurdy ("Boss"). You live by example, and I hope to continue to learn from you, both as an academic, and as a human being. I am looking forward to our future work, and I hope that I can help you build the research program here at University of Manitoba.

I would also like to thank, Dr.'s Lawrence Ryner, Jew Bews, and John Lewis for giving insightful comments to this work. Also, many thanks to the dynamic duo: Dr.'s Andrej and Alex Hnatov. Your medical input and insight was crucial in the development of this thesis.

To my fellow graduate students, I also give my gratitude. Research can be tough at times, and it is the friendship of the students around you that helps you through those periods. Special thanks to Peter Potrebko, Ryan Rivest, Heather Andres, Eric Van Uytven, Keyvan Jabbari, and Huanjin Wu.

I thank my entire family for their constant support during my academic studies, especially over the last few years. Without your support and love I know I would not have made this far.

Lastly, I would to dedicate this work to my father, Mr. Selvakumar Venugopal who underwent prostate cancer treatment in 2003, and made an excellent recovery. Dad, you were an inspiration for me, and this research.

TABLE OF CONTENTS

ABSTRACT iii

ACKNOWLEDGEMENTS v

TABLE OF CONTENTS vi

LIST OF FIGURES x

LIST OF TABLES xiv

GLOSSARY OF TERMS xiv

CHAPTER 1

RATIONALE

1.1 Cancer Treatment with Radiation Therapy..... 1

1.2 The Basis of Radiation Therapy..... 2

1.3 Radiation Treatment Planning..... 4

1.3.1 Radiation Therapy Simulation 4

1.3.2 The Role of Diagnostic Imaging and Digital Image Registration 4

1.4 Role of Digital Image Registration in Radiation treatment planning 7

1.5 Rationale..... 8

CHAPTER 2

INTRODUCTION

2.1 Digital image registration 9

2.2 Methodology 10

2.3 Rigid and Affine Transformation 11

2.3.1 Rigid Transformation 11

2.3.2 Scaling Transformation 12

2.3.3 Affine Transformation 13
2.4 Non-rigid (non-linear) Transformations 14
2.4.1 Rigid versus Non-rigid registration 14
2.4.2 Techniques 15
2.4.3 Registration using Basis Functions 16
2.4.4 Registration Using splines 17
2.4.5 Thin-Plate Splines 18
2.4.6 Registration as an Optimization Problem 20
2.5 Fiducial Marker-Based Methods for Rigid and Non-rigid Applications 21
2.5.1 Fiducial Localization 22
2.5.2 Fiducial-Based Rigid Registration 24
2.5.3 Error Statistics in Fiducial-Based Rigid Registration 25
2.5.3.1 Fiducial Registration Error (FRE) 25
2.5.3.2 Target registration error (TRE) 26
2.6 Magnetic Resonance Imaging 29
2.6.1 The Imaging object 30
2.6.2 The MR Data Set 32
2.6.3 Magnetic Resonance Spectroscopy 34
2.6.3.1 Increasing the signal-to-noise ratio: The endorectal radio frequency coil 36
2.6.3.2 Spectroscopic data analysis 37
2.6.3.3 Clinical applications of Spectroscopy 38
2.6.3.4 MRS of the prostate 39
2.6.4 Summary 42

CHAPTER 3

DEVELOPMENT OF A PHANTOM FOR QUALITY ASSURANCE OF IMAGE REGISTRATION

3.1 Abstract 43
3.2 Introduction 43

3.3 Material and Methods 46
3.3.1 Phantom 46
3.3.2 Image acquisition 47
3.3.3 Image Registration 48

3.4 Analysis 48
3.4.1 Sagittal and Coronal images 48
3.4.2 Rod Center Acquisition 49
3.4.2.1 Filtering the background image 49
3.4.2.2 Center of Mass 51
3.4.3 Rod Spacing 52
3.4.4 Fiducial Landmark and Registration Error (FLE and FRE)..... 52
3.5 Results and Discussion 53
3.6 Conclusion 59

CHAPTER 4

FUSION IN RETROSPECT: A STUDY TO QUANTIFY THE EFFECT OF DIGITAL IMAGE FUSION IN RADIATION TREATMENT PLANNING OF BRAIN TUMOURS

4.1 Abstract 60
4.2 Introduction 61
4.3 Methods and Materials 63
4.3.1 Patient population 63
4.3.2 Image registration method..... 63
4.3.3 Target Delineation 64
4.4 Analysis 65
4.5 Results and Discussion 68
4.6 Conclusion 74

CHAPTER 5

FAST THREE DIMENSIONAL NON-LINEAR WARPING: TARGET LOCALIZATION OF INTRAPROSTATIC LESIONS USING MAGNETIC RESONANCE SPECTROSCOPIC IMAGES

5.1 Abstract 75

5.2 Introduction 76

5.3 Methods and Materials 78

5.3.1 Data Acquisition 78

5.3.2 Image registration method 79

5.3.3 Rigid Body Alignment 81

5.3.4 Target delineation and Intra-operator Variability 81

5.3.5 Control points selection 82

5.3.6 Non-rigid transformation/TPS algorithm 83

5.4 Analysis 84

5.4.1 Collected Data Summary 85

5.4.2 Evaluation of TPS algorithm 85

5.4.3 Intraoperator Variability 87

5.5 Results 87

5.5.1 Intraoperator variability 87

5.5.2 TPS algorithm Variability 90

5.6 Discussion and Conclusion 92

CHAPTER 6

SUMMARY

6.1 Conclusion 94

6.2 Future Work 97

REFERENCES 98

LIST OF FIGURES

Figure 1-1 The patient is positioned and consulted by the technologist prior to radiotherapy. 3

Figure 1-2 The *fused* image contains information from both imaging modalities 6

Figure 1-3 A simplified flow of the treatment planning process. Note that the image registration occurs before the tumour volume definition.....7

Figure 2-1 Example of different types of transformations of a square: (a) identity transformation, (b) rigid transformation, (c) affine transformation, and (d) non-rigid transformation. As adapted from[Ha02]..... 16

Figure 2-2 Example of a non-rigid transformation required to warp a square into a circle. The transformation is shown as two surfaces. (a) is defined as the displacement in the horizontal direction, and in (b) the displacement in the vertical direction. Adapted from [Ha02]. 17

Figure 2-3 Sample CT images of a prostate phantom and a fiducial marker.(Left: Full image, Right: Zoomed image) 23

Figure 2-4 This is a schematic diagram of a point based registration illustrating two types of error measurements. The black circles represent positions y_i in one space. The unfilled circles represent positions x_i in another space, after they have been mapped by a registering transformation T. The numbered positions are points used in the registration. The target registration error (TRE) is the registration at a point not used to effect the registration. The fiducial registration error (FRE) is the alignment error between two points and is used to effect the registration..... 27

Figure 2-5 (A) T1 weighted MR image, and (B) T2 weighted MR image of spinal cord. This figure illustrates the difference between T1 and T2 weighted images. (A) Cerebro-Spinal Fluid (CSF) appears black. (B) appears white. The background of the image (air) appears black in both images..... 31

Figure 2-6 A simple magnetic resonance spectrum showing the chemical shift between water and fat. As adapted from [Br82]..... 35

Figure 2-7 In (A) an image of the endorectal RF coil is shown. In (B) the endorectal coil is shown inserted, and inflated with approximately 100cc of air. The rectum is dilated approximately 5cm, and the prostate(highlighted by white contour)is pushed anteriorly..... 37

Figure 2-8 Pelvic anatomy (sagittal view). Note the location of the prostate behind the pubis between the bladder neck (superiorly) and the urogenital diaphragm (inferiorly) [Ca02]..... 40

Figure 2-9 (a) A T2-weighted axial image taken from a MR volume data set demonstrating a large tumor in the right midgland to base. The selected volume for spectroscopy (bold white box) and a portion of the 16x8x8 spectral phase-encode grid from one of eight axial spectroscopic slices is shown overlaid (fine white line) on (b) the T2-weighted image with (c) the corresponding 0.3 cm^3 proton spectral array. Spectra in (d) are regions of cancer that demonstrate dramatically elevated choline, and a reduction or absence of citrate and polyamines relative to (e) regions of healthy peripheral zone tissue [Ku02]. 41

Figure 3-1 On the left is a photograph of the QA phantom. On the right is a 3-D schematic of the phantom, showing the placement of the 3mm and 10mm diameter acrylic rods..... 47

Figure 3-2 In (A), a CT slice, I_{slice} , taken at the middle of the phantom is shown. The bright circular dots are the rods. A single region of interest is drawn around the rod, ROI_{rod}. In (B) the subtraction image, $I_{subtract}$, is shown without the ROI_{rod}'s. Finally in (C), the final image, I_{final}, contains only the ROI_{rod}'s. Alongside the images (A), (B), and (C), the surface plots of the regions just inside of plates of each image are illustrated..... 50

Figure 3-3 (A), (B), and (C) are Transverse, Sagittal, and Coronal mid-phantom images acquired with the MR scanner..... 51

Figure 3-4 The displacement between the rod centers, $|\vec{R}|$, is found by simple vector subtraction of $\vec{r}_1$, and $\vec{r}_2$. Thus $|\vec{R}| = |\vec{r}_1 - \vec{r}_2|$. Where $\vec{r}_1 = [x_1 - x_0, y_1 - y_0]$, and $\vec{r}_2 = [x_2 - x_0, y_2 - y_0]$. Subtracting the x and y coordinates alone is not satisfactory since the rods may not be exactly aligned with the imaging coordinate axes..... 52

Figure 3-5 The FRE is defined as the distance between the CT rod center location, and the transformed MR rod center location. In this figure, the rod centers are taken from the transverse slices of the MR and CT data sets. In this example, a slight systematic misregistration of ~1mm is apparent. The MR rod center locations are shifted in the negative x-direction..... 53

Figure 3-6 Spacing between rod centers in all three spatial directions for the CT image data set. 55

Figure 3-7 Spacing between rod centers in all three spatial directions for the MR image data set. 56

Figure 3-8 In (A) a histogram of the CT rod centers are presented in all three planes of view. Similarly in (B), a histogram of the MR rod centers are presented for all three planes of view. 57

Figure 3-9 The fiducial registration error (FRE) is presented for each rod for slices, in each plane of view. In the transverse view, there are 20 rods, while in the sagittal, and coronal view there are 16 rods. Rods are labeled left to right, top to bottom according to figure 3-3.....58

Figure 4-1 Maximum geometric miss as seen from the BEV. The geometric miss between the digital image fusion (dark grey) and non-digital image fusion (light grey) targets can clearly be seen. In this diagram both the maximum geometric miss(black) and normal tissue over irradiation(white) have been highlighted to show the method of measurement .(TM=Target Miss, NTO= Normal Tissue Over Irradiation)..... 67

Figure 4-2 **A:**The volumes of the GTV and PTV structures via each digital image fusion and non-digital image fusion methods. Study sets 1-13 represent MRI/CT fusion study sets. While Study sets 14-20 represent Infused-CT/Ct fusion study sets. **B:** Percent Volumetric difference GTV's and PTV's of digital image fusion and non-digital image fusion volumes..... 69

Figure 4-3 Spatial Shifts between digital image fusion and non-digital image fusion geometric centers. 70

Figure 4-4 **A:** A graph of the rotation angle vector(δ) versus the spatial shift between geometrical centers(mm). The rotation vector is defined as the root mean square of each azimuthal angle. **B:** A graph of the translation distance(λ) versus the spatial shift between geometrical centers(mm).....73

Figure 5-1 Sample images acquired from one patient. (A) The intensity mapping of the spectroscopy data overlaid on top of a T2 weighted MR image with endorectal coil inflated. (B), and (C) are two other data sets acquired during the MRS image acquisition. In image (B) the endorectal coil is inflated with ~100cc of air, while in (C) the endorectal coil is deflated. 79

Figure 5-2 Flowchart of the image registration method.....80

Figure 5-3 The images (A) and (B), are volumetric representations of the prostate GTV's. The GTV_{def}, is shaded in light grey, while the GTV_{inf} is shaded in dark grey. In (A) the prostate GTV's are not anatomically aligned. A 6mm shift in the superior/inferior direction aligns the anatomy of the prostate. Finally in (B) the two volumes are aligned anatomically.....81

Figure 5-4 The light grey represents the set of contours that make up the GTV_{def}, while the dark grey represents the contours making up GTV_{inf}. "•" and "▪" marks the spot of five example control points $\{X_I, Y_I\}$ that are selected from the GTV_{inf}, and then matched to the corresponding anatomical positions $\{X_0, Y_0\}$ on the GTV_{def}. 83

Figure 5-5 "+" marks the spot of the control points $\{X_I, Y_I\}$ that are selected from the MRS image set(inflated image) (A), and then matched to the corresponding anatomical positions $\{X_0, Y_0\}$ on the T2 weighted MR image (deflated image) (B). Once all control points are collected, a thin plate spline warping algorithm is applied to the inflated image to producethe corrected image in (C). In image (A) and (C), the white shaded region within the prostate represents the spectral overlay of increased choline/citrate. (An area in which there may be an intraprostatic lesion.) 84

Figure 5-6: To compare two MR slices at the same location, a region filling algorithm uniquely identifies each pixel within the contour. Taking the 'goldstandard' contour as the reference set, three unique identifiers are assigned to the difference image of the two filled contours. In (A) the volume of the gold standard is given a unique value of "2", while in (B) the corrected image is assigned a value of "1". The resultant difference of the two volumes gives (C). In (C) the light grey is the region of complete coincidence with values of "1". The regions in (C) that are white and black, are the regions of positive and negative discrepancies, respectively(i.e pixel values of "-1" and "2" respectively). These discrepancies correspond to regions of corrected prostate volume that are outside (white) and inside (black) the gold standard contour..... 86

Figure 5-7 In (A) the average volume per slice is presented for the deflated and inflated GTV's volumes. In (B) and (C), all 10 trial volumes per slice are presented for the inflated and deflated GTV volumes. 89

Figure 5-8 In (A) the total TPS volume is presented along with the volume of coincidence. Within error, the total coincidence volume is the same as the gold standard volume. The "gold standard" volumes particular reference volume that was chosen from the data set. In (B) the positive and negative discrepancies per trial are shown, and represents only a small percentage (~3-5%) of the total TPS volume. 91

LIST OF TABLES

Table 3-1 The average spacing between adjacent rod centers over all slices in the phantom for each particular plane of view. 54

Table 4-1 Histological classification and the type of digital image fusion used for each disease type. There a total of 20 study sets. Each study set contained the contours for GTV structure via both fusion and non-fusion techniques. 64

Table 4-2 Summary of the results obtained through the BEV analysis. The average maximum TM (target miss) represents the average maximum radial displacement between adjoining non-digital image fusion to digital image fusion edges over all fields in that particular treatment field geometry. Conversely, the average maximum NTO(normal tissue over irradiation) represents the average maximum radial displacement between adjoining non-digital image fusion to digital image fusion edges over all fields. The smallest and largest values over all fields for both type of measurement are listed for comparison. 71

Table 5-1 The results of the intraoperator variance were based on the result of a single RO contouring both the deflated and inflated prostate volumes 10 times. The TPS warping algorithm, utilizes the contour information based on the RO's prostate delineation, and was tested repeatedly 10 times to evaluate its accuracy. 90

GLOSSARY OF TERMS:

BPH — **B**enign **P**rostate **H**yperplasia. BPH is a common benign neoplasm (non cancerous enlargement of the prostate gland) in men, and has a high prevalence that increases with age. The increase in size of the prostate inside its capsule exerts pressure on the urethra, which passes through the capsule, resulting in obstruction to urine flow.

CT — **C**omputed **T**omography. A type of radiography in which a three-dimensional image of a body structure is constructed by computer from a series of plane cross-sectional images made along an axis.

CTV — **C**linical **T**arget **V**olume. Is a tissue volume that contains a demonstrable GTV and/or sub-clinical malignant disease that must be eliminated. The CTV can be described as including structures with clinical suspected but unproved involvement, in addition to an known tumour.

F.I.D. — **F**ree **I**nduction **D**ecay. A time-based electrical signal that is detected in a nuclear magnetic resonance spectrometer, that is produced by induction from the precessing magnetic moments of nuclei which have undergone a coherent quantum-mechanical spin transition caused by the application of a radiofrequency pulse.

FRE — **F**iducial **R**egistration **E**rror. Is defined as the root mean square (RMS) distance between corresponding fiducials after registration, has been used as feedback for point-based registration.

GTV — **G**ross **T**umour **V**olume. The gross demonstrable extent and location of the malignant growth. The GTV consist of primary tumour and metastases.

HDR — **H**igh **D**ose **R**ate. HDR brachytherapy involves placing very tiny plastic catheters into the prostate gland, and then giving a series of radiation treatments through these catheters, by temporarily inserting radioactive source (seeds). The catheters are then easily pulled out, and no radiactive material is left in the prostate gland.

Infused-CT — **I**nfused **C**omputed **T**omography. Another form of computed tomography, in which a contrast agent is intravenously injected into the blood stream to enhance the contrast of the anatomical structure or tumour of interest.

LDR — **L**ow **D**ose **R**ate. LDR brachytherapy is the implantation of small, weak radio-active radiation sources (seeds) directly into the prostate gland. As these seeds are only about 0.8 mm in diameter and 3.5 mm in length, the implantation is performed by injection through needles.

MRI	**M**agnetic **R**esonance **I**maging. Is the use of a nuclear magnetic resonance spectrometer to produce digital images of specific atoms, and molecular structures in solids especially human cells, tissues, and organs.
MRS	**M**agnetic **R**esonance **S**pectroscopy. A noninvasive technique that is similar to magnetic resonance imaging but uses a stronger field and is used to monitor body chemistry (as in metabolism or blood flow) rather than anatomical structures.
NTO	**N**ormal **T**issues **O**ver-irradiation. In the context of this work, is the amount of tissue that may have been exposed to radiation during a treatment session.
PET	**P**ositron **E**mission **T**omography. Tomography in which a computer-generated image of a biological activity within the body is produced through the detection of gamma rays that are emitted when introduced radionuclides decay and release positrons.
PTV	**P**lanning **T**arget **V**olume. A geometrical concept used for treatment planning and it defined to select appropriate beam sizes and beam arrangements, to ensure that the prescribed dose is actually delivered to the clinical target volume.
QA	**Q**uality **A**ssurance. A quality assurance program is the systematic monitoring and evaluation of the various aspects of a project, service, or facility to ensure that the standards of quality are being met.
TRE	**T**arget **R**egistration **E**rror. Is the distance between homologous points other than the fiducial centroids. TRE at a spatial position r, denoted $TRE(r)$, is the distance between this point and the corresponding point in the other space after registration.
US	**U**ltrasound. Is the use of ultrasonic waves for diagnostic or therapeutic purposes. Specifically to image an internal body structure, monitor a developing fetus, or generate localized deep heat to the tissues.

CHAPTER 1

Rationale

1.1 Cancer Treatment with Radiation Therapy

Radiation therapy is an important tool in the fight against cancer and is used in the treatment of approximately 50% of all cancer patients. In 2004, among Canadians, there will be an estimated 145,500 new cases of cancer and 68,300 deaths from cancer. The most common cancers in Canada continue to be breast cancer for women, and prostate cancer for men [Ca03]. Treatment options are determined by a multidisciplinary team, and depend's on the specific performance indicators (i.e. the type and stage of the cancer) of a particular patient. Often a combination of those treatments is used to obtain the best result. Radiation therapy is useful especially in cases where surgical removal of the cancer is not possible or when surgery might debilitate the patient (for example, when tumors are located close to the spinal cord).

Radiation therapy can be used following surgery to destroy any cancer cells that were not removed by surgery, or prior to surgery to "shrink" a previously inoperable tumor to a manageable size to enable surgical excision. Radiation can also be used to help relieve symptoms of advanced cancer (such as bleeding or pain), even if a cure is not possible. (i.e. palliative treatment) [Am03]

Radiation is energy in the form of high speed particles and electromagnetic waves. Radiation can be further classified as ionizing or non-ionizing. Ionizing radiation is radiation of high enough energy so that during an interaction with an atom, it can remove tightly bound electrons from their orbits, causing the atom to become charged or ionized (i.e. X-rays and electrons). Non-ionizing radiation is radiation without enough energy to

remove tightly bound electrons from atoms. (i.e. microwaves and visible light) High energy radiation can be used to treat cancer and other illnesses. Radiation can be delivered from outside of the patient using special machines (teletherapy) or deposited from radioactive substances inserted within the patient (brachytherapy). Combined with image guided treatment planning, radiation therapy is a powerful tool in the treatment of cancer, particularly effective when the cancer is detected at an early stage.

1.2 The Basis of Radiation Therapy

Radiation therapy uses high-energy x-rays (ionizing radiation) to stop cancer cells from dividing. The gray (Gy) is the scientific unit of measure of radiation energy dose equal to 1 joule/kilogram. A patient who receives radiation therapy as a treatment for cancer will receive typically several thousand centiGray (4500-7500 cGy) over a short period of time (4-7weeks). In comparison a typical diagnostic x-ray delivers far less dose. For example, modern mammography systems deliver approximately 2 to 3 mGy of dose per mammographic image.

Radiation therapy may be used to treat localized solid tumors, such as cancers of the skin, head and neck, brain, breast, prostate and cervix. Radiation therapy may be used to treat microscopic disease which is present but not detectable via clinical exam or diagnostic imaging.

Today, external beam radiation therapy is usually delivered by means of a linear accelerator. Linear accelerators use microwaves and waveguides to accelerate electrons to high energies (MeV's). These high energy electrons can be used to form an electron beam, or a photon beam (via bremsstrahlung interactions).

External beam radiation therapy typically uses x-rays, or photons to treat tumours at increased depth, while electrons may be used to treat shallower targets. The higher the

energy of the x-ray beam, the deeper the x-rays penetrate into the target tissue. Linear accelerators produce x-rays at various energies.

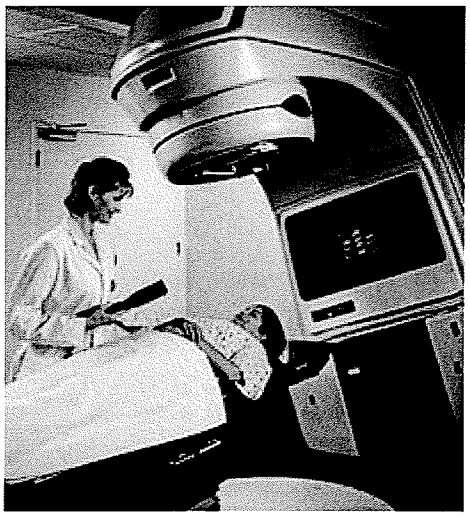

Figure 1-1 The patient is positioned and consulted by the technologist prior to radiotherapy.

Commercially available linear accelerators are able to rotate, delivering radiation from all angles. This is illustrated in figure 1-1. Multiple angles allow the maximum amount of radiation to be delivered to the tumor while minimizing the amount of radiation to the surrounding healthy tissue.

Radiation therapy may also be delivered by placing a small amount of radioactive material directly into the tumor (brachytherapy), either permanently (LDR), or temporarily (HDR). Some patients may receive both types of radiation treatment (external and brachytherapy).

1.3 Radiation Treatment Planning

1.3.1 Radiation Therapy Simulation

Before radiation treatment can begin, the intended treatment volume or target must be defined by the physician. This may be accomplished with a simulation machine- either a conventional simulator or a computed tomography (CT) simulator. The

conventional simulator can acquire planar x-ray images of diagnostic quality, and the physician identifies the target in relation to bony landmarks. The CT simulator can acquire a 3D volumetric image data set on which the physician may identify the target in 3D.

During simulation, the area of the patient's body to be treated is marked directly on the patient's skin with markers. Tiny permanent reference marks, or tattoos are sometimes made to ensure that daily treatments are delivered accurately. These are also useful for possible future treatment planning sessions and treatment updates.

In radiation therapy centers, radiation physicists and dosimetrists use computer software to plan the treatment. This computerized treatment planning allows the treatment to be delivered more accurately, both in terms of the "beam shape" that is achieved with precise collimation settings and in terms of the angles used to deliver the radiation to the target. The treatment planning software also incorporates a very accurate dose calculation algorithm which allows visualization of the radiation dose to be delivered to the patient. By using the computer tools to help "focus the x-ray beam," the radiation oncologist can deliver the radiation precisely to cancer, delivering a minimal amount of radiation to healthy tissues.

1.3.2 The Role of Diagnostic Imaging and Digital Image Registration

Computed tomography data is currently used for routine, three-dimensional (3D) planning of radiotherapy treatments. This x-ray based imaging modality offers two major advantages for this purpose: 1) it may be converted easily into electron density information, which is necessary for accurate dose calculations, and 2) it does not suffer from spatial distortions (e.g. geometrically uniform). While CT imaging provides excellent anatomical information in general, the images do not exhibit good soft tissue contrast. For this reason, secondary imaging modalities like magnetic resonance imaging (MRI) or infused-CT are often used in addition to the CT simulator data, to provide 3D image data with excellent soft tissue contrast. In many instances (especially the central nervous system including the brain), the tumor extent is much more readily visible in the

MRI images. However, it is somewhat difficult to incorporate the MRI data as the only imaging modality into the treatment planning process. MRI data are not related to physical densities, may suffer from spatial distortions, and slice thicknesses may be in error [Ho98]. Potentially distortions in the MRI data, may change the relationship between a displayed voxel and the part of the patient's body it represents [Ho98].

Historically, the radiation oncologist was forced to try to estimate the tumor outlines from MRI image data printed on film, and manually draw these onto the CT simulator data. Until September of 2001, this was the method that Radiation Oncologists at CancerCare Manitoba used to delineate tumor volumes. This process is very challenging, time consuming, and somewhat subjective. Additional difficulties arise due to changes in patient position between diagnostic image acquisition and CT simulation.

Over the last several years, digital image registration techniques have been vigorously researched as a possible solution to some of the problems mentioned above. Image registration (also known as image *fusion*) is a process by which an image data set is mathematically mapped onto another image data set in such a manner as to ensure anatomical coincidence. Usually rigid body transformations (e.g. translations, rotations) are used to match a reference image data set. Although many types of image fusion algorithms exist (e.g. landmark-based or intensity-based) in general these algorithms will attempt to minimize the difference measures that assess the quality of the fit, through an iterative process. This iterative process may be manual or automated. By mapping the alternate image data to the CT simulator data, the geometric and density qualities of the CT are retained, while the beneficial qualities of an alternate imaging modality may be utilized (i.e. excellent soft tissue contrast of the MRI.) Therefore, the combined data set may be used for improved tumor and critical structure delineation.

Several studies indicate that tumor localization using CT data alone (compared with fused CT-MRI data) results in widely varying tumor volumes and in an unacceptable rate of target misses [Ka97, Kh00, La97]. Therefore, the use of image fusion methods to incorporate alternate imaging modalities (i.e. MRI) into the treatment

planning process is crucial to accurate tumor delineation. The primary disease site for application of image fusion techniques is the brain [Kh00, Ko94, La97], but advantages have also been demonstrated for ocular tumors [Ho97], rectum [Ho98], and prostate [Ka97, La96]. Currently at CancerCare Manitoba nearly all patients receiving radiation treatment for brain tumors utilize image fusion to register an alternate image set (i.e. MRI study set or infused CT) onto the CT simulator image set. The fusion is performed manually by matching anatomical landmarks of the two imaging data sets using rigid body transformation tools. Figure 1-2 illustrates how image fusion combines the anatomy of the CT image and the soft tissue contrast of the MRI image. The final 'fused' image displays both image data sets.

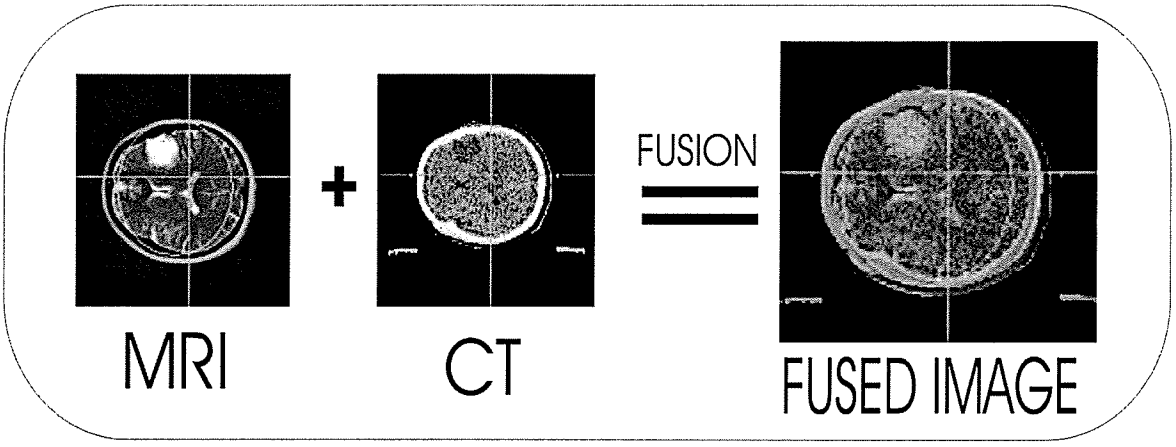

Figure 1-2 The *fused* image contains information from both imaging modalities

1.4 Role of Digital Image Registration in Radiation treatment planning

So how does image registration fit into the radiation treatment process? To recap the treatment planning process, consider the following flow chart, in figure 1-3.

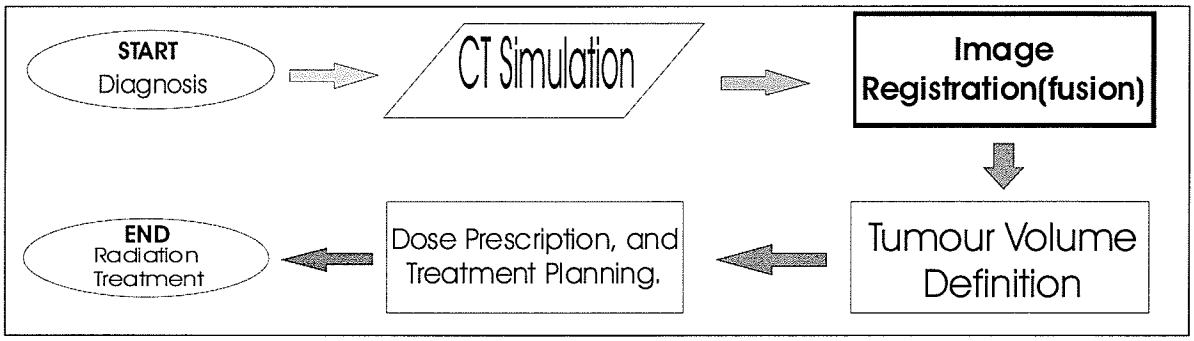

Figure 1-3 A simplified flow of the treatment planning process. Note that the image registration occurs before the tumour volume definition.

The treatment planning process may be broken down into six main steps. First there is the diagnosis, followed by a CT simulation. At the same time the physician may order secondary imaging sets, to provide additional diagnostic information to enhance tumour definition. Sometimes other diagnostic imaging data are acquired before a cancer diagnosis is made. Secondary imaging modalities that may be of interest could be Infused-CT, MRI, PET (positron emission tomography), or MRSI (magnetic resonance spectroscopic imaging) data. Following this, the secondary image data sets are registered to the primary data set (i.e. CT simulation data set). Using this secondary imaging information, the tumour volume is identified. Once the tumour volume is identified, treatment planning may be performed. When the treatment plan is finished, and checked for quality, the plan may be carried out and the patient receives customized radiation treatment.

1.5 Rationale

Since image registration is performed to assist in target localization, it is an absolutely critical step in the radiation treatment process. It is evident that this particular process be carried out with a high degree of accuracy, since any errors that are introduced in the image registration step will be propagated forward into the treatment planning, and ultimately in the patients' treatment.

This thesis is composed of three areas of investigation on issues surrounding the use of image registration in radiation treatment planning. In chapter 3, a phantom is presented to perform quality assurance checks. The phantom allows an evaluation of the geometric uniformity of CT and MRI images, and the registration error. Following in chapter 4, a retrospective study is performed to evaluate the effect of introducing digital image registration into the treatment planning of brain tumours at CancerCare Manitoba. Finally in chapter 5, the use of a non-rigid registration algorithm is investigated to introduce MRS imaging to the radiation treatment planning of the prostrate. In summary, this thesis evaluates the accuracy of past, current, and future modes of image registration as used in radiation therapy.

CHAPTER 2

Introduction

2.1 Digital image registration

In general, image registration is the process of geometrically mapping two or more imaging data sets so that corresponding anatomical features coincide.A key process of image registration is the determination of a geometrical transformation that aligns points of an object in one view with corresponding points in another view of either the same or another object [So01]. The term is also used in the context of aligning images with a computer model or aligning features in an image with locations in physical space [Ha02]. Image registration has application in many fields; the one addressed in this thesis is medical imaging, specifically for use in radiation treatment planning. Medical imaging deals with establishing shape, structure, size, and spatial relationships of anatomical structures within the patient, together with spatial information about function and any pathology or other abnormality. Establishing the spatial correspondence in medical images and equivalent structures in the body is fundamental to medical image interpretation and analysis. In many clinical applications, images from multiple modalities may be acquired and the physician's task is to mentally combine or "fuse" the information to draw useful clinical conclusions. This usually requires compensation for changes in subject position. Image registration geometrically aligns the images and so establishes correspondence between different features seen on different imaging modalities. It is also common for patients to be imaged dynamically, i.e. to have sequences of images acquired in real-time, often at many frames per second. This increases the amount of data, thus it is more desirable to relate one image to another to help extract relevant information. Intermodality registration enables the combination of complementary information from different modalities (i.e. MRI/CT, CT/PET, etc.), and intramodality registration enables accurate comparisons between images from the same modality (i.e. CT/Infused-CT).

2.2 Methodology

There are several types of registration algorithms in medical imaging, which can be classified as being either frame based, point landmark based, surface based, or voxel based. Stereotactic frame-based registration is very accurate and applied widely in image-guided neurosurgery, but requires substantial user interaction, and cannot be applied retrospectively. External/anatomical point landmark-based methods are usually labor-intensive and their accuracy depends on the accurate indication of corresponding landmarks in all modalities. Surface-based registration requires delineation of corresponding surfaces in each of the images. However, surface segmentation algorithms are generally highly data and application dependent and surfaces are not easily identified in functional modalities such as SPECT, etc. A major step forward in image registration came in the first half of the 1990s with the development of retrospective registration algorithms that were fully or virtually fully automated for both intramodality [Wo92] and intermodality registration [Wo93;Vi95;Co95;St96;St97;Ha02]. A significant breakthrough in the mid 1990s was the development of image alignment measures and registration algorithms based on entropy and, in particular, mutual information–measures first derived from the information theory developed by Shannon in 1948 [Sh48].

Another way to classify registration methods is to categorize them by complexity of geometrical transformations, which are mappings of points from the space X of one image set to the space Y of a second view. The transformation Γ applied to a point in X represented by the column vector x produces a transformed point x',

$$x' = \Gamma(x) \tag{2.1}$$

If the point y in Y corresponds to x, then a successful registration will make x' equal, or approximately equal, to y. Any nonzero displacement $\Gamma(x) - y$ is a registration error. The set of all possible Γ may be partitioned into rigid and non-rigid transformations with the latter transformations further divided into many subsets. This division makes sense for medical applications because some parts of the body are rigid , for example the

bone and the contents of the skull, while other parts of the body have a non-rigid nature, like the breast, pelvis, and thorax. Currently, registration algorithms commercially available from treatment planning vendors incorporate rigid body image registration, while considerable research activity in non-rigid registration has been ongoing in recent years.

2.3 Rigid and Affine Transformation

2.3.1 Rigid Transformation

Rigid transformation, or rigid mappings, are defined as geometrical transformations that preserve all distances. These transformations also preserve the straightness of lines (and the planarity of surfaces) and all nonzero angles between straight lines. Registration problems that are limited to rigid transformations are called rigid registration problems. Rigid transformations have two vector components of specification, a rotation and a translation. The translation is a 3D column vector t consisting of three components (t_x, t_y, t_z) relative to a set of (x, y, z) Cartesian axes. The rotation can be represented by orthogonal matrices in Cartesian coordinate system. With this convention, if Γ is rigid, then

$$x' = Rx + t \tag{2.2}$$

where R is a 3×3 orthogonal matrix, meaning that $R^tR = RR^t = I$ (identity). Thus $R^{-1} = R^t$, where t denotes the transpose. This class of matrices includes both the proper rotations, which describe physical transformations of rigid objects, and improper rotations, which do not. These latter transformations both rotate and reflect rigid objects. Improper rotations can be eliminated by requiring *det* $R = +1$, where *det* denotes the determinant.

Proper rotations can be parameterized in terms of three angles of rotation, $(\theta^x, \theta^y, \theta^z)$, around the respective Cartesian axes, the so-called "Euler angles". The rotation angle

around a given axis is typically considered positive if the rotation about the axis appears clockwise as viewed from the origin while looking in the positive direction along the axis. The rotation of an object (as opposed to the coordinate system to which it is referred) about the *x, y, z* axes, in that order leads to

$$R = \begin{pmatrix} \cos\theta_z & -\sin\theta_z & 0 \\ \sin\theta_z & \cos\theta_z & 0 \\ 0 & 0 & 1 \end{pmatrix} \begin{pmatrix} \cos\theta_y & 0 & \sin\theta_y \\ 0 & 1 & 0 \\ -\sin\theta_y & 0 & \cos\theta_y \end{pmatrix} \begin{pmatrix} 1 & 0 & 0 \\ 0 & \cos\theta_x & -\sin\theta_x \\ 0 & \sin\theta_x & \cos\theta_x \end{pmatrix} \tag{2.3}$$

with the three matrices representing the rotations $R_z(\theta_z)$, $R_y(\theta_y)$, and $R_x(\theta_x)$ about z, y, and x, respectively (in reverse order because they are applied from right to left). Other angular parameterizations are sometimes used, including all permutations of the order of R_x, R_y, and R_z.

2.3.2 Scaling Transformation

Scaling transformations contain both rigid and scaling components. Besides the 6 degrees of freedom of rigid transformations, scaling transformations have more, which are scaling factors in *X*, *Y* and *Z* directions respectively. They have following forms:

$$x' = RSx + t \tag{2.4}$$

$$x' = SRx + t \tag{2.5}$$

where $S = diag(s_x, s_y, s_z)$ is a diagonal matrix whose elements represent scale factors along the three coordinate axes. Because *RS* is not generally equal to *SR*, these equations represent two different classes of transformations. Such transformations may be needed to compensate for calibration errors in image acquisition systems. The diagonal elements of *S* then become the respective correction factors for the *x*, *y* and *z* gradients. If the scaling is isotropic, i.e. $s_x = s_y = s_z = s$, the transformation is a similarity transformation,

$$x' = sRx + t \tag{2.6}$$

where s is a positive scalar, sometimes known as a "dilation" (even for values less than 1). This transformation preserves the straightness of lines and the angles between them. The coupling of scaling with the rigid transformation is effective when registrations must account for erroneous or unknown scales in the image acquisition process.

2.3.3 Affine Transformation

The scaling transformations are special cases of the more general form affine transformation,

$$x' = Ax + t \tag{2.7}$$

in which there is no restriction on the elements a_{ij} of the matrix A. The affine transformation preserves the parallelism of lines, but allows angles between lines to change. It is an appropriate transformation class when the image may have been skewed during acquisition as, for example, when the CT gantry angle is incorrectly recorded. [Ha02]

The affine transformations and their associated special cases are sometimes represented by means of homogeneous coordinates. In this representation, both A and t are folded into one 4×4 matrix, M, whose elements are defined as follow : $m_{ij} = a_{ij}$, $i = 1, 2, 3...$, $j = 1, 2, 3...$ $m_{i4} = t_i$, $i = 1, 2, 3...$, $m_{4j} = 0$, $j = 1, 2, 3...$, *and* $m_{44} = 1$. To accomplish the transformation, augmented vectors u and u' are used for which $u_i = x_i$ and $x_{i'} = u_{i'}$ for $i = 1, 2,3$ and $u_4 = u_{4'} = 1$.

$$u' = \begin{pmatrix} u_{1'} \\ u_{2'} \\ u_{3'} \\ 1 \end{pmatrix} = Mu = \begin{pmatrix} a_{11} & a_{12} & a_{13} & t_1 \\ a_{21} & a_{22} & a_{23} & t_2 \\ a_{31} & a_{32} & a_{33} & t_3 \\ 0 & 0 & 0 & 1 \end{pmatrix} \begin{pmatrix} u_1 \\ u_2 \\ u_3 \\ 1 \end{pmatrix} \tag{2.8}$$

While the use of homogeneous coordinates does not produce any extra power or generality for rigid transformation, it does simplify notation.

2.4 Non-rigid (non-linear) Transformations

2.4.1 Rigid versus Non-rigid registration

For many medical applications rigid transformations are sufficient to describe the spatial relationship between two image data sets. An example of this are rigid body transformations between two brain imaging data sets. The skull provides naturally rigidity, thus the brain does not undergo large non-linear distortions. Although many applications can be handled by rigid body equations, there are cases where non-rigid transformations are utilized to better describe the relationship between two image data sets. For example in intrasubject registration, non-rigid transformations are required to account for tissue deformations that might occur over time. In this thesis, they are used to account for the deformation the prostate undergoes during an MRSI imaging sequence. In contrast to rigid body techniques, non-rigid registration techniques are still the subject of significant ongoing research activity. The purpose of this section is to give an overview of non-rigid transformation, and in particular the use of thin plate splines.

2.4.2 Techniques

Any non-rigid transformation method can be described by three components:

1. A transformation which relates the target and source images.
2. A similarity measure which quantifies the similarity between the target and source.
3. An optimization which determines the optimal transformation parameters as a function of the similarity measure.

The main difference between rigid and non-rigid registration techniques is the nature of the transformation. The goal of rigid transformation is to find the six degrees of freedom (3 rotational and 3 translational) of transformation $\Gamma:(x,y,z) \rightarrow (x',y',z')$ which maps any point in the source image to the corresponding point in the target image. As previously defined in section 2.3.3, the extension of this model is the affine transformation, which has 12 degrees of freedom, and allows for scaling and shearing:

$$\Gamma(x,y,z) = \begin{pmatrix} x' \\ y' \\ z' \\ 1 \end{pmatrix} = \begin{pmatrix} a_{00} & a_{01} & a_{02} & a_{03} \\ a_{10} & a_{11} & a_{13} & a_{14} \\ a_{20} & a_{21} & a_{22} & a_{23} \\ 0 & 0 & 0 & 1 \end{pmatrix} \begin{pmatrix} x \\ y \\ z \\ 1 \end{pmatrix} \tag{2.9}$$

Affine transformations are generally used for registration of images for which both structures follow a rigid pattern, or there are enough anatomical landmarks to align the images accurately [Co94]. By adding additional degrees of freedom, a linear transformation model such as that defined by equation 2.9, can be extended to a nonlinear transformation model. Figure 2-1 demonstrates the progression to higher order transformations (i.e. linear to nonlinear) on a simple square field.

In a similar manner it is possible to construct even higher order transformations such as, third order (60 degrees of freedom) and fourth order (105 degrees of freedom)

[Wo98]. Despite the larger number of degrees of freedom as we increase the order, the parameters only model global changes and cannot account for local distortions. Thus, linear quadratic models are quite limited in the ability to recover anatomical shape variability. As well, higher order polynomials tend to introduce artifacts such as oscillations, and consequently are not used for non-rigid transformations [Sz94] .

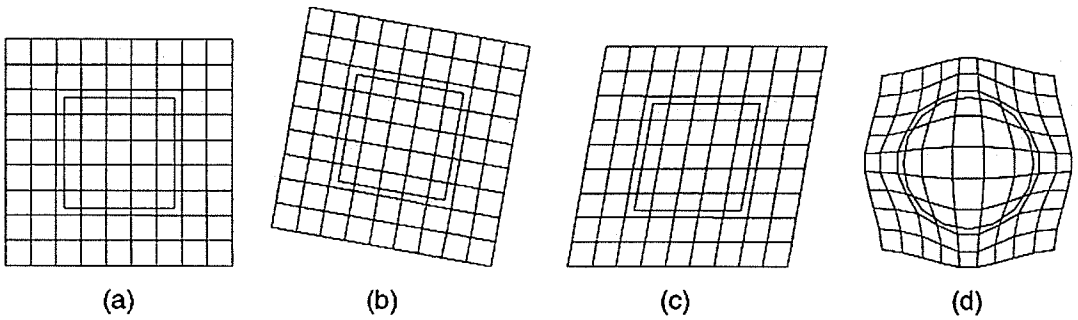

Figure 2-1 Example of different types of transformations of a square: (a) identity transformation, (b) rigid transformation, (c) affine transformation, and (d) non-rigid transformation. As adapted from [Ha02].

2.4.3 Registration using Basis Functions

Instead of using polynomials (as linear combination of higher order terms), a linear combination of basis functions θ_i may be used to describe the deformation field:

$$\Gamma(x,y,z)=\begin{pmatrix} x' \\ y' \\ z' \\ 1 \end{pmatrix}=\begin{pmatrix} a_{00} & \cdots & a_{0n} \\ a_{10} & \cdots & a_{1n} \\ a_{20} & \cdots & a_{2n} \\ 0 & \cdots & 1 \end{pmatrix}\begin{pmatrix} \theta_1(x,y,z) \\ \vdots \\ \theta_n(x,y,z) \\ 1 \end{pmatrix} \tag{2.11}$$

A common choice is to represent the deformation field using a set of (orthonormal) basis functions such as Fourier (trigonometric) basis functions or wavelet basis functions [Am91, As99]. In the case of trigonometric basis functions this corresponds to a spectral

representation of the deformation field where each basis function describes a particular frequency of the deformation.

2.4.4 Registration Using splines

A spline is a smooth function which interpolates a surface that is fixed at the landmark points at a specific height. If one imagines this surface as a thin metal plate, then this plate will take a shape in which it is least bent. For example, a 2D transformation can be represented by two series of surfaces whose height above the plane corresponds to the displacement in the horizontal or vertical direction. An example of such a transformation can be seen in figure 2-2.

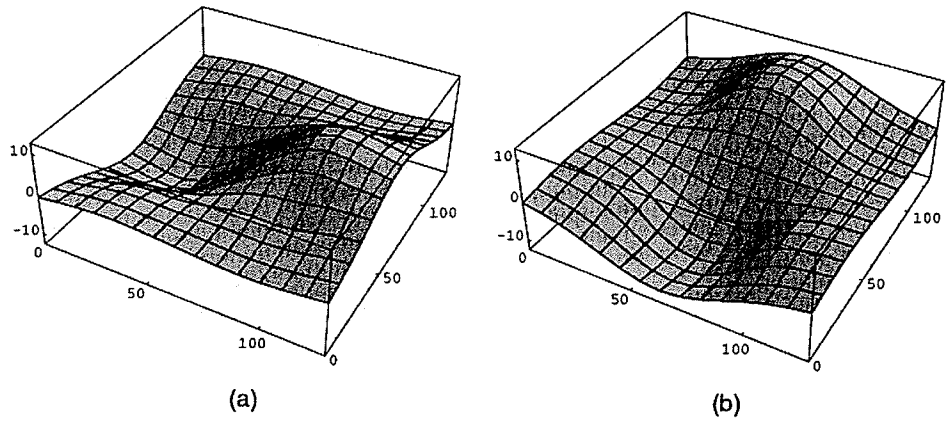

Figure 2-2 Example of a non-rigid transformation required to warp a square into a circle. The transformation is shown as two surfaces. On the left, in (a), the surface plot is defined as the displacement in the horizontal direction, and in (b) the surface plot of the displacement in the vertical direction. Adapted from [Ha02].

Many registration techniques using splines are based on the assumption that the set of corresponding points can be identified in the source and target images. This is analogous to the use of landmarks for rigid or affine registration methods. The corresponding points are often referred to as *control points.* At the control points, spline based transformations interpolate the displacements which are necessary to map the

location of control points in the target image into their corresponding counterpart in the source image. Between control points, the construct is a smoothly varying displacement field. The interpolation condition can be written as,

$$T(\phi_i) = \phi_i' \quad i = 1,...,n \tag{2.12}$$

where $T(\phi_i)$ is the transformation of ϕ_i , and ϕ_i denotes the location of the control points in the target image and ϕ'_i denotes the corresponding control points in the source image. Determination of the control points can vary. Generally in clinical situations, anatomical or geometrical landmarks which can be identified in both images may be used to define the spline based mapping function. This function would then map the spatial position of the landmarks in the source image into their corresponding position in the target image [Bo91]. As well, Meyers *et al* [Me97], suggested updating the location of control points by optimization of voxel similarity measures such as mutual information. In addition, control points can be arranged with equidistant spacing across the image, forming a regular mesh. In the latter, the control points are used in a parameterization of the transformation and do not correspond to anatomical landmarks. They are sometimes referred to as *pseudo-* or *quasi*-landmarks.

2.4.5 Thin-Plate Splines

Thin-plate splines are part of a family of splines that are based on radial basis functions. They have been formulated by Duchon [Du76] and Meinguit [Me79] for surface interpolation of scattered data. In recent years they have been widely used for image registration. The radial basis function splines can be defined as a linear combination of n radial basis functions $\theta(s)$.

$$t(x,y,z) = a_1 + a_2 x + a_3 y + a_4 z + \sum_{i=1}^{n} b_i \theta(|\phi_i - (x,y,z)|) \tag{2.13}$$

The transformation is defined as three separate thin-plate spline functions $T=(t_x, t_y, t_z)^T$, which returns a mapping between images. The coefficients a characterize the affine part of the spline-based transformation, while the coefficients b characterize the non-affine part of the transformation. The conditions of the interpolation function defined in equation 2.12 form a set of $3n$ linear equations. To solve the $3(n+4)$ coefficients uniquely, 12 additional equations are required. The 12 equations confirm that the non-affine coefficients b sum to zero and their cross products with the x, y, z coordinates of the control points are also zero. In matrix representation this can written as,

$$\begin{pmatrix} \Theta & \Phi \\ \Phi^T & 0 \end{pmatrix} \begin{pmatrix} \vec{c} \\ \vec{d} \end{pmatrix} = \begin{pmatrix} \Phi' \\ 0 \end{pmatrix} \tag{2.14}$$

Here $\vec{d}$ is a 4×3 vector of the affine coefficients a and $\vec{c}$ is an n×3 vector of the non-affine coefficients b. Θ is the kernel matrix with $\Theta_{ij} = \theta(|\phi_i - \phi_j|)$. Using some algebra, we can solve for a and b, in which the resultant yields a thin-plate transformation. This will also interpolate the displacement at the control points.

Considering 2 and 3 dimensions, the radial basis function of the thin-plate spline is defined as:

$$\theta(s) = \begin{cases} |s|^2 \log(|s|) & in\ 2D \\ |s| & in\ 3D \end{cases} \tag{2.15}$$

Here s is defined as $s = \sqrt{x^2 + y^2 + z^2}$. Modelling deformations with thin-plate splines has a number of advantages. For instance, they can be used to incorporate additional constraints, such as rigid bodies, and directional restraints [Bo93]. More over they can be extended to approximating splines in which the degree of approximation at the land mark depends on the confidence of the land mark localizations[Ro96].

2.4.6 Registration as an Optimization Problem

Registration can be formulated as an optimization problem whose goal is to minimize an associated energy or cost function. The most general form of such a cost function is

$$C = -C_{similarity} + C_{deformation} \tag{2.16}$$

where the first term characterizes the similarity between the target and source images and the second term characterizes the cost associated with particular deformations.
Most of the non-rigid registration techniques discussed so far can be formulated in this framework. In this context, the similarity measure can be viewed as a likelihood term which expresses the probability of a match between the target and source images. The second term can be interpreted as representing *a priori* knowledge about the expected deformations.

The first term is the driving force behind the registration process, and aims to maximize the similarity between both images. The different similarity measures can be divided into two main categories: point based and voxel based similarity measures. Point-based similarity measures minimize the distance between features such as points, curves, or surfaces of corresponding anatomical structures or artificial markers, and requires prior feature extraction. In recent years, voxel-based similarity measures such as sums of squared differences, cross correlation, or mutual information, have become increasingly popular. These voxel-based similarity measures have the advantage that they do not require any feature extraction process.

The second term is often referred to as the regularization or penalty function which can be used to constrain the transformation relating the target and source images. In the case of rigid or affine transformation, i.e., linear transformation, this term is normally ignored. A variety of regularization models have been used, such as linear

elasticity model, Laplacian or membrane model, and the biharmonic or thin-plate model [Ha02]. The thin-plate model[Bo93][Ru99] has the following form:

$$\int_{-\infty}^{\infty}\int_{-\infty}^{\infty}\int_{-\infty}^{\infty}\left[\left(\frac{\partial^2 T}{\partial x^2}\right)^2+\left(\frac{\partial^2 T}{\partial y^2}\right)^2+\left(\frac{\partial^2 T}{\partial z^2}\right)^2+2\left[\left(\frac{\partial^2 T}{\partial x\partial y}\right)^2+\left(\frac{\partial^2 T}{\partial x\partial z}\right)^2+\left(\frac{\partial^2 T}{\partial y\partial z}\right)^2\right]\right]dxdydz \quad (2.17)$$

This model has an intuitive physical interpretation in that it approximates the energy of a thin plate of metal which is subject to bending deformations [Co53]. Courent [Co53] combined a similarity function based on normalized mutual information with thin plate regularization.

The foundation for a basic understanding in rigid and non-rigid types of registration has been laid in the preceding sections. Equally, it is important to define and discuss current methods in evaluation of image registrations. This allows us to evaluate current models, and put into perspective the clinical evaluation of image registration.

2.5 Fiducial Marker-Based Methods for Rigid and Non-rigid Applications

If some set of corresponding point pairs can be identified *a priori* for a given pair of images, the registration can be determined by computing a transformation that maps one set of points to the other. Often, externally attached markers maybe preferred to anatomical landmarks, since the former are independent of anatomy and may be used when applying automatic fiducial localization algorithms as described in the following sections. Such points, taken as being reliable for registration, are called 'fiducial points', simply or 'fiducials'. The fiducial point of an image marker is defined as its centroid and the determination of this position is called fiducial localization [Ma97]. A centroid of a fiducial image is the location of the geometrical center based on pixel intensity. The transformation that aligns the corresponding fiducials will then interpolate the mapping from points in one image to those in the other.

2.5.1 Fiducial Localization

The accuracy of fiducial-based registration depends only on the degree to which the chosen points correspond in the two images. However, it is generally not straightforward to identify a single voxel as the centroid, because one fiducial usually occupies several voxels, as Figure 2-3 indicates.

There are mainly two ways to identify the centroid [Ha02]. One is based on interactive visual identification. In this approach, the same operator is asked to select, n times, the voxel which best represents a certain fiducial. Then the average and variance of the selected positions are computed, which provides the centroid and fiducial localization error $< FLE^2 >$ of the certain fiducial, respectively (Note that the use of bold font indicate the vector displacement FLE and a normal font indicates the magnitude FLE).

$$< p >= \frac{1}{n} \sum_{i=1}^{n} p_i \tag{2.18}$$

$$< FLE^2 >= \frac{1}{n-1} \sum_{i=1}^{n} |p_i - < p >|^2 \tag{2.19}$$

where p_i represents the centroid identified by the operator for the i^{th} time, and $< p >$ is the mean value.

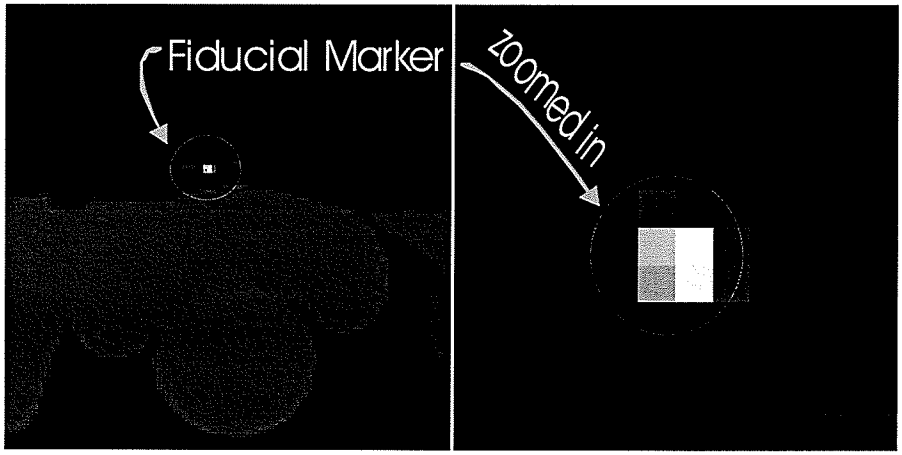

Figure 2-3 Sample CT images of a prostate phantom and a fiducial marker. (Left: Full image, Right: Zoomed image)

Another way to accomplish fiducial localization in MRI is by an intensity weighted automatic determination procedure [Wa96]. It has the advantage of being fully automated and taking into account the marker's physical size and shape to provide a consistent centroid. Briefly, the image is first searched for candidate markers. Then the neighborhood regions of the voxels of the candidate markers are divided into foreground (marker) and background voxels by thresholding. The set of foreground voxels that are three-dimensionally connected to the candidate voxel are identified by region growing, and an intensity weighted centroid of the foreground component is calculated as

$$x = \frac{\sum_{i}^{n} (I_i - I_o) x_i}{\sum_{i}^{n} (I_i - I_o)} \tag{2.20}$$

where voxel i, $i = 1\ 2, \ldots,$ n represent all voxels in current foreground component, I_i is the intensity of voxel i, I_0 is the intensity of "background" voxel, and x_i is the centroid of voxel i. The technique essentially finds the lowest threshold, such that the object formed from voxels whose intensities are higher than the threshold and are three-dimensionally connected to the candidate marker voxel is neither too small nor too large to be a marker. If it is not possible to find such a threshold, the candidate marker is identified as a false marker and rejected. The marker positions produced by the algorithm are then reviewed by a human operator.

2.5.2 Fiducial-Based Rigid Registration

In the case of rigid registration application, if FLE is reasonably small and the transformation correctly describes the motion of the object, the alignment of fiducials in the two images will lead to a small registration error for all points. Because of FLE, it is theoretically impossible to achieve a perfect alignment of fiducial points [Wa96]. The FLE of the fiducials in the two registered images is one standard to assess whether the registration is successful or not. A common measure of the overall fiducial misalignment, is the root-mean- square (RMS) error, called fiducial registration error, or FRE. FRE can be defined mathematically as follows. First, the individual fiducial registration error is defined as

$$FRE_i = \Gamma(x_i) - y_i \tag{2.21}$$

where x_i and y_i are the corresponding fiducial points in views X and Y . FRE is defined in terms of the magnitudes of the individual FRE_i.

$$FRE^2 = \frac{1}{N}\sum_{i}^{N} w_i^2 FRE_i^2 \tag{2.22}$$

where N is the number of fiducial points used in the registration and w_i^2 is a non-negative weighting factor, which may be used to decrease the influence of less reliable fiducials. For example, if $< FLE_i^2 >$ is the expected squared fiducial localization error for fiducial i, then an intuitive choice of w_i^2 is $1/ < FLE_i^2 >$.

If the transformation to be determined is constrained to be rigid, then Equation 2.22 can be written as [Ha02]:

$$FRE^2 = \frac{1}{N}\sum_{i}^{N} w_i^2 \mid Rx_i + t - y_i \mid^2 \tag{2.23}$$

Here R is rigid body transformations, and t is the translation previously defined in section 2.3.1. If the FLE_i are random errors with zero means and isotropic distributions for all fiducials, then an optimum registration can be achieved by minimizing FRE^2 with $w_i^2 = 1/ < FLE_i^2 >$. Therefore, we formulate the problem as finding R and t that minimize FRE^2 as calculated in Equation 2.23. The solution is unique unless the fiducials are distributed linearly (in which case FRE^2 is independent of rotations about the fiducial line). In 1987, Arun *et al.* [Ar87] proposed an algorithm to find R and t by least-square fitting two 3D point sets, an approach which has been widely applied [Ma97][Fi98][Ch02].

2.5.3 Error Statistics in Fiducial-Based Rigid Registration

Registration error is assumed to be randomly distributed over the entire image space. With this reasonable assumption, registration errors, mainly fiducial registration error can be predicted given a fiducial configuration. Inversely, the registration error statistics can serve as a guide in the fiducial configuration design to achieve an optimal registration result.

2.5.3.1 Fiducial Registration Error (FRE)

Fiducial registration error (FRE), is defined as the root mean square (RMS) distance between corresponding fiducials after registration, has been used as feedback for point-based registration since the late 1960s. In point-based rigid registration, FRE is defined as in Equation 2.24, where the rotation R and translation t minimize FRE. With the assumption that FLE_i is a random variable with isotropic, independent and identical probability distribution for all N fiducial markers, Sibson [So01] derived the relationship between FLE and FRE.

$$< FRE^2 >= (1-2/N) < FLE^2 > \qquad (2.24)$$

This result has important implications: (1) FRE is completely determined by FLE and the number of fiducial markers; (2) FRE is independent of fiducial configuration and global transformation (rotation and translation) between the two point sets. However, fiducial markers are generally not the points of interest. In medical applications, particularly cancer treatment, medical doctors are more concerned about the registration accuracy of the lesion region rather than that of any external fiducials. Thus, a more critical and direct measure is necessary.

2.5.3.2 Target registration error (TRE)

A more critical and direct measure of the registration error is target registration error *(TRE)*, the distance between homologous points other than the fiducial centroids [Fi98]. TRE at a spatial position r, denoted *TRE(r)*, is the distance between this point and the corresponding point in the other space after registration. The target can be any point in the space, and is commonly chosen from a region of interest, e.g., the lesion area. Fitzpatrick *et. al* [Fi98] found an approximate expression for $< TRE^2(r) >$, which exhibits the relationship between TRE and FLE.

$$< TRE^2(r) > \approx \frac{< FLE^2 >}{N}\left(1+\frac{1}{3}\sum_{k=1}^{3}\frac{d_k^2}{f_k^2}\right) \tag{2.25}$$

where f_k is the RMS distance of the fiducials from principal axis k in the coordinate system whose origin is at the centroid of the overall fiducial configuration (point x for image X and point y for image Y), and whose axes are parallel to corresponding axes in original images X and Y ; d_k is the distance of the target from principal axis k. See figure 2-4 for an illustrated example.

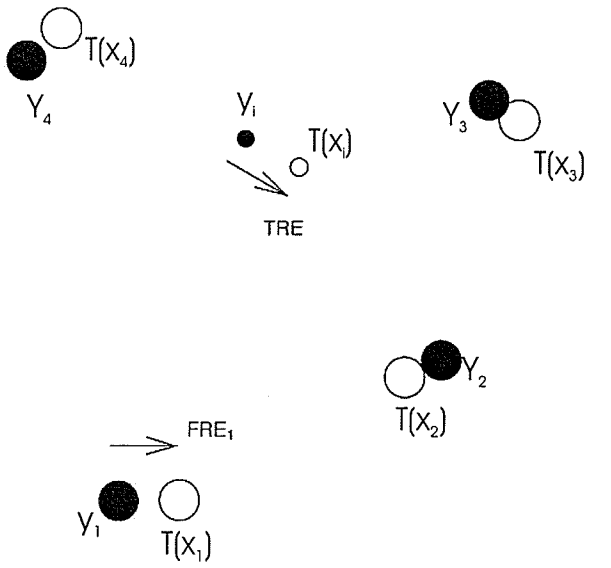

Figure 2-4 This is a schematic diagram of a point based registration illustrating two types of error measurements. The black circles represent positions y_i in one space. The unfilled circles represent positions x_i in another space, after they have been mapped by a registering transformation T. The numbered positions are points used in the registration. The target registration error (TRE) is the registration at a point not used to effect the registration. The fiducial registration error (FRE) is the alignment error between two points and is used to effect the registration.

Like $< FRE^2 >$, $<TRE>$ is proportional to $< FLE^2 >$, but unlike $< FRE^2 >$, it also depends on the fiducial configuration. It is this dependence that make TRE a more reliable measure than *FRE* for the point-based registration accuracy. From Equation 2.25, we can see that, for a given fiducial configuration the optimal position r for a target lies at the centroid of the configuration, where $d_k = 0$ for $i = 1,2,3$. At that position, the minimum $< TRE^2 >$ is achieved, which is $< FLE^2 > /N$. From the derivation of Equation 2.25, Fitzpatrick found that $< FLE^2 > /N$ arises from the error in the centroid of the fiducials, and that the remainder is the result of rotational error in fiducial configuration. Thus a target at the centroid of fiducial configuration is immune to rotational error in the transformation. As the distance $r = \sqrt{\sum_{k=1}^{3} d_k^2}$ of the target from the fiducial centroid increases, the rotational error increases, approaching r^2 dependence. The error also increases as the configuration of fiducials becomes smaller. In particular, suppose the shape of the configuration remains the same while its size is changed by some scaling

factor s. In this case, $\sum_{k=1}^{3} f_k^2$ increases as $(1/s)^2$, which leads to $\sum_{k=1}^{3} \frac{d_k^2}{f_k^2}$ increasing as $(r/s)^2$. For large r/s, $< TRE^2 >$ is approximately proportional to $(r/s)^2$.

We can also observe from Equation 2.25 that, if N is increased by adding additional fiducial points, the expected $N^{-1/2}$ dependence occurs when points are added such that their *RMS* distance to the three axes remains constant. For application purpose, we can briefly interpret Equation 2.25 as: (1) a fiducial configuration that lies close to one of its own principal axes, i.e., one which is almost colinear, will give rise to large *TRE* values at locations distant from the fiducial line; (2) isocontours of $< TRE^2 >$ are ellipsoidal and are centered at the centroid of fiducial configuration.

Fitzpatrick *et al* [Fi98], also derived another equation revealing the algebraic relationship between TRE, FRE, and FLE:

$$< FRE_i^2 >=< FLE^2 > - < TRE^2(\tilde{x}_i) > \tag{2.26}$$

where $< FRE_i^2 >$ denotes the expected value of FRE at fiducial point i, $\tilde{x}_i$ is the vector from the centroid of the overall fiducial configuration to fiducial i, and $< TRE^2(\tilde{x}_i) >$ is the expected value of TRE at that point. From Equation 2.19 we can see that TRE will be worst (largest) at the places where FRE is best (smaller), i.e., near pairs of fiducial points that are in close alignment.

Both Equations 2.25 and 2.26 serve as a warning that FRE is not a reliable merit for measuring registration accuracy, and as a guide in designing fiducial configuration for the purpose of image registration.

The FLE and TRE are useful quantities in determining the optimal registration between two data sets. Further more these quantities allow for specific calculations based on pixel intensity between two image data sets using fiducial landmarks. Currently most treatment planning software use only land mark based or mutual information techniques for image registration. The quantities are standards for measurement of registration error

in medical image registration. In this thesis, we will follow the standard conventions of registration error as applied to our quality assurance calculations in Chapter 3.

2.6 Magnetic Resonance Imaging

In the later part of this thesis, in particular chapter 5, extensive reference is made to magnetic resonance imaging (MRI) and as well as magnetic resonance spectroscopic (MRS) imaging. Thus, it is fitting to present basic background information about MR and spectroscopic data acquisition.

The magnetic resonance modality relies on the interaction that occurs between an extra magnetic field and the spin of the nucleus, or more specifically, the nuclear spin angular momentum. In the presence of an applied external field $\vec{B}_0$, nuclei containing unpaired nucleons (such as, ^{1}H, ^{13}C, ^{19}F, ^{23}Na, ^{31}P, and ^{39}K) tend to align themselves either with or against the magnetic field. In equilibrium, only slightly more of the nuclei align with, rather than against, the field but the large number of nuclei in a volume of material results in a measurable bulk magnetization. Although true mathematical descriptions of the nuclear spin require a quantum mechanical treatment, in this brief review, simpler classical characteristics of this system are used to describe the general signal acquisition for magnetic resonance spectroscopy.

The direction of the applied field is arbitrary. A coordinate system may be defined along the magnetic field, $\vec{B}_0 = B_0\hat{x}_3$, with $\hat{x}_3$, a unit vector in the x_3 direction. In most MR imaging systems, this field is aligned along the longitudinal axis of the patient. Because, $\vec{B}_0$ is time independent, it is commonly referred to as the static field. If the magnetization is taken out of alignment with $\vec{B}_0$, it will precess about the applied field with a frequency proportional to the field strength. That is, the frequency of the precession about the magnetic field is defined as, $\omega_0 = \gamma B_0$ where ω_0, is the Larmor

frequency, and γ is the gyromagnetic ratio. The gyromagnetic ratio depends on the nucleus, so that different nuclei precess at different frequencies in the same field.

The simplest magnetic resonance experiments consist of two basic steps [Pi00]. In the excitation step the magnetization established by the static field is tipped away from the alignment with $\vec{B}_0$. This is done through an applied time-dependent RF field $\vec{B}_1$. This field is often referred to as the *transverse field* because it is orthogonal to $\vec{B}_0$. The application of $\vec{B}_1$ creates a transverse component to the magnetization and tips away from alignment with $\vec{B}_0$ and aligns with the effective field.

Following the excitation step is the detection step. In this step the excitation field is turned off and nuclei are allowed to relax towards their initial state of alignment with $\vec{B}_0$. By Faraday's law of induction this precessing magnetization can be detected as a flux in a coil that is tuned to the frequency of this system.

All magnetic resonance experiments contain the above basic elements. However they typically have multiple excitations, multiple time intervals in which the spin systems are perturbed by gradient magnetic fields added to the main applied field, and possibly multiple time intervals in which the spin system is observed. The complete series of excitation/detection steps in MR experiments is referred to as a *pulse sequence.*

2.6.1 The Imaging object

The most abundant of the nuclei in the body that are studied by magnetic resonance methods are the protons associated with hydrogen. These are found primarily in water and are present in a number of other components in sufficient concentration to be detectable by MR. The MR quantities of primary interest are the spin density and the relaxation times T_1 and T_2. The spin density is denoted by N, and is defined as the concentration of spins per unit volume. The spin-spin relaxation, with time constant T_2, is known as the transverse relaxation, as it describes the relaxation transverse to the main

magnetic field. This results from the dephasing of spins as they precess at slightly different frequencies due to local differences in static field and spin-spin interactions. Spin-lattice relaxation, with time constant T_1, relates to the loss of energy from the spins to the environment and describes the component of the magnetization that is aligned with the applied field. From a medical perspective, it means that MR Imaging can provide multiple channels to observe the same anatomy. For instance, T1- and T2-weighted images of the same brain, will have different tissues appear differently in both images. White matter appears as light grey in T1 and dark grey in T2. Grey matter appears grey in both images. For example in figure 2-5 the Cerebro-Spinal Fluid (CSF) appears black in T1 and white in T2. The background of the image (air) appears black in both images.

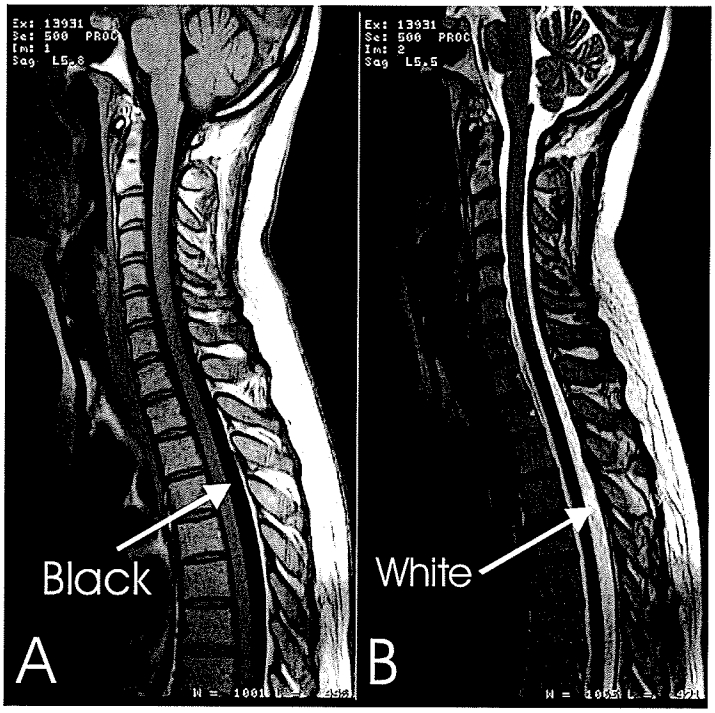

Figure 2-5 (A) T1 weighted MR image, and (B) T2 weighted MR image of spinal cord. This figure illustrates the difference between T1 and T2 weighted images. (A) Cerebro-Spinal Fluid (CSF) appears black. (B) appears white. The background of the image (air) appears black in both images.

The magnetization is a function of the proton density and relaxation times at each position. These quantities may change with time if there is significant patient motion. Therefore, the magnetization at each position x, and time t is defined as $\vec{M}(t,\vec{x})$. Also,

we define the transverse component of the magnetization, to be $\vec{M}_{\perp}(t,\vec{x})$. This is the component of the magnetization in the plane perpendicular to the direction of the static field. Further, this magnetization is the object being mapped to the data in all MR experiments, via induced currents in the detection coils.

2.6.2 The MR Data Set

Sonka *et al,* defines the data sample recorded in terms of the magnetic field, $\vec{M}(t,\vec{x})$:

$$\begin{aligned} g_m &= \int_{T,S} h_m(t,\vec{x})\vec{M}(t,\vec{x})dtd\vec{x} + n_m \\ &= \overline{g}_m + n_m \end{aligned} \qquad (2.26)$$

In this equation, $\overline{g}_m$ is the noise-free measured signal, n_m is the noise, in the m^{th} data element, and h_m is the sensitivity function that describes the linear transformation from object space to the data space [So01].

The random noise n_m results from the stochastic nature of the data set due the thermal and electronic noise in the measurement system. From our knowledge of thermodynamics, the MR detection system will suffer from thermal noise at equilibrium. This thermal noise turns out to be the dominant source of the fluctuations in a MR data set [Ed86]. The level of the thermal noise depends on the antennae, and the subject being imaged. The noise mechanism is usually well approximated by a Gaussian probability density function [Ed86]. Thus, the real and imaginary parts of each noise element n_m are often modeled by independent, uncorrelated Gaussian random variables.

We see from (2.26) that the measurements are discrete, linear functions of the magnetization. The sensitivity function, h_m, describes the response of the measurements system recorded at discrete sample m to the magnetization in the object at location $\vec{x}$ and time t_l. Thus it is a continuous-to-discrete mapping from object space to data space. The

function h_m, contains the sensitivity of the receiver coils, the demodulation of the high-frequency spin precession, any filtering applied to the data before sampling, and the finite temporal sampling window.

In all MR scanners, the transverse component of the magnetization is measurable. The sensitivity function is zero for $\vec{M}(t,\vec{x})\cdot\hat{x}_3 = \vec{M}_{\square}(t,\vec{x})$ and non-zero for $\vec{M}_{\perp}(t,\vec{x})$. In principle, one can solve for the magnetization analytically by using the Bloch Equations [Sl80] using vector notation:

$$\frac{d\vec{M}}{dt} - \gamma\vec{M}\times\frac{\vec{B}}{\mu} + \vec{D}\vec{M} = \vec{D}\vec{M}_0 \tag{2.27}$$

Where $\vec{M}_0$ is the initial magnetization, which is aligned with the static field $\vec{B}_0$. $\vec{B}/\mu$ is the total magnetic field, so it represents the static field, applied RF fields and any local fields resulting from the motion of the neighboring charges. Here μ is the permeability. The dissipation matrix $\vec{D}$, is given by:

$$\vec{D} = \begin{pmatrix} \frac{1}{T_2} & 0 & 0 \\ 0 & \frac{1}{T_2} & 0 \\ 0 & 0 & \frac{1}{T_1} \end{pmatrix} \tag{2.28}$$

The quantities in the *Bloch* equations, $\vec{D}$, $\vec{M}$, $\vec{B}$, and $\vec{M}_0$ are implicit functions of position and time. If the γ's and the applied magnetic field at previous times and locations are all known. The *Bloch* equations allow the determination of the magnetization $\vec{M}_0$, and the object-dependent relaxation times.

2.6.3 Magnetic Resonance Spectroscopy

The precession frequency of a nucleus in a magnetic field is proportional to the field strength. The electron cloud created by the chemical bonds in the immediate vicinity of any given proton affects the magnetic field that is experienced by its nucleus. These local field changes are small, but form the basis of MR spectroscopy (MRS).

An effective field at nucleus j can be expressed as,

$$\vec{B}_{eff} = \vec{B}_0(1-\sigma_j) \tag{2.29}$$

where σ_j is the chemical shielding constant for the nucleus j. The resulting precession frequency of nucleus j is then, $\omega_j = \gamma B_0(1-\sigma_j)$.

The resonance frequency of the water protons are different from the resonance frequency of fat protons. Other proton-containing metabolites are similiarly affected. In MRS, the frequency of the precession is used to unlock information about the chemical make-up of the object under study.

Spectroscopy capitalizes on the fact that each nucleus or functional group is associated with a unique ω_j. Spectroscopy experiments usually convert the difference between the local frequency ω_j and the frequency ω_r used in the detection system to the chemical shift δ_j, defined by:

$$\delta_j = \frac{\omega_r - \omega_j}{\omega_r} \tag{2.30}$$

which is measured in parts per million (ppm). The chemical shift is a useful parameter because it is independent of static field strength. Tables of the chemical shift for a

multitude of molecules of biological interest are readily available and have been published [Fr89].

Let us consider a simple but very common example of fat and water to exemplify spectroscopic data acquisition. This is illustrated in figure 2-6. This is a display of MR signal intensity on a relative frequency scale. This is a magnetic resonance spectrum. Following the normal conventions, the frequencies are expressed in (ppm) of the basic resonant frequency. This makes the scale independent of field strength. However, the actual difference in frequency between two compounds, in the units of Hertz, increase with field strength.

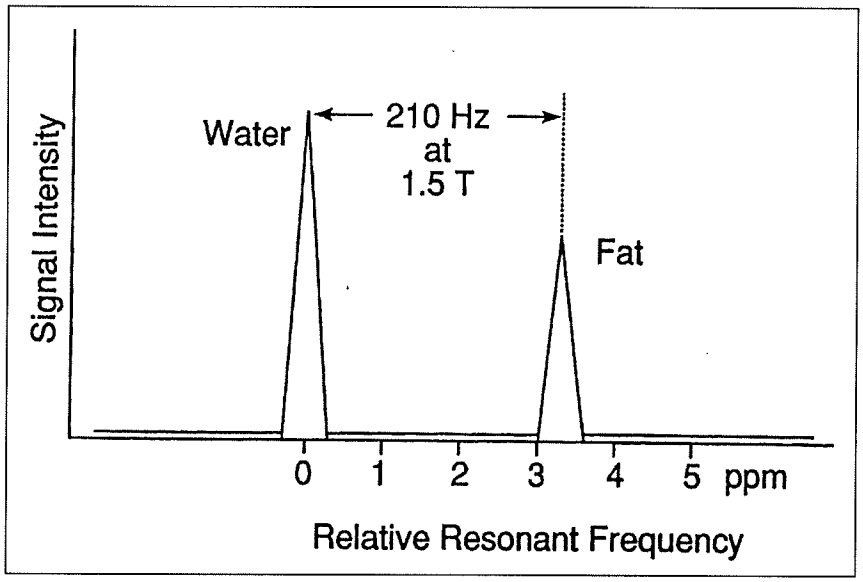

Figure 2-6 A simple magnetic resonance spectrum showing the chemical shift between water and fat. As adapted from [Br82].

The chemical shift between the major component of fat and water is approximately 3.3 ppm. At a field strength of 1.5T the protons have a basic resonant frequency of approximately 64 MHz. Multiplying this by 3.3 gives a water-fat chemical shift of approximately 210Hz. At a field strength of 0.5T the chemical shift would be only 70hz.

MRS analysis can be performed with any MRI system equipped with the necessary components and software, or with specifically designed laboratory systems. In general, spectroscopy requires high field strengths in order to produce more chemical shift separation between the chemical compounds and to increase signal strength.

2.6.3.1 Increasing the signal-to-noise ratio: The endorectal radio frequency coil

When an anatomical site is deep-seated within the body (i.e. prostate, rectum, cervix, etc.), achieving a high signal-to-noise ratio in MRI or MRSI may be difficult to achieve using standard external radio frequency (RF) coils. To overcome this problem, the use of internal RF coils is recommended [Pi00]. There are several types of internal RF coils that are commercially available for anatomical sites like the prostate, cervix, and rectum. In the context of this thesis, the endorectal RF coil designed for prostate MRS is of particular interest. The endorectal RF coil, as illustrated in figure 2-7a, is covered by a latex sheath to protect the coil upon insertion into the rectum. When it is inserted into the rectum, the latex sheath is filled with approximately 100cc of air. This extends the attached coil such that the coil is pressed against the prostate, alongside the rectal wall.

Although the endorectal RF coil is essential in spectroscopic data acquisition, it in turn deforms the prostate. In Chapter 5, this problem is addressed, as it relates to the image registration of magnetic spectroscopic images of the prostate with computed tomographics images used in radiation treatment planning.

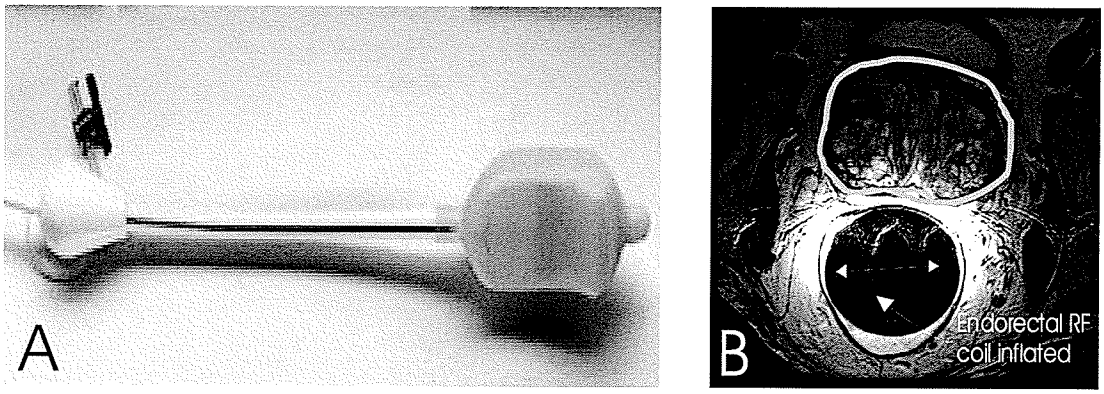

Figure 2-7 In (A) an image of the endorectal RF coil is shown. In (B) the endorectal coil is shown inserted, and inflated with approximately 100cc of air. The rectum is dilated approximately 5cm, and the prostate (highlighted by white contour) is pushed anteriorly.

2.6.3.2 Spectroscopic data analysis

With or without spatial localization, the goal in MR Spectroscopy is the determination of the concentrations of the J metabolites, their chemical shifts, and their relaxation behaviors. The problem is one, then, of solving an inverse problem to estimate these parameters using the data and a model for the forward problem.

There have been two major approaches used MRS data analysis. The first is to utilize the time-domain data directly. The most widespread of time-domain methods are the linear-prediction singular-value-decomposition method (LPSVD) and the variable projection method (VARPRO). These methods model the data as a sum of damped sinusoids with unknown phase, amplitude, and relaxation time. As early as 1985, estimation theory was used in this approach to incorporate *a priori* information, for example, the known chemical shift of metabolites being probed in the experiment [So01].

Alternatively, the data are Fourier transformed and estimation is done in the spectral domain. The essence of this approach is to assume a certain number of spectral peaks with known or estimated widths, chemical shifts, phases, and amplitudes [Pi00].

Temporal and spectral-domain approaches each have their advantages and draw backs. For example, limitations in the detection system often result in missing data at the beginning of the free induction decay FID, so metabolites with short relaxation times are very poorly sampled. At the tail end of the data collection process, sampling may terminate before a long-relaxation-time constituent is fully relaxed [So01]. These issues can be modeled in either domain, but their effects are localized in the time domain. Otherwise, the assumption of a set of exponentially-damped sinusoids and by some time-domain fitting methods can be incorrect, particularly when inhomogeneous tissue regions cause spatially-dependent susceptibilities. This can result in line broadening. Other real-world circumstances, like imperfect homogeneity of the static field, can also make the simple exponential model inapplicable. Also, multiplets arising from spin-spin coupling can be problematic [So01].

An advantage of the spectral-domain approach is that it allows the investigator to focus on subregions of the spectrum centered on chemical shift values of known interest, while avoiding spectra that are difficult to model. In particular, to obtain adequate dynamic range for the low-concentration molecules of interest, special frequency-selective excitation pulses are often used to suppress the water signal that would otherwise dominate the detection electronics [Fr89]. Estimation in the frequency domain can avoid the region where residual water signal resides. Fitting in the spectral domain also reduces the dimensionality of the estimation problem because there are typically fewer model parameters to fit [Pi00].

2.6.3.3 Clinical applications of Spectroscopy

In parallel with the ongoing investigation into methods for MRS data analysis, a body of information is accumulating on the biological applications of MRS. Proton MRS permits the acquisition of signals arising from many biological molecules. Long-echo-time sequences, such as those employing chemical shift imaging, can detect compounds that contain N-acetyl-aspartate (NAA), choline, the combination of creatine and phosphocreatine, and lactate. Short-echo-time sequences, typically single voxel techniques, can detect lipids, tryglicerides, alanine, glutamate, glutamine, scyllo-inositol,

glucose, myo-inositol, camosine, and histydine [Bo99]. Despite the long list of potential signals and pathologies for which some benefit has been found, success for Spectroscopy as a clinical tool has come on only a few fronts, for example, MRS of the prostate. Proton Spectroscopy also shows promise for determination of benign versus malignant disease in the prostate. Other nuclei besides ^{1}H can also be observed using MRS. The nuclei that have received the most attention in the biomedical literature are ^{13}C, ^{23}Na, and ^{31}P [So01]. While many studies of these nuclei have reported variations in metabolites with disease, these nuclei have not found their way into routine clinical applications at this time. More experience is still needed to determine the data acquisition and analysis strategies that will best utilize the yet-untapped potential of MRS.

2.6.3.4 MRS of the prostate

The addition of metabolic information from three dimensional MR spectroscopic imaging to anatomical data from MRI may allow more specific diagnosis and localization of prostate cancer. Magnetic resonance spectroscopy has been used to obtain metabolic data from tumors *in situ* [La96]. Recent technical developments have allowed the application of localized three-dimensional proton MR spectroscopic imaging to the *in vivo* evaluation of the human prostate, see illustration in figure 2.8. The prostate is a secretory gland that provides a significant proportion of the human male ejaculate. However, the normal prostate is not a homogeneous organ but is composed of several anatomic zones that differ in function and pathology. Human prostatic secretions contain high concentrations of citrate that are 240 to 1,300 times greater than blood plasma concentrations [Ca02]. Citrate production, secretion, and storage are associated only with prostatic glandular tissues, the majority of which (75%) are contained in the peripheral zone. This is the site for approximately 68% of all prostate cancers [Ca02].

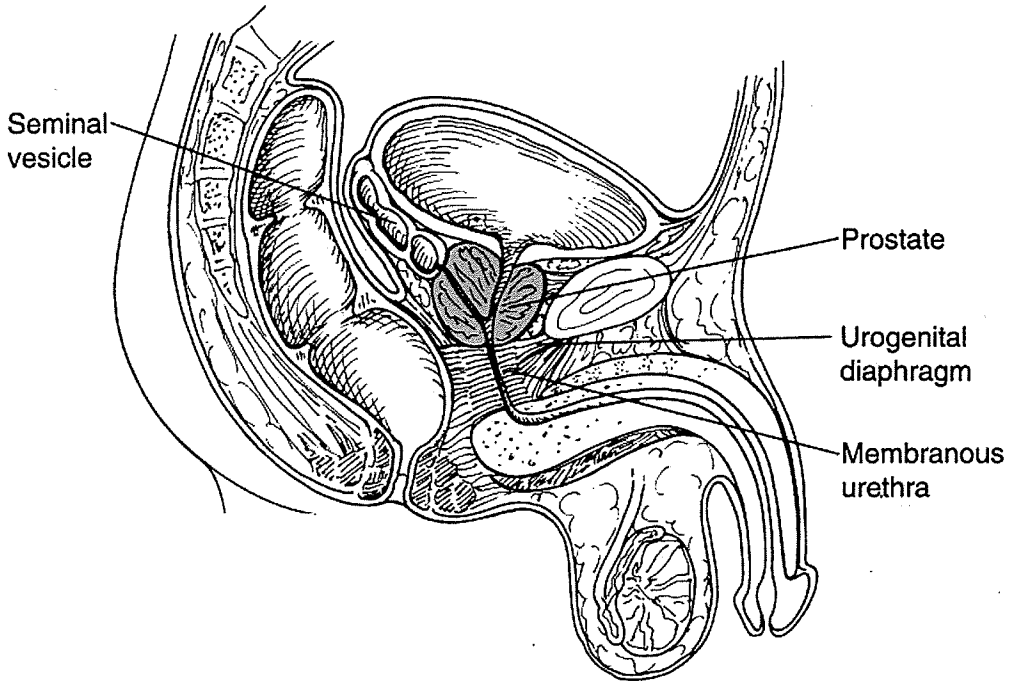

Figure 2-8 Pelvic anatomy(sagittal view). Note the location of the prostate behind the pubis between the bladder neck (superiorly) and the urogenital diaphragm (inferiorly) [Ca02].

High levels of citrate and intermediate levels of choline have been observed throughout the normal peripheral zone. In regions of cancer, two significant differences in metabolite levels have been observed: a significant increase in prostate choline levels relative to the normal peripheral zone and a significant reduction in prostate citrate levels [Ku02] (see figure 2-9). The decrease in citrate in prostate cancer is caused by both changes in cellular function and in the organization of the tissue. In prostate cancer, malignant epithelial cells have demonstrated diminished capacity for net citrate production and secretion. Also, cancer causes a great reduction in the volume of glandular ducts, which normally contain high levels of citrate.

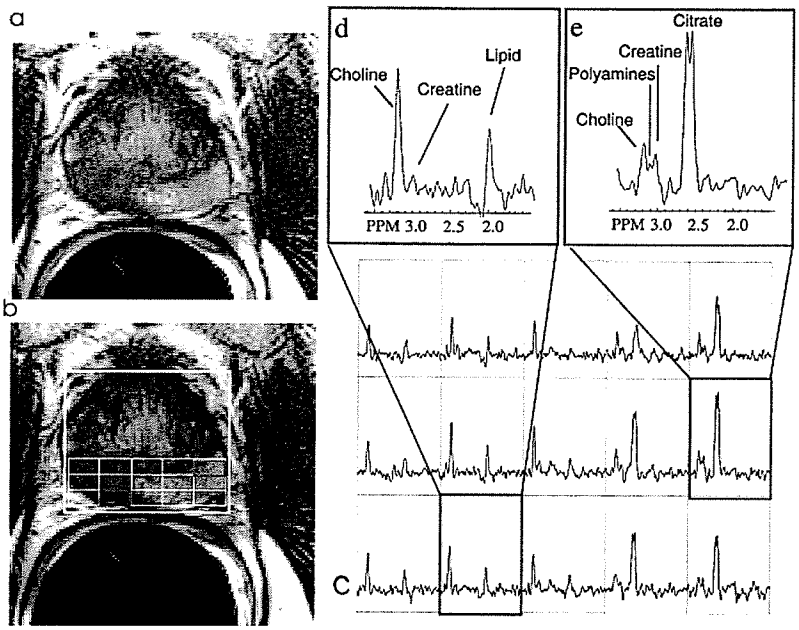

Figure 2-9. (a) A T2-weighted axial image taken from a MR volume data set demonstrating a large tumor in the right midgland to base . The selected volume for spectroscopy (bold white box) and a portion of the 16x8x8 spectral phase-encode grid from one of eight axial spectroscopic slices is shown overlaid (fine white line) on (b) the T2-weighted image with (c) the corresponding 0.3 cm^3 proton spectral array. Spectra in (d) are regions of cancer that demonstrate dramatically elevated choline, and a reduction or absence of citrate and polyamines relative to (e) regions of healthy peripheral zone tissue. [Ku02]

With the use of three-dimensional MR spectroscopic imaging, significantly higher choline levels and significantly lower citrate levels were observed in regions of cancer compared with areas of BPH (benign prostate hyperplasia) and normal prostatic tissue [Ku02]. The ratio of these metabolites (choline to citrate) in regions of cancer appears not to overlap with ratios in the normal peripheral zone, which suggests that three dimensional MR spectroscopic imaging combined with MRI may improve tumor detection and localization compared to MRI alone.

The combination that was most useful for excluding the presence of cancer in a volume (negative predictive value of 74 to 82%) was the absence of cancer with either MRI or MRSI. Magnetic resonance spectroscopy has been effective in discriminating residual cancer from necrosis and other residual tissues after cryosurgery. Magnetic resonance spectroscopic imaging information may also provide insight into tumor aggressiveness, which may lead to improved risk assessment in patients with prostate

cancer. Early biochemical studies have indicated that citrate levels in prostatic cancer are dependent on the grade of the tumour, with citrate levels being low in well-differentiated prostate cancers and effectively absent in poorly differentiated prostate cancer[Ku02]. More recent developments to improve MRI include contrast-enhanced fast dynamic MRI. On contrast- enhanced images, prostate cancer shows a typical early and rapidly accelerating enhancement compared with normal tissues [Ku02].

2.6.4 Summary

The basic theory utilized in this thesis has been presented in this chapter. One goal was to present and describe the mathematical framework for rigid and non-rigid body image registration techniques. Of particular interest, is the thin-plate-spline model. An important observation is that this type of interpolation allows for non-linear modeling of deformations. Thin-plate splines have a number of advantages. For instance, they can be used to incorporate additional constraints, such as rigid bodies, directional restraints [Bo93]. More over they can be extended to approximating splines in which the degree of approximation at the land mark depends on the confidence of the land mark localizations [Ro96]. In medical imaging processing, work carried out by Meyer *et al* [Me97], has set the precedence in using thin-plate-splines to account for deformation in the pelvic anatomical region. Based on this literature, computer code was generated to automate the image registration. A thorough review of image registration error was also presented. Knowledge of the error in the registration makes it possible to develop a quality assurance protocol for the image registration that is used clinically. Furthermore, this chapter was concluded with discussion relating to MRS imaging. Specifically, MRSI is a method to non-invasively determine staging and phenotype of prostate cancer. This area of diagnosis is now being used at some research centers for the radiation treatment planning of men with prostate cancer. With increased accuracy of modern radiation treatment techniques, intraprostatic lesions identified using MRS image data may be treated with higher dose. Chapters 3, 4 and 5, will present three areas of investigation, exploring past, present and current methods of image registration.

CHAPTER 3

Development of a phantom for Quality Assurance of Image Registration

3.1 Abstract

In this chapter, two calculations are performed to assess the quality of the image registration process used in clinical radiation treatment planning. Since the introduction of digital image registration techniques in 2001 at CancerCare Manitoba, there was a need to develop a method to evaluate the quality of the digital image registration process. To achieve this end, an acrylic phantom was designed and constructed in house. The phantom contains three regularly spaced perpendicular arrays of solid acrylic rods and was based on a similar phantom presented by Yu *et al* [Yu01]. The design parameter for the separation between rod centers was 3.0cm. To assess the geometric uniformity of the CT and MR phantom image data the distance between the rod center was calculated. Average values of 3.00±0.02 cm in the transverse CT data set, and 2.98±0.10 cm in the transverse MR data set indicate a high degree of geometric uniformity in the CT data and acceptable uniformity in the MRI data. Using standard techniques to calculate the image registration error, the fiducial registration error (FRE) was calculated. For the transverse direction the FRE, was calculated to be 1.0±0.6 mm, which indicates accuracy to within about one voxel.

3.2 Introduction

The use of 'phantoms' in the field of medical physics dates back to the beginning of the century. A phantom is an inanimate object that is used to help isolate or evaluate physical parameters during experimental measurements. In the 1920's, water tanks and

wax blocks were often used for x-ray experiments, and to this day these materials are still in use in certain applications. It was not until the 1960's however, that more reliable tissue substitutes and sophisticated phantoms began to appear [Wo93]. Since, that time, phantom technology has developed in step with medical imaging and treatment technology. Today, phantoms are made using a wide variety of available raw materials and processes. Various types of phantoms are used to test the performance of medical imaging equipment by mimicking the radiation attenuation and absorption properties of human tissue. They are also used to verify radiation dosage to be delivered during therapy, to calibrate equipment, and for research. They are an essential part of maintaining high standards in radiotherapy and diagnostic imaging through quality assurance (QA) and control programs.

In this chapter two calculations are performed to assess the quality of the image registration process that is used in the clinical radiation treatment planning at CancerCare Manitoba. Digital image registration methods were introduced clinically at CancerCare Manitoba, in September 2001. There was a need to design a QA process to evaluate the quality of the image registration. Currently the two most commonly used imaging modalities involved in image registration at this centre are computed tomography (CT), and magnetic resonance imaging (MRI) .

At CancerCare Manitoba, the brain is the most common anatomical site on which to apply image registration. The brain is an ideal site for application of rigid-body registration techniques, due to the rigid anatomical structure of the skull. In the brain, tumour enhancing compounds such as gadolinium may greatly increase the tumour visibility. Furthermore, the visualization of the tumour extent in the brain (and central nervous system) is better on the MRI. This is a direct result of the enhanced soft tissue contrast on MRI as compared to CT. However, MRI image acquisition is prone to a number of problems that may affect the integrity of the image data set. For example, inhomogeneities in the constant magnetic field, nonlinearity of the gradient field, linear scale errors, instrument imperfections, magnetic susceptibility artifacts, and local magnetization effects represent some of these problems [Ph91,Ba92, Su94].

Several researchers have investigated the accuracy of the image registration in various situations. A study performed by Kondziolka *et al* [Ko92] measured the vector distances between the target and the center of the stereotactic frame on axial and coronal MRI studies in which they found that the mean difference in measurement in the x axis was 1.19 mm and 1.55 mm in the y axis. Bednarz *et al* [Be99]. also reported similar average differences between CT and MRI coordinates using the a skull phantom. Walton *et al* [Wa96]. reported much larger errors, up to 2.7 mm for the x axis, 7.0 mm for the y axis, and 8.0 mm for the z axis in a MR phantom study. Furthermore, they reported that more accurate stereotactic localization could be achieved using a three-dimensional image data set.

In another recent study, Orth *et al* [Or99] reported on the geometric accuracy of manually registering MR image data with CT image data. They found differences in fiducial marker positions of 1.99 mm in the anterior/posterior or the y direction. These were correlated with differences in intraphantom target positions (up to 1.97 mm in the same direction) and suggested that improper fiducial rod identification and the subsequent transformation to stereotactic coordinate space were the greatest sources of spatial uncertainty.

In this study, a custom acrylic phantom designed for both MRI and CT scanners was constructed to evaluate the geometrical accuracy of registering CT and MRI data sets and to determine the error using rigid body registration techniques currently available in the treatment planning software.

3.3 Material and Methods

3.3.1 Phantom

The phantom was manufactured in-house by the Medical Devices Section of the Department of Medical Physics at CancerCare Manitoba (CCMB). It consisted of a hollow cube with an outer dimension of 164±1 mm. The phantom is illustrated in Fig. 1. The phantom contains three perpendicular arrays of solid acrylic rods, placed along the three panels of the cube labeled A, B, and C. Two sizes of acrylic rods were used, one with a 3mm diameter, and a second size with a 10mm diameter. The distance between the centers of the rods along each dimension was designed to be a constant 30mm separation. All the rods, and edges of each plate can be used as markers for the registration of the MR to CT image data sets. There were 16 rods in panels A and B. In panel C, there were 20 rods. On panels A and B, 4 rods had a diameter of 10 mm, and 12 rods had a diameter of 3 mm. Similarly on panel C, 5 rods had a diameter of 10 mm, and 15 rods had a diameter of 3 mm. Using rods of different thicknesses allows the user to easily manipulate image orientation during the image registration. An additional design feature of the phantom is the ability to hold water.

The thickness of the six plates for the phantom was 12.7±1.0 mm. This thickness was felt to be strong enough to keep all the rods and plates in their correct positions during the image acquisition. The phantom has an inner dimension of 136±2 mm. During the CT acquisition the phantom was not filled with water, while during the MR acquisition, the phantom was filled with water. When imaged using CT, the contrast between air and the acrylic rod is good. However, when imaged using MR, water is needed to provide image contrast between the acrylic rods(which actually do not provide signal) and the surrounding volume.

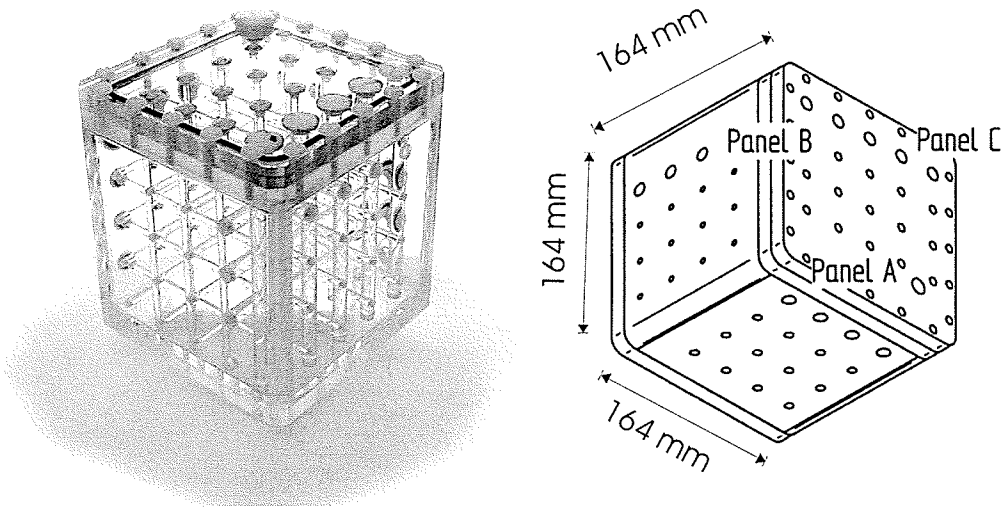

Figure 3-1 On the left is a photograph of the QA phantom. On the right is a 3-D schematic of the phantom, showing the placement of the 3 mm and 10 mm diameter acrylic rods.

3.3.2 Image acquisition

A complete CT image data set (66 slices, 512 by 512 pixel matrix) with a 3 mm slice thickness and zero gap in the transverse plane was acquired for the entire phantom with the CCMB Radiotherapy Department CT scanner[1]. Images were obtained using typical head scan parameters including an energy of 120 KeV, with a field of view of 50 cm diameter. The MRI acquisitions were performed on a 1.5T MRI scanner[2]. One set of T1-weighted spin echo transverse sequences (49 slices, 256 by 256 pixel matrix) was acquired for the entire phantom, with a 3 mm thickness and zero gap. A standard head coil was used during the acquisition. The field of view was 240×240 mm^2. For the MR data acquisition the repetition time was 500 ms and the echo time was 20 ms. All image data sets were directly transferred through the hospital network to the radiation treatment planning system[3] on which the image registration is performed.

[1] Somatom Plus 4 CT scanner, Siemens Medical Systems.
[2] 1.5 Tesla Genesis Signa, General Electric Medical Systems.
[3] Pinnacle[3], Philips Medical Systems, Inc.

3.3.3 Image Registration

The pixel intensity information of the rod positions in three dimensions forms the basis on which the image registration will be performed. The rods themselves form a set of fiducial landmarks. The MR and CT image sets are reviewed in the transverse, coronal, and sagittal planes. The image fusion tool provided in the radiation treatment planning software blends any two defined image sets together so that anatomical structures can be clearly visualized by enhancing the best features of both image sets. Using rigid body registration techniques, the MR image data set is mapped directly on to the CT data set, in the CT coordinate system. Upon completion of the image registration, the software stores all global transformations that the MR data set undergoes. This data is easily accessible. To assess reproducibility image registration is performed 10 times using the same pair of data sets. The errors in the image registration are an estimate of the accuracy of fiducial marker correlation through the entire image study. The discrepancies between adjacent rod positions, in both the MRI and CT data sets were measured. To determine the localization uncertainty, the fiducial registration error and the root-mean-square (RMS) of the FRE are calculated.

3.4 Analysis

3.4.1 Sagittal and Coronal images

The MR and CT image data acquired consisted of transverse slices of the phantom. To extend the analysis into a full three dimensional perspective, sagittal and coronal views of the phantom are needed. This was done by using a standard cubic interpolation routine. Cubic convolution is an interpolation method that closely approximates the theoretically optimum sinc interpolation function using cubic polynomials [Pa83]. In this manner the sagittal, and coronal slices were interpolated from the MR and CT transverse images. Thus the two original transverse data sets are interpolated to yield a total of 6 data sets: three MR (MR transverse, MR coronal, and MR sagittal), and three CT (CT transverse, CT coronal, and CT sagittal).

3.4.2 Rod Center Acquisition

The purpose of this analysis is to obtain the coordinates of the rod centers from each slice of the MR and CT data sets. The rods form a set of fiducial landmarks. Obtaining the centers of each rod in each plane will allow us to assess the spatial localization of the MR and CT image data sets. To obtain the coordinates of rod centers the following method is used for a given spatial direction of a data set (i.e., transverse, coronal, and sagittal):

1. **Read data for a single slice.**
2. **Filter background image from the regions of interest.**
3. **Isolate region of interest containing the rod.**
4. **Calculate center of mass of the rod, based on intensity of pixel values.**
5. **Convert pixel coordinates to radiation treatment planning coordinates.**
6. **Store rod centers*(x,y,z)* to a file.**

The region of interest is defined to be a square area (10 by 10 pixels) that contains only a small region around a rod. This sequence of steps is performed on both the MR and CT data sets.

3.4.2.1 Filtering the background image

The interleaving rods in all three directions pose a problem. In some of the images the rods parallel to the imaging plane show up quite close to the region of interest. This is illustrated in figure 3-2. To remove the interleaving rods from the image, a subtraction is performed on both the CT and MR data sets. The subtraction, as illustrated in figure 3-2, occurs by taking the image slice data, I_{slice}, and subtracting from it an image, $I_{subtract}$ that contains the image without the regions of interest of the rod center. The subtraction (I_{slice} - $I_{subtract}$) give the result, I_{final} . I_{final}, contains only the regions of interest as shown in figure 3-2c. Outside the regions of interest the pixel intensity is zero. In carrying out this filtering step, any 'parallel rod' pixel contribution to the center of mass calculation, occurring in the following step, is removed.

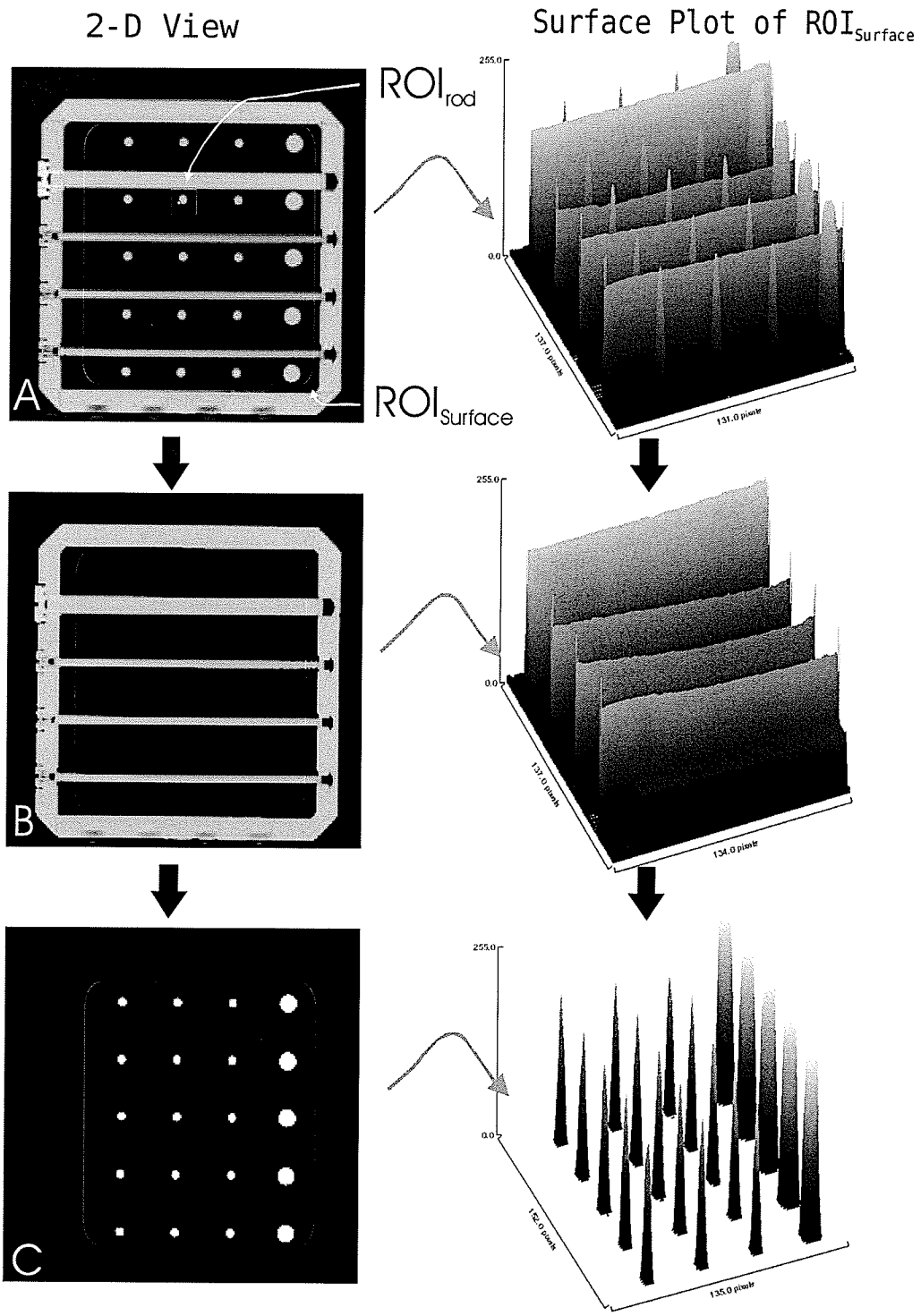

Figure 3-2 In (A), a CT slice, I_{slice} , taken at the middle of the phantom is shown. The bright circular dots are the rods. A single region of interest is drawn around the rod, ROI_{rod}. In (B) the subtraction image, $I_{subtract}$, is shown without the ROI_{rod}'s. Finally in (C), the final image, I_{final}, contains only the ROI_{rod}'s. Alongside the images (A), (B), and (C), the surface plots of the regions just inside of plates of each image are illustrated.

3.4.2.2 Center of Mass

To determine the center of the rod within the region of interest, the center of mass or pixel intensity is calculated. In this case, the pixel intensity is analogous to mass. Thus, the center of the rod is defined by considering the extension of the classical definition of center of mass and calculating over a region of N pixels. The x and y coordinate center is then calculated by:

$$x_c = \frac{\sum_{i=0}^{N} x_i p_i}{P} \tag{3.1}$$

$$y_c = \frac{\sum_{i=0}^{N} y_i p_i}{P} \tag{3.2}$$

where p is the pixel intensity at coordinate (x_i, y_i), and P is the total pixel intensity of the entire region of interest. For the transverse image, there will be 20 rod center positions, and for the coronal and sagittal image there will be 16 rod center positions. (See figure 3-3.) Once the rod center coordinates are calculated, the pixel coordinates are recalculated to the radiation treatment planning coordinates.

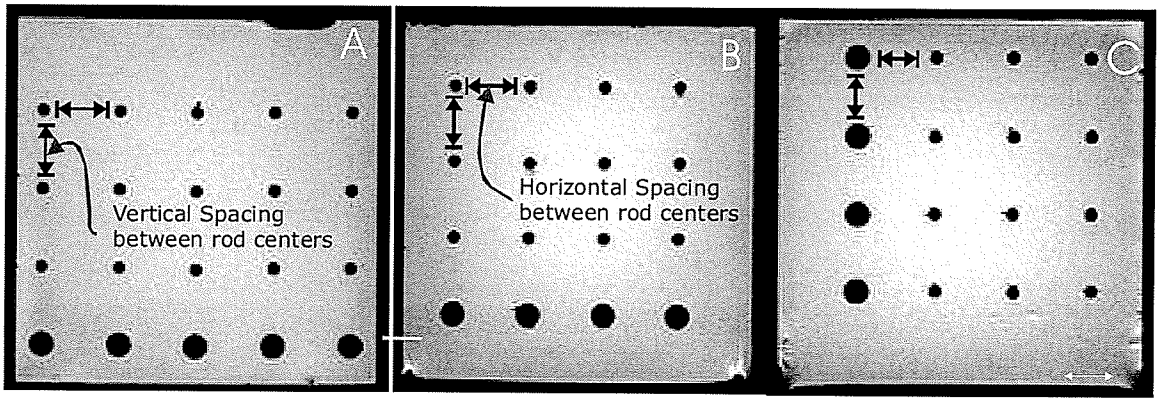

Figure 3-3 (A), (B), and (C) are Transverse, Sagittal, and Coronal mid-phantom images acquired with the MR scanner.

3.4.3 Rod Spacing

The rod positions in all three views (transverse, sagittal, and coronal) are analysed to determine the separation between adjacent rods. Simple vector subtraction is used to calculate the displacement between the rod centers. In doing this we assume no out-of-plane variations.

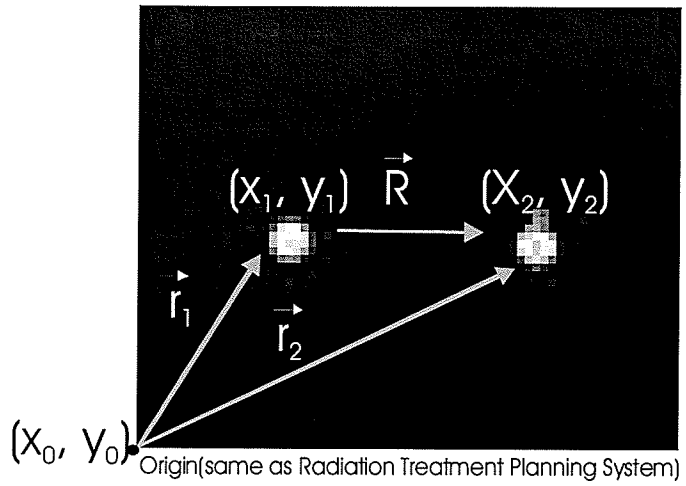

Figure 3-4 The displacement between the rod centers, $|\vec{R}|$ is found by simple vector subtraction of $\vec{r}_1$, and $\vec{r}_2$. Thus $|\vec{R}| = |\vec{r}_1 - \vec{r}_2|$. Where $\vec{r}_1 = [x_1 - x_0, y_1 - y_0]$, and $\vec{r}_2 = [x_2 - x_0, y_2 - y_0]$. Subtracting the x and y coordinates alone is not satisfactory since the rods may not be exactly aligned with the imaging coordinate axes.

3.4.4 Fiducial Landmark and Registration Error (FLE and FRE)

The image registrations performed previously allow a simple calculation of the fiducial registration error (*FRE*), as defined in section 2.5.1. In addition, the RMS(FRE) is calculated. To calculate the FRE, the coordinates of the rod centers within a particular slice are directly compared to the registered rod center of the same slice from the MR image. Then the FRE value for each rod location is averaged over all slices in the phantom. This calculation was performed on 40 evenly spaced slices in each direction. To further illustrate the FRE calculation, consider figure 3-5. The transformation matrices

retrieved from the radiation treatment planning system are applied to the MR rod center coordinates to simulate the image registration. Using equation 2.19, the rod center coordinates are then compared to the CT rod center coordinates to estimate the FLE. From this, the FRE can be calculated using equation 2.24.

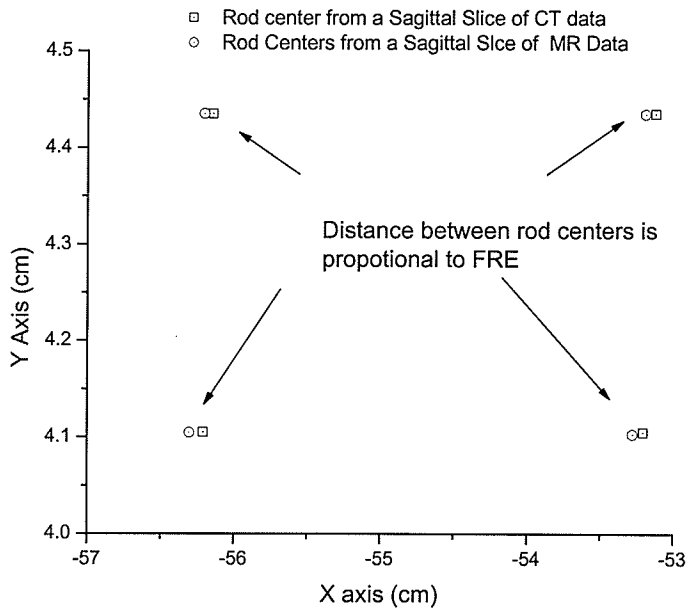

Figure 3-5 The FRE is defined as the distance between the CT rod center location, and the transformed MR rod center location. In this figure, the rod centers are taken from the transverse slices of the MR and CT data sets. In this example, a slight systematic misregistration of ~1 mm is apparent. The MR rod center locations are shifted in the negative x-direction.

3.5 Results and Discussion

The results of the analysis show that the spacing between rod centers across the phantom is consistent along each spatial direction for both the MR and CT data sets. Table 3-1 shows results of the average spacing over the entire phantom. In the transverse direction, where spatial resolution is higher, the average spacing between rods was 3.00±0.02 cm in the CT data set, and 2.98±0.02 cm in the MR data set. The minimum and maximum rod separations for the CT transverse slices are 2.93 cm and 3.06 cm, while for the MR transverse slices are 2.91 cm, and 3.02 cm.

These results indicate sub-voxel accuracy of the geometric uniformity. This is of particular interest to radiation treatment planning, because only transverse image are currently used for treatment planning purposes. These results indicate the imaging equipment is producing very geometrically uniform images. Considering target margins in radiation treatment planning are on the order of 5-20 mm, this indicates that there will be very little error introduced into the target volume delineation. In the transverse, sagittal and coronal views, the values also agree within one standard deviation between CT and MRI. The plots of the average spacing per slice in each spatial direction for both MR and CT data sets is shown in figure 3-6 and figure 3-7.

Table 3-1: Average Spacing Between Adjacent Rods

		Average Spacing(cm)	Min(cm)	Max(cm)
CT	Transverse	3.00±0.02	2.93	3.06
	Sagittal	3.00±0.03	2.93	3.07
	Coronal	3.00±0.03	2.91	3.07
MR	Transverse	2.98±0.02	2.98	3.02
	Sagittal	3.01±0.02	2.90	3.09
	Coronal	3.09±0.03	3.00	3.19

Table 3-1 The average spacing between adjacent rod centers over all slices in the phantom for each particular plane of view.

In addition to these figures, a histogram plot of the data is shown in figure 3-8. Although the displacement measurement between the rod centers provides a good measure of the spatial uniformity of the phantom during image acquisition, a measurement of the fiducial landmark error also provides useful information about the image registration process. In this analysis, the results indicate an average FRE of 1.0±0.6 mm in the transverse view, 0.4±0.3 mm in the sagittal view, and 1.0±0.7 mm in the coronal view. These findings are similar in magnitude to the results in the spacing between adjacent rod centers, where the spatial uniformity was <1 mm of the design specification. To evaluate the fiducial registration error, the MR image data was registered to the CT data 10 times to account for intraoperator variability. The results are illustrated in figure 3-9. The FRE results also indicate sub-voxel accuracy, unlike previous studies [Or99], where geometric uniformity error were as large as 1.99 mm. In

[Or99], they attributed the large error to registration accuracy, however in those studies the FRE was not compared to the geometric uniformity error to put into perspective the image registration.

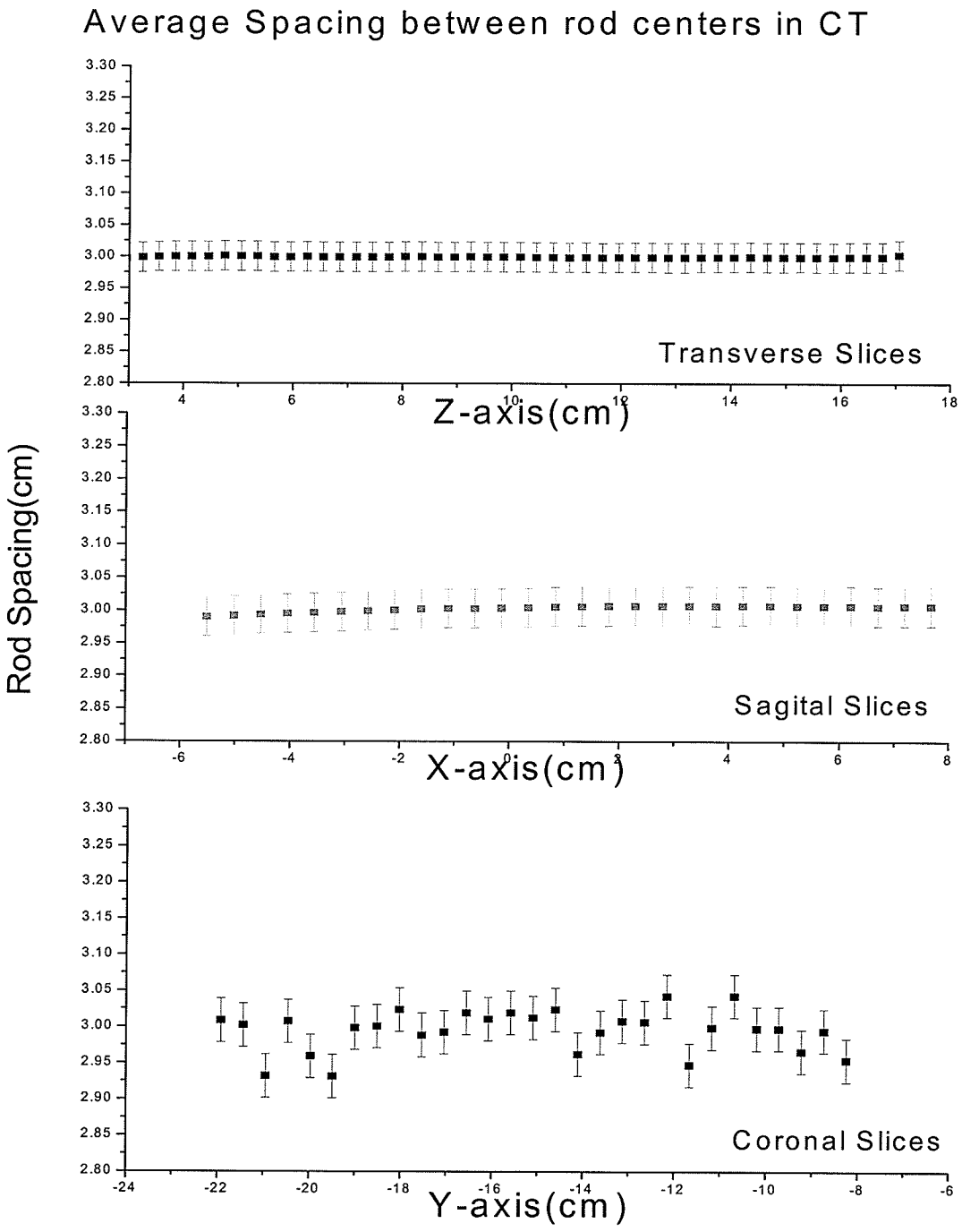

Figure 3-6 Spacing between rod centers in all three spatial directions for the CT image data set.

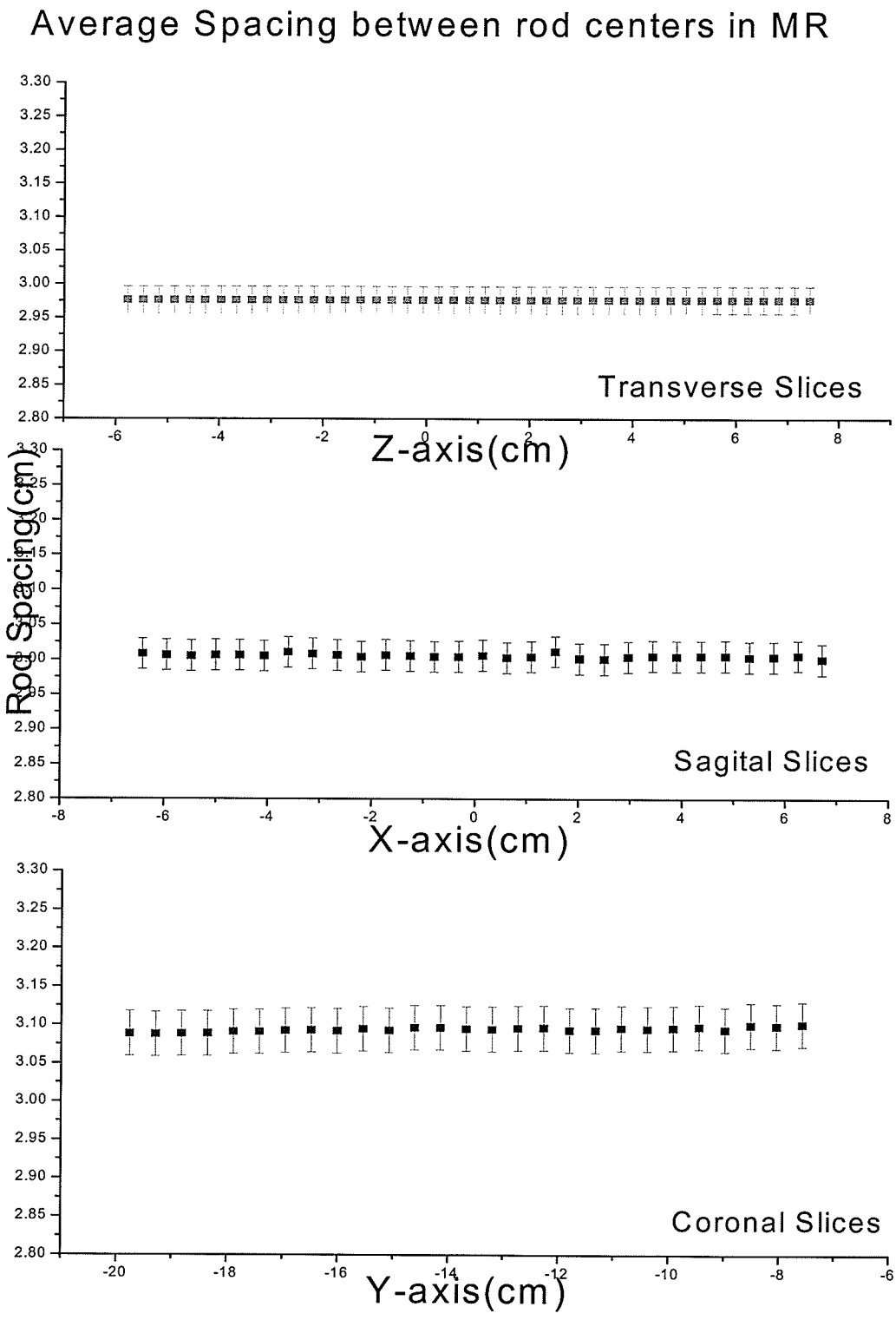

Figure 3-7 Spacing between rod centers in all three spatial directions for the MR image data set.

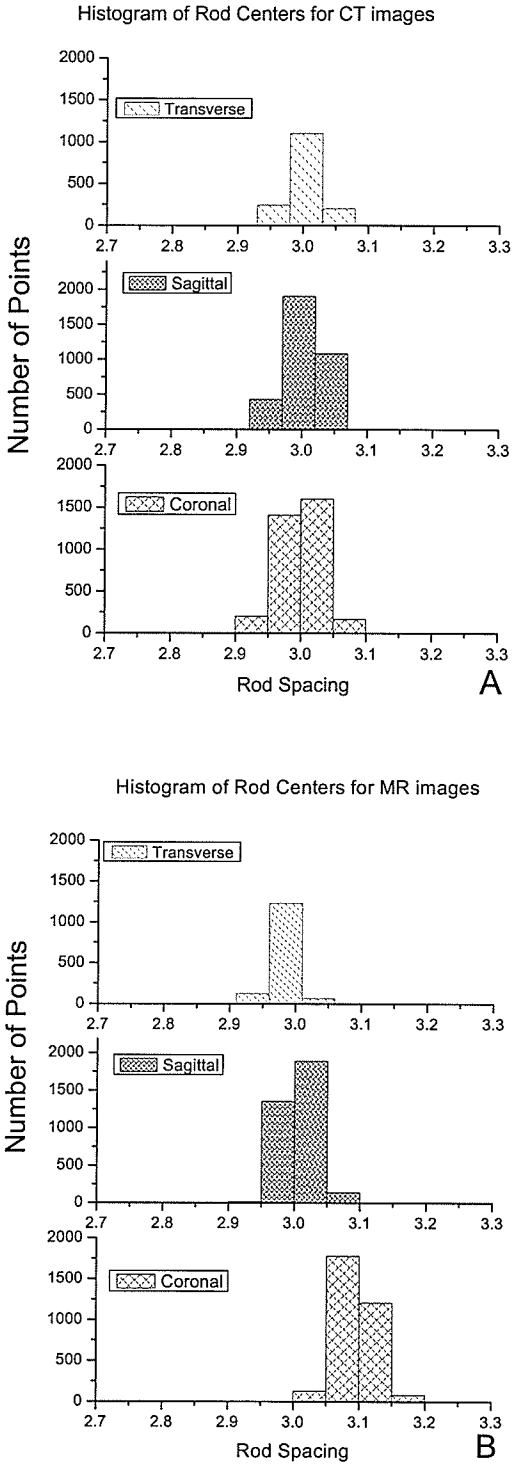

Figure 3-8 In (A) a histogram of the CT rod centers are presented in all three planes of view. Similarly in (B), a histogram of the MR rod centers are presented for all three planes of view.

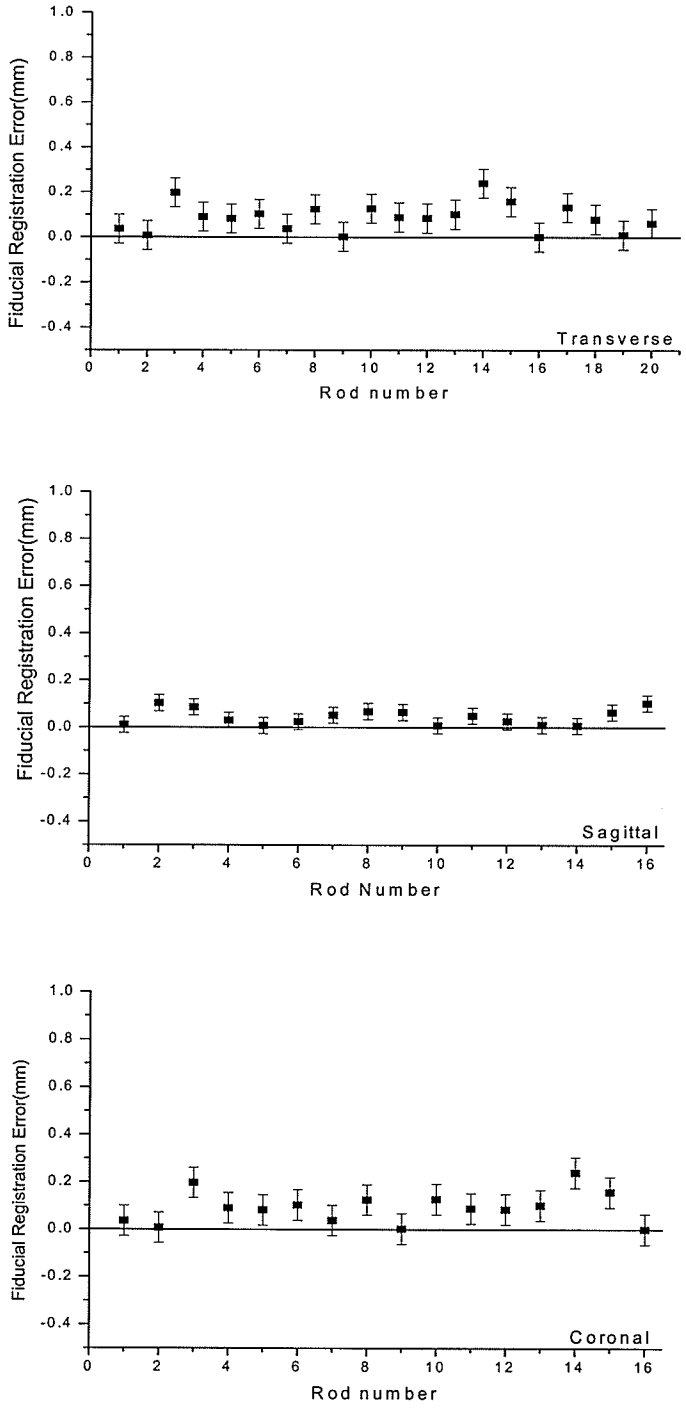

Figure 3-9 The fiducial registration error (FRE) is presented for each rod for slices, in each plane of view. In the transverse view, there are 20 rods, while in the sagital, and coronal view there are 16 rods. Rods are labeled left to right, top to bottom according to figure 3-3.

3. 6 Conclusion

The quality assurance measurements for the image registration process at CancerCare Manitoba were performed with a hollow phantom that was constructed with solid acrylic rods orientated in all three orthogonal directions (i.e. transverse, sagittal, and coronal). The spacing between the rods in the CT images was measured to be 3.00±0.02 cm in the transverse direction, 3.00±0.03 cm in the sagittal direction, and 3.00±0.03 cm in the coronal direction. Similar results were found in the MR images, where the rod spacing was measured to be 2.98±0.02 cm in the transverse direction, 3.01±0.02 cm in the sagittal direction, and 3.09±0.03 cm in the coronal direction. These values compare well to the design values of the phantom which was 3.0 cm. The quality of the geometric uniformity of MR images compares well with that of the CT data, although the CT uniformity is still superior. The geometric uniformity of both modalities is subvoxel. This result indicates that very little error will be introduced into the target delineation by the image registration process. To assess the fiducial registration error and its RMS uncertainty, a registration between the MR and CT image data sets was performed ten times. The fiducial registration error was found to be 1.0±0.6 mm in the transverse view, 0.4±0.3 mm in the sagittal view, and 1.0±0.7 mm in the coronal view. These values indicate that the image registration is being performed to <1mm accuracy. The results of the geometric uniformity and FRE calculation support each other in demonstrating the sub-voxel accuracy of the image registration process.

It is recommended that periodic and comprehensive accuracy assessments of the image registration process should be performed in the treatment planning quality assurance program. For a given set of CT and MR images, the spacing between the rod centers should be uniform. For most of intracranial lesions where the image registration procedure is used, the accuracy of the registration can be achieved within the size of a voxel. The characteristics of the geometric uniformity and FRE obtained in this study strictly apply to the specific scanners studied.

CHAPTER 4

Fusion in Retrospect: A Study to quantify the effect of digital image fusion in radiation treatment planning of brain tumours

4.1 Abstract

In this study the target localization differences caused by introducing digital image fusion into routine treatment planning of brain cancer patients are quantified. Data for twenty brain cancer cases where digital image fusion was employed in the treatment planning process were analyzed. A single Radiation Oncologist re-contoured the gross target volume for 20 patient data sets, using both the new (digital image fusion) and the old (non-digital image fusion) methods. After the contouring process was completed, a number of different quantitative parameters were extracted from the digital fusion and non-digital fusion contoured data sets. These parameters included: the magnitude of shift between the geometric centres, the structure volume, spatial translation and angle rotation extracted from the digital image fusion transformation matrix, the maximum geometric miss as observed when looking through the beam's eye view for all fields of the final treatment plan, as well as the time required to perform the contouring via each method. Shifts between the digital fusion and non-digital fusion target's geometrical centers ranged from 2 mm to 15 mm. Volumetric differences in the targets ranged from 1 cm^3 to 112 cm^3. Had treatment proceeded using the non-digital image fusion technique, it is estimated that maximum geometric misses ranging from 2mm to 36mm would have occurred. On average, it took 3.69 minutes to perform the target delineation using the digital fusion versus 4.33 minutes using the non-digital fusion method. There is a significant improvement in target delineation when using digital image fusion as compared to previous, non-digital image fusion methods. Quantitatively, this improvement may be of similar or larger magnitude compared to the typical target

margins applied to brain tumours. This study underscores the critical need for digital image fusion in the radiation treatment planning process for brain tumour patients.

4.2 Introduction

Computed tomography data are currently used for routine, three-dimensional (3D) planning of radiotherapy treatments. This x-ray based imaging modality offers two major advantages for this purpose: 1) it may be converted easily into density information (physical or electron), necessary for accurate dose calculations, and 2) it does not suffer from spatial distortions (e.g. geometrically uniform). While CT imaging provides excellent anatomical information in general, the images do not exhibit good soft tissue contrast. For this reason, magnetic resonance images (MRI's) or contrast-infused CT images are often used in addition to or in combination with the CT simulator image data, to provide improved soft tissue contrast. In many instances (especially the central nervous system), the tumor extent is much more readily visible in the MRI or infused CT images. However, incorporating this additional imaging data into the treatment planning process may be challenging. For example, MRI data are not related to physical densities, may suffer from spatial distortions, and slice thicknesses may be in error [Ho98].

Prior to the advent of digital image fusion methods, the Radiation Oncologist (RO) was forced to estimate the tumor outline from MRI (or infused CT) image data printed on film, and manually draw these onto the CT simulator data. In this work, this approach is referred to as the 'non-digital image fusion method'. This process required the physician to mentally account for differences in the patient's position which have occurred between the acquisition of the diagnostic imaging data and the CT simulation data.

Over the last several years, digital image fusion techniques have been vigorously researched as a possible solution to some of the problems mentioned above. Image fusion is a process by which one image data set is mathematically mapped onto another image data set in such a manner as to ensure anatomical coincidence. Typically, rigid

body transformations (e.g. translations, rotations) are used to match a reference image data set. For example, in radiotherapy treatment planning, a secondary study set (i.e. MRI, infused-CT, PET, etc.) may be registered to a primary study set which is generally the CT simulation image data set. Although many types of image fusion algorithm exist (e.g. automated, semi-automated, manual), in general the algorithms will attempt to minimize the difference measures that assess the quality of the fit, through an iterative process. Mapping the supplementary diagnostic imaging data onto the CT simulator imaging data maintains the geometric qualities and density information of the CT modality while simultaneously providing the excellent soft tissue contrast of the MRI, or better tumour visualization of the infused CT. The combined data set allows for improved accuracy in tumor and critical structure delineation.

Several studies indicate that tumor localization using CT data alone (compared with fused CT-MRI data) results in widely varying tumor volumes and in an unacceptable rate of misses [Ka97, Kh00, La97]. Kagawa *et al* comments that in the 3D conformal treatment of the prostate, MRI image data was invaluable. In another study Lattanzi *et al* used CT/MRI fusion to improve tumour localization in primary central nervous system lesions. In that study they demonstrated that when comparing CT/MRI fusion GTV's (gross tumour volumes) to CT-alone GTV's, in one case the large discrepancy between the two methods resulted in a 72% increase in the radiographic tumour volume. Therefore, the use of image fusion techniques in the treatment planning process improves the accuracy of tumor delineation. The primary disease site for application of image fusion techniques is the central nervous system (including brain) [Kh00, La97, Ko93], but advantages have also been demonstrated for ocular tumors [Ho97], rectum [Ho98], and prostate [Ka97, La96].

This work examines variations in target delineation due to two different, clinically used image registration techniques. An underlying assumption throughout this analysis is that the digital image fusion is inherently more accurate than the non-digital image fusion method. Note that this does not imply that the digital image fusion techniques is without error. Both approaches possess the same underlying uncertainties due to the physical

differences between the primary and secondary image data sets (i.e. slice thickness and voxel size differences, potential non-uniformity of MRI data, etc.).

This study provides a quantitative evaluation of the improvements in accuracy provided by the digital image fusion technique over the previous, non-digital image fusion technique for treatment planning of brain tumours.

4.3 Methods and Materials

4.3.1 Patient population

A retrospective analysis was performed on 20 patient data sets that had already been planned using digital image fusion for the treatment of brain tumors. Of these 20 data sets, 13 used MRI images and 7 used infused CT images as the secondary study set. Based on the histology, there were 11 Glioblastomas, 2 Anaplastic Astrocytomas, 2 Gliosarcomas, 2 Mixed Gliomas, 1 Glioma, 1 Atypical Meningioma, and 1 Pituitary Macroadenoma, as summarized in table 1.

4.3.2 Image registration method

All 20 treatment plans used the CT simulation images as the primary image set. An MRI or infused-CT image was registered as the secondary image sets. This is done because the treatment planning software* requires CT data to perform the treatment plan dose calculations. The CT simulation image data were acquired† and transferred via an internal LAN to the treatment planning system. Immobilization consisted of a custom thermoplastic cast, and the image data was acquired in serial mode with slice thickness and index of 3 mm. The diagnostic image data (either MRI or infused CT) was transferred from a local picture archiving and communications system (PACS) to the treatment planning system, using a digital information communication (DICOM)

* Focus 3D, Computerized Medical Systems Inc., St. Louis, MO
† Somatom Plus 4 CT scanner, Siemens Medical Systems, CancerCare Manitoba, Winnipeg, MB

software product. MR image data was acquired with a 1.5T whole body scanner[‡] , while gadolinium infused CT data was acquired with a helical CT scanner[§]. Once both primary and secondary study sets were loaded onto the treatment planning system, the image data sets was registered (i.e.'fused') using the treatment planning software. The registration was performed manually by the RO, using anatomical knowledge and rigid body transformations. When the registration was completed, a file containing the transformation matrix is created in a local subdirectory.

Table 4-1: Patient Population

Histology	Fusion Type	Number of Study Sets
GBM	MRI/CT	9
	Infused-CT/CT	2
Anaplastic Astrocytoma	Infused-CT/CT	2
Gliosarcoma	MRI/CT	1
	Infused-CT/CT	1
Mixed Glioma	MRI/CT	2
Glioma	MRI/CT	1
Atypical Meningioma	Infused-CT/CT	1
Pituitary macroadenoma	Infused-CT/CT	1
Total number of study sets		20

Table 4-1 Histological classification and the type of digital image fusion used for each disease type. There a total of 20 study sets. Each study set contained the contours for GTV structure via both fusion and non-fusion techniques.

4.3.3 Target Delineation

Since this work was performed on planned data sets, the previously identified GTV was not displayed. A single RO performed the re-contouring of the gross tumour volumes. This approach was taken because Welton et al. reports large inter-operator variability exists in GTV delineation [We01]. This large variability in GTV delineation would be an additional and obscuring uncertainty in this study, so inter-observer

[‡] 1.5 Tesla Genesis Signa, General Electric Medical Systems, Health Sciences Centre, Winnipeg , MB
[§] Light-Speed Helical CT Scanner, GE Medical Systems, Health Sciences Center, Winnipeg, MB

variability effects was eliminated by using a single observer. However, this does not eliminate potential intra-observer variability, which has not been studied.

For each of the 20 patient data sets, the RO contoured the GTV using the digital image fusion technique. In this technique, the RO performed the target delineation directly on the MRI or infused-CT data set, after it had been registered to the CT simulation data set. After a significant period of time elapsed (~3 weeks), the same RO contoured all of the tumour target volumes using the non-digital image fusion method (ie. utilizing radiographic films). This method required the RO to view a radiographic image of the MRI or infused-CT image on a lightbox, and then contour the GTV on the primary CT data set in the treatment planning software. The time required for the RO to contour the GTV via each method was recorded.

4.4 Analysis

After the contouring process was completed, a number of different quantitative parameters were extracted. These parameters included: the shifts between the geometric centres of the target structures, the volumes of the target structures, spatial translations and angle rotations extracted from the digital image fusion registration matrix, and the maximum geometric misses as observed when looking through the beam's eye view (BEV) for all fields of the final treatment plan.

The volume of contoured structures was directly calculated using a software tool within the treatment planning system. The shift in the position of the geometric centres of the two GTV's was also extracted through the use of a software tool, that calculates the three-dimensional coordinates of the geometric center of any structure. Therefore, the shift between the geometric centers is found by calculating the distance between these two points.

However, the question remains, what is the clinical impact on the delivered treatment *if* the non-digital image fusion GTV had been used instead of the digital image fusion GTV? To assess this as directly as possible, the concept of geometric miss was

used. Here, a 'geometric miss' is defined as occurring when a field edge is too close to the planning target volume (PTV), meaning that the field edge placement will not provide adequate dosimetric coverage along that edge of the PTV. This terminology is commonly used to describe gross errors observed when reviewing portal images, since patient anatomy may move in or out of the field on a day-to-day basis, thus potentially resulting in a 'geometric miss' of the PTV. The term is used here since a change in GTV position (and hence PTV) due to the difference between the digital image fusion and non-digital image fusion contouring processes is analogous to changing the patient position. The maximum geometric misses were estimated by measuring the maximum radial distance (from central axis) between the edges of the non-digital image fusion GTV and the digital image fusion GTV, in the beams eye view (BEV), for all fields in the final treatment plan. This approach assumes that differences in the isocentre position chosen for planning between the two techniques would be small, and a uniform margin added to the GTV to yield the PTV would not effect the BEV assessment of maximum geometric miss. These should be reasonable assumptions, since the geometric centre shifts and therefore the difference to the chosen isocenter locations are small when compared to the 100 cm source-to-axis distance, and the GTV's are reasonably elliptical. For example consider figure 4-1, where an imaging software package[‖] is used to draw a radial vector extending from the isocenter to the outermost point of the digital image fusion GTV to estimate the maximum geometrical miss. Two measurements were taken with a digital ruler[χ] along the radii where the digital image fusion target edge was furthest from the original planned isocenter. One was taken along the radial direction from isocenter to the outer edge of the digital fusion image GTV. The second measurement was taken along the same direction as the first radial vector, but from to the non-digital image fusion target edge. A subtraction between the first and second measurements provides an estimate of the maximum geometric miss as observed in that particular field BEV. The maximum amount of overexposure of normal tissue may be estimated in a similar manner, except that the radius is located where the non-digital image fusion target edge was

[‖] Image J, RSB Research Services Branch, http://rsb.info.nih.gov/ij/ .

[χ] Measurements were made with the digital ruler which measures the number of pixels. A pixel to centimeter conversion is done based on known values of spatial tick marks.

furthest from the original planned isocentre. Based on these measurements, the average maximum geometric miss was calculated by using the dosimetric weighting of each beam:

$$\text{Average Maximum Target Miss} = \frac{\sum_{\text{all beams}} (\text{maximum target miss}) \times (\text{beam weight})}{\sum_{\text{all beams}} (\text{beam weight})} \quad (4.1)$$

This ensures the average maximum geometric miss is more dosimetrically relevant.

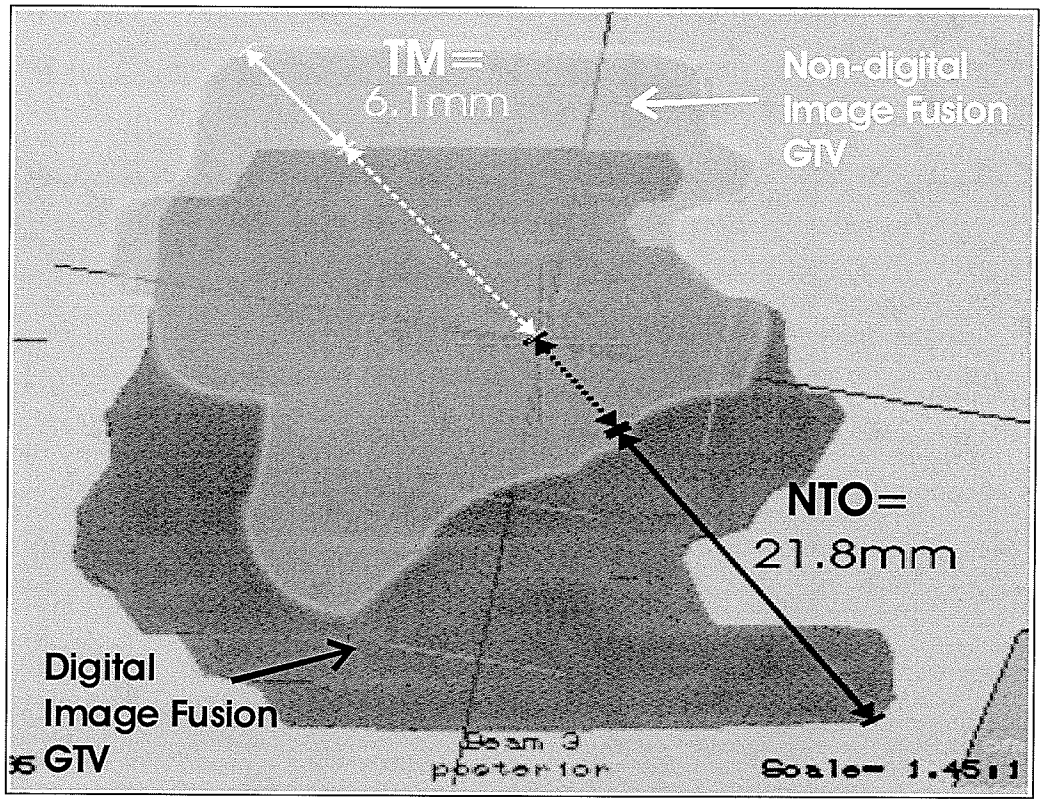

Figure 4-1 Maximum geometric miss as seen from the BEV. The geometric miss between the digital image fusion (dark grey) and non-digital image fusion (light grey) targets can clearly be seen. In this diagram both the maximum geometric miss (black) and normal tissue over irradiation (white) have been highlighted to show the method of measurement .(TM=Target Miss, NTO= Normal Tissue Over Irradiation)

The transformation matrix that was used to align the primary (CT) and secondary (MRI/infused CT) study sets was analyzed to extract the rotation and translation information used for the digital image fusion. The correlation between the magnitude of rotations and translations needed to perform the digital image fusion and the difference

measures (i.e. geometric position differences, volumetric differences) was examined. To simplify the analysis, the rotation angles were added in quadrature to yield a single average rotation angle parameter (δ), while the translation vector was converted to a distance value (λ). The correlations here are of interest since they would reveal if the non-digital image fusion approach could be improved by ensuring the patient position in the diagnostic image acquisition were the same as that during CT simulation.

Finally, the time required for the contouring process was measured, to assess if there were any efficiency differences. Note that the time required for the image registration step of the digital image fusion process was not included in this measurement.

4.5 Results and Discussion

Volumetric comparisons between the GTVs demonstrate differences varying between 1 and 112 cm^3 , as illustrated in figure 4-2. This large range is mainly due to three outliers where there was a significant difference between the results of the two methods of target delineation (cases 3,14, and 17). For the remainder of the cases, there appears to be only small volumetric differences (<50 cm^3) between the two GTV's. The relative volumes of the GTVs, also exhibit a wide range of differences (4.2-49.2%). When the required GTV to PTV expansion margin is added (typically ranging from 1.5 to 2.5 cm), the relative volumetric differences are even smaller as illustrated in Figure 4-2. This is expected, since adding a margin will produce larger volumes that will minimize the effect of differences of the original GTV volumes. The result for the volumetric GTV comparison indicates that, in most cases, the physician has a reasonable ability to conserve the target volume when transferring from the radiographic film via the non-digital image fusion method.

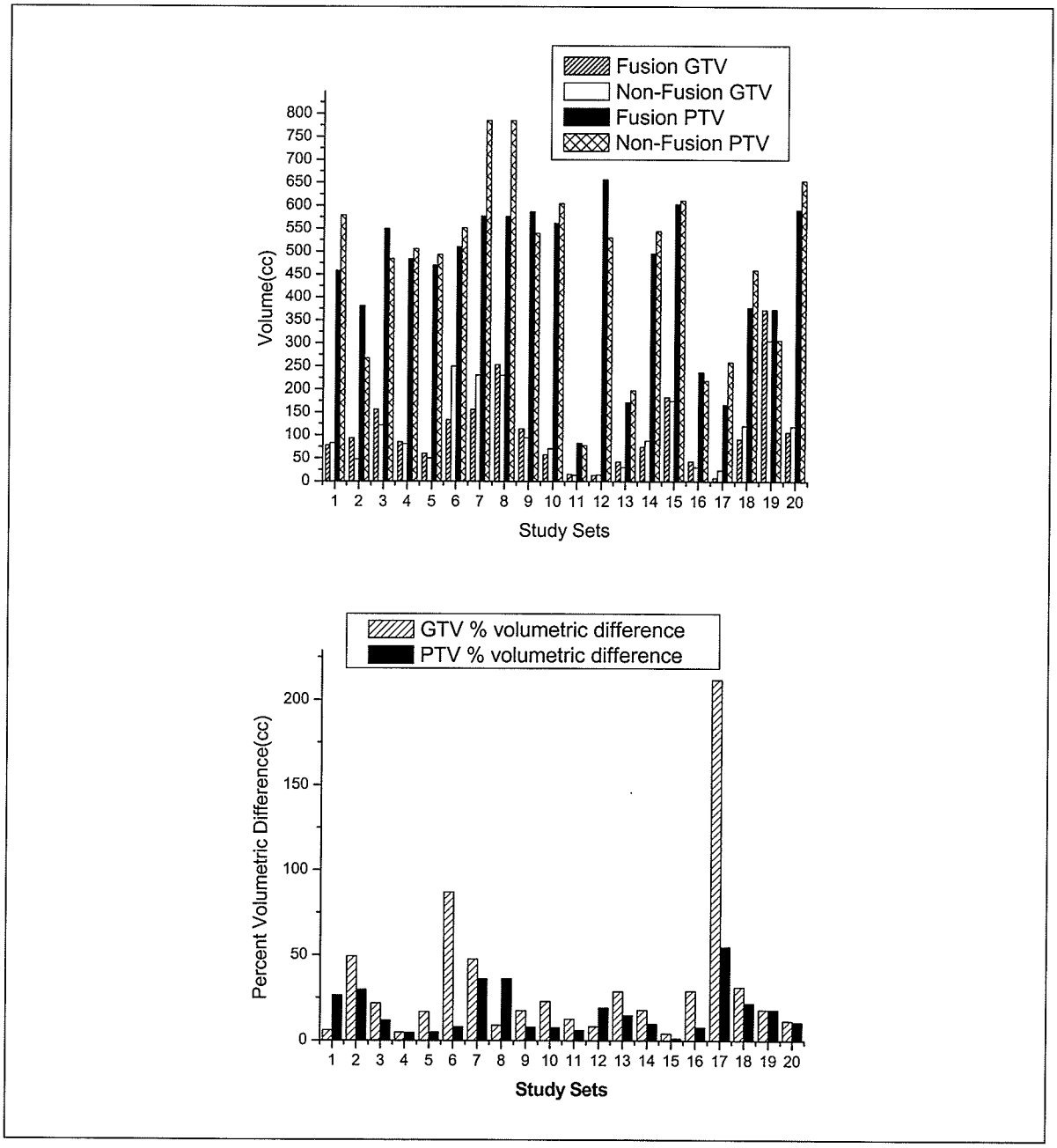

Figure 4-2 A: The volumes of the GTV and PTV structures via each digital image fusion and non-digital image fusion methods. Study sets 1-13 represent MRI/CT fusion study sets. While Study sets 14-20 represent Infused-CT/Ct fusion study sets. **B:** Percent Volumetric difference GTV's and PTV's of digital image fusion and non-digital image fusion volumes.

Examining the differences between the geometric centers of the two GTV's revealed spatial shifts ranging from 2 mm to 17 mm, with an average of 9.7 mm (refer to Figure 4-3). These shifts are significant when we consider that treatment field geometry

is generally accurate to less than 2mm. It is interesting to note that while the volumetric comparison indicated a clear and significant improvement in accuracy in only a few cases (cases 3, 14, and17), the geometric center shift indicates significant improvement in almost all cases. The observed shifts are significant, even when considering the typical GTV-PTV margin expansion in brain tumors is 15-25 mm. These geometric shifts have the potential to cause a geometric miss (as discussed below) of the PTV and possibly even GTV, and therefore may correspond to an associated decrease in patient outcome.

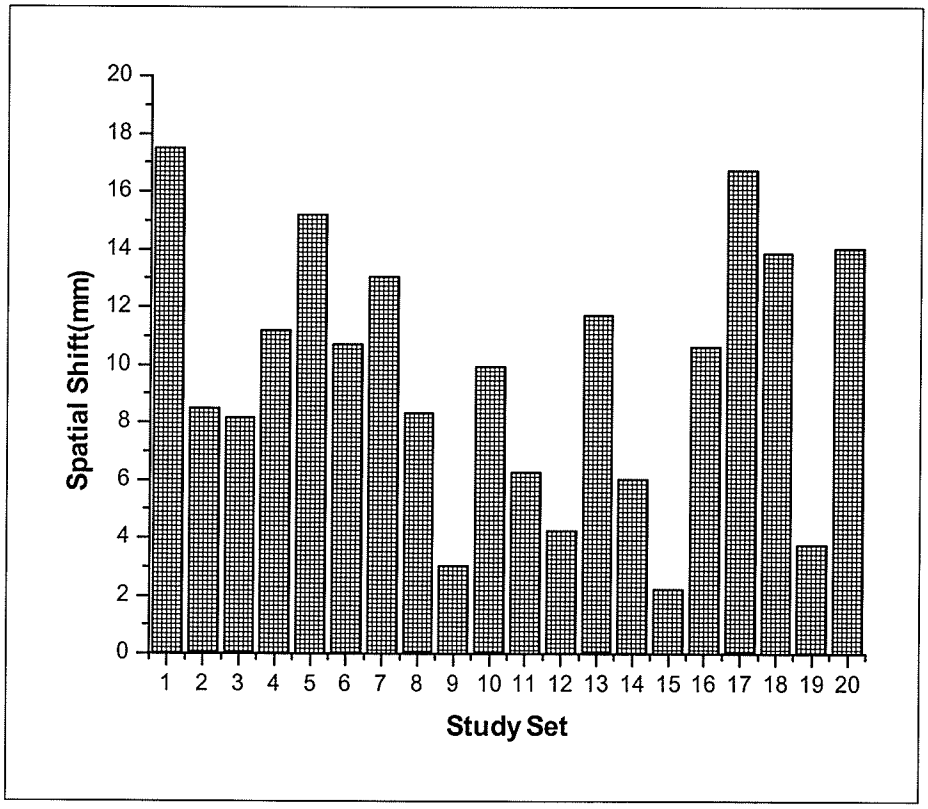

Figure 4-3 Spatial Shifts between digital image fusion and non-digital image fusion geometric centers.

The maximum geometric miss estimates are presented in Table 4-2. For an individual treatment field, the potential maximum geometric miss ranged from 2 mm to 36 mm. For each treatment, the average (beam weighted) maximum geometric miss ranged from 2.3 mm to 23.1 mm, as averaged over all fields in the final treatment plan. The maximum geometric miss parameter appears to be more sensitive than either the volumetric difference or geometric center shift. The maximum geometric miss parameter

is the most clinically relevant parameter investigated here, since it depends upon the specific geometry of the GTV's (and therefore associated PTV's) and the direction of approach of the treatment fields. In addition to the average maximum target miss, the average maximum normal tissue over-irradiation was measured using the same technique. Values ranged from 4.4mm to 28.8mm. Clinically these values are significant when considering unnecessary over irradiation.

Table 4- 2: BEV measurements

Study Set	Number of treatment fields	Average TM (mm)	Largest TM (mm)	Smallest TM (mm)	Average NTO (mm)	Largest NTO (mm)	Smallest NTO (mm)
1	3	12.64	16.08	6.73	18.18	26.33	6.12
2	3	5.04	7.65	3.59	19.32	20.15	16.96
3	2	7.23	7.38	7.09	15.61	17.80	13.32
3	2	2.26	3.62	3.31	4.43	9.18	8.52
5	3	13.87	13.57	13.35	28.82	32.76	22.53
6	6	3.44	5.21	1.67	25.21	30.15	18.32
7	5	5.58	16.03	0.00	23.30	33.11	21.08
8	3	15.55	35.66	6.09	9.96	21.98	8.57
9	3	9.41	13.97	3.53	5.68	7.32	3.39
10	3	7.29	11.33	1.91	15.79	20.20	11.55
11	3	10.22	13.53	3.53	6.95	7.83	6.30
12	5	7.56	8.25	6.36	7.93	8.55	3.11
13	3	23.14	28.75	20.35	13.98	18.25	6.12
13	3	7.05	7.37	6.73	22.63	23.96	20.29
15	6	7.19	15.12	3.20	4.79	6.95	2.86
16	3	16.24	23.01	9.90	13.31	19.23	7.15
17	3	8.22	19.31	0.73	17.34	21.87	12.32
18	3	7.84	9.72	6.26	21.28	28.91	15.23
19	3	16.78	22.97	12.86	20.76	37.22	8.28
20	3	8.95	12.79	6.28	13.63	16.59	10.98

TM=Target Miss, NTO= Normal Tissue Over Irradiation

Table 4-2 Summary of the results obtained through the BEV analysis. The average maximum TM (target miss) represents the average maximum radial displacement between adjoining non-digital image fusion to digital image fusion edges over all fields in that particular treatment field geometry. Conversely, the average maximum NTO(normal tissue over irradiation) represents the average maximum radial displacement between adjoining non-digital image fusion to digital image fusion edges over all fields. The smallest and largest values over all fields for both type of measurement are listed for comparison.

Both the average rotation angle parameter (δ) and the translation distance parameter (λ) were plotted against the geometric shift between the GTV's (see Figure 4-

4). Note that some of the rotation angle parameters were large, due to the patient being CT simulated in a rolled position while the diagnostic data was acquired in supine position. A least-squares fit of each data set in Figure 4-4 revealed a very poor correlation constant (r = 0.5 and 0.04 for δ and λ respectively). If these data sets were found to be highly correlated it would provide evidence that acquiring the patients diagnostic image data in a position close to the treatment position would result in improved accuracy of the non-digital image fusion method. Due to the poor correlation observed this is not the case.

Measuring the time required for the RO to complete the GTV contouring via each method revealed that, on average, it took 3.69 minutes (range of 1.2 to 6.5 minutes) via the digital image fusion method and 4.33 minutes (range of 1.5 to 6.5 minutes) via the non-digital image fusion method. Therefore, contouring the GTV using the digital image fusion technique does not save a significant amount of time compared to the non-digital image fusion method.

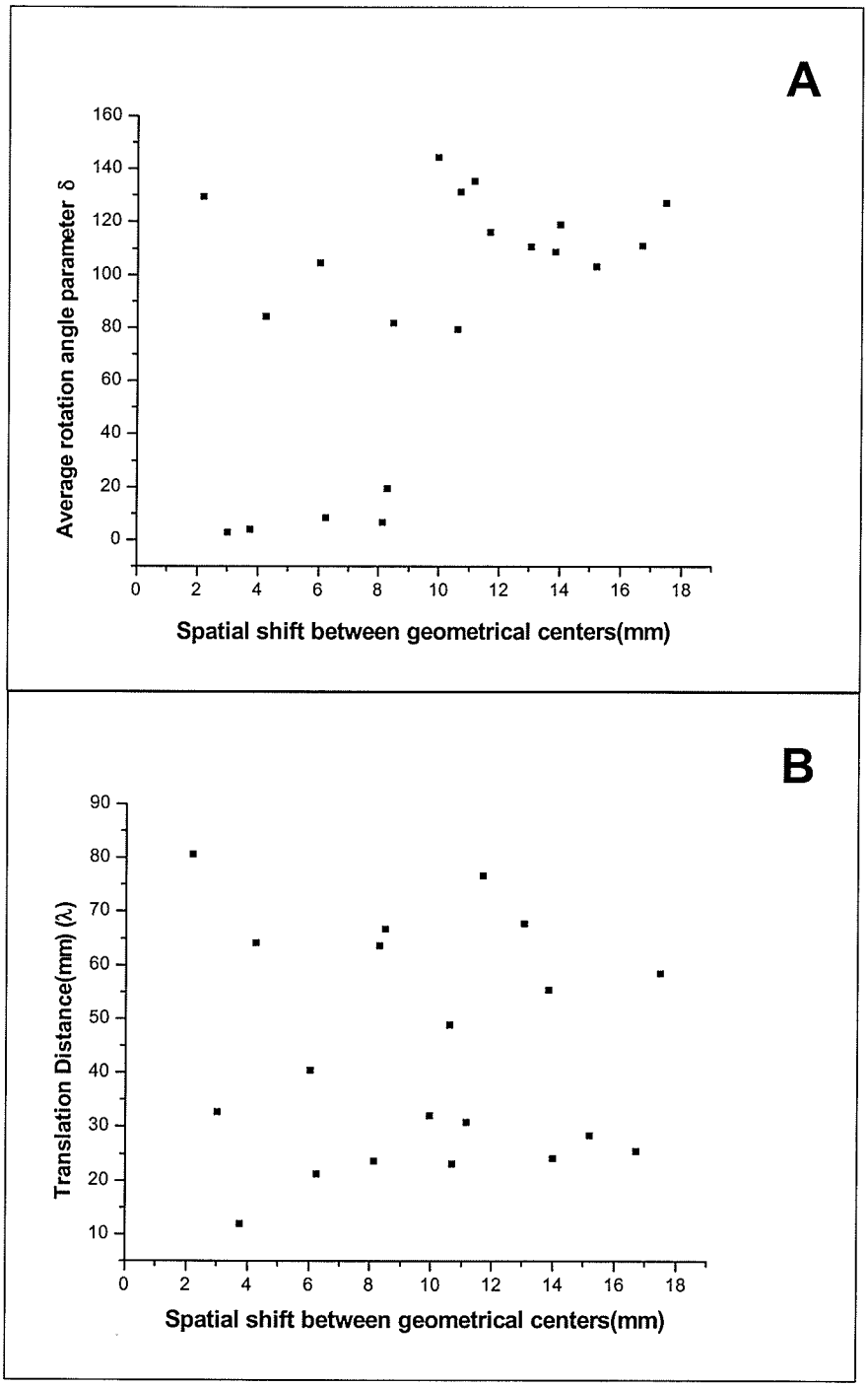

Figure 4-4 A: A graph of the rotation angle vector (δ) versus the spatial shift between geometrical centers (mm). The rotation vector is defined as the root mean square of each azimuthal angle. **B:** A graph of the translation distance (λ) versus the spatial shift between geometrical centers (mm).

4.6 Conclusion

It has been previously demonstrated that image fusion is a useful step in the treatment planning process, generally leading to increased accuracy of target delineation [Am99]. Clearly, accurate delineation of the tumour volume is essential to ensure that the prescribed dose is delivered to the correct volume. Inaccurate target volume definition may result in lower patient outcome (e.g. reduced life span and/or relapse) [Ro98]. In this work two clinically utilized methods of performing image fusion for radiotherapy of brain cancer are compared, these being a digital image fusion and a non-digital image fusion technique. Quantification of the improvements in accuracy achieved with the digital image fusion process as compared to the non-digital image fusion process has enabled us to objectively assess these improvements. Very little correlation was found between the magnitude of rotations and translations used in the registration in the digital image fusion process, and the shifts of the GTV geometric centre's, thus indicating that, for the brain site, little would be gained by attempting to modify diagnostic imaging procedures to ensure patient position was more similar to that in CT simulation. Estimates of contouring time required for the two methods indicate that only a small reduction (~30 seconds) is achieved using the digital image fusion versus the non-digital image fusion.

The data demonstrate that while volumetric differences between GTV's identified with the two methods may be typically small (mostly <20%), geometric centre shifts are larger (2-17 mm), and resulting maximum geometric miss estimates are even more significant (5-35 mm). Even when compared with the relatively large margins (15-25 mm), used for brain GTV to PTV expansions these potential geometric misses are significant. Based on the results of this work it is recommended that digital image fusion be used instead of non-digital image fusion in the treatment planning process for all brain tumor patients.

CHAPTER 5

Fast Three Dimensional Non-Linear Warping: Target Localization of Intraprostatic Lesions using Magnetic Resonance Spectroscopic Images

5.1 Abstract

Image registration is an important step in the radiotherapy treatment planning process. It provides a method of incorporating different types of diagnostic imaging information. One such application is to combine magnetic resonance spectroscopic images of the prostate with computed tomography images that are routinely used in the radiation treatment planning of prostate cancer. MRSI provides *in vivo* information related to the underlying metabolic activity of tissues, and can be related to the presence of cancer. However, the inflated endorectal coil required during MRS imaging poses a potential problem by deforming the prostate when it is filled with ~100cc of air during image acquisition. This pushes the prostate superiorly/anteriorly, deforming the prostate and consequently the spectroscopic imaging data in a non-linear manner. Since patients receiving radiation treatment for prostate cancer will not have their prostate deformed in this way, we propose the application of a non-linear mapping to the MRS image data, in order to localize this information accurately. In this application, the coil-deformed MRS images are warped back to a non-deformed state. A non-linear warping algorithm is presented to achieve this. Results indicate that the algorithm attains an accuracy of 97% (3 cc difference) when reproducing the total prostate volume compared to a Radiation Oncologist defined prostate volume. This difference is smaller than the measured intra-operator variance of ±7.4 cc (deflated coil) and the measured algorithm variance of ±4.0 cc.

5.2 Introduction

At some centers, MRS image data are now being used to identify areas of increased metabolic activity within the prostate treatment volume. Within the prostate, elevated levels of choline relative to that of citrate (choline/citrate ratio of 2.1±1.3) have been hypothesized as an indicator of an active tumour [Ku95][Ku96]. In another recent study by He *et al*, it was shown that MRS imaging can be used in to identify specific genetic and metabolic changes that occur in malignant tumours [He04]. Therefore, not only can MRS imaging identify specific genetic and biochemical changes but also can define different metabolic tumor types phenotypes. Thus, when combined with anatomical magnetic resonance imaging (MRI), MRS imaging improves the diagnostic specificity of malignant human tumours and is becoming an important clinical tool for cancer management and care [He04]. Evidence has been shown that in the extracapsular region MRS aids in identification of active tumour regions [Yu99]. The MRS images of the prostate are acquired using an endorectal coil, which is required to increase the signal to noise ratio of the resulting spectroscopic data. The spectroscopic data is then digitally presented as a shaded overlay on the anatomical magnetic resonance image acquired in the same imaging session, as demonstrated in figure 5-1. Using this information, the Radiation Oncologist can then define an intraprostatic lesion. Once an active tumour region is identified, higher dose may be delivered to that region in an effort to obtain increased local control. For example, a recent study showed the feasibility of intensity modulated radiotherapy (IMRT) to deliver increased dose (up to 90 Gy) to two intraprostatic lesions, while treating the entire prostate to 73.8 Gy, and keeping the dose to the rectum and bladder below tolerance [Xi01].

The endorectal coil, although required by the MRS imaging, poses a potential problem for the radiotherapy treatment planning of the prostate [Di02]. The coil deforms the prostate as it is filled with approximately 100cc of air required for image acquisition. This pushes into the prostate superiorly/anteriorly, and deforms the prostate, as illustrated in figure 5-1. Consequently the spectroscopic imaging data is deformed as well. Routine radiation treatment planning of the prostate relies on CT images to provide patient

density information needed to perform accurate dose calculations. These CT images of the prostate do not experience the same deformation as the MRSI data. The deformation in the MRS image data will not allow accurate anatomical coincidence when trying to register the deformed MRS image information with the non-deformed CT image data. We propose the following solution: (1) Acquire two sets of images during the MRS imaging session. Image set one is the MRS image data set, with the spectroscopic data overlaid on the anatomical data and the endorectal coil inflated. Image set two is a T2-weighted MR image of the prostate with the endorectal coil deflated (illustrated in figure 5-1c). (2) Using the anatomical information from the T2 weighted MR image, where the prostate is not deformed, correct the nonlinear deformations that are present in the MRS image data and create a set of *corrected images*. (3) Use rigid body (i.e. linear) transformations to then register the set of corrected images to the CT image data. The deformation of the prostate can not be described by simple linear rotations and translations [Me97]. Thus, in order to utilize the MRS image information accurately in the treatment planning process a non-linear mapping of the MRS image data is required. This will warp the deformed MRS images back to a non-deformed state that is more representative of the prostate anatomy in the CT image data. In this work a non-linear warping algorithm is presented to allow MRS image data to be incorporated into the radiation treatment planning process. The method is based on thin-plate-splines and a manual selection of control points, that is simple and fast to operate. A novel method of verifying the correctness of the warping algorithm is also presented. In addition, delineations of the prostate gross tumour volume, as performed by the Radiation Oncologist are investigated to determine the amount of intra-operator variability.

5.3 Methods and Materials

5.3.1 Data Acquisition

Three data sets were obtained from a single patient. An MRS data set was acquired with a 1.5T whole body scanner[4], with the use of an inflatable endorectal coil. After the MRS acquisition, two supplementary T2-weighted MR image data set were acquired, with a voxel size of 0.98x0.98x3.0 mm. The first of these two anatomical data sets was acquired with the endorectal coil fully inflated, while the second data set was acquired with the coil fully deflated, but still present in the rectum.

The raw spectroscopic data, and the reconstructed images of the two T2 weighted image sets were analyzed with the software package SAGE 7[5] (Spectroscopy Analysis by General Electric). In the analysis a spectral phase-encode grid of 16x8x8 was chosen, with voxel sizes of 7x7x7 mm in the MRS image data set. The resulting spectroscopic data from the analysis was represented as a spectral grid overlaid on the T2 weighted MR images of the prostate. Based on the spectral grid an intensity mapping of the positive spectroscopic regions was made. Within each grid location, the choline/citrate ratio is calculated. If the ratio reaches or surpasses the specified threshold value (i.e. 2.1±1.3) the region is marked positive. Depending on the value of the ratio in that region, a grayscale intensity value is assigned. Software was developed in house to export the "overlaid images" in DICOM 3 standard in order to meet the requirements of the treatment planning system[6]. Samples of the overlaid images, and both T2 weighted images can be seen in figure 5-1.

[4] Genesis Signa, General Electric Medical Systems.
[5] SAGE 7, Spectroscopy Analysis by General Electric, © 1998 General Electric
[6] Pinnacle[3], Philips Medical Systems.

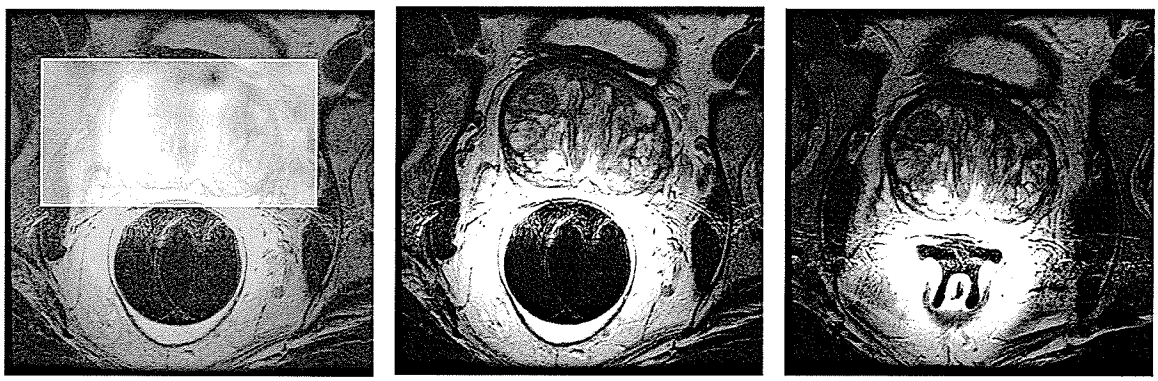

Figure 5-1 Sample images acquired from one patient. (A) The intensity mapping of the spectroscopy data overlaid on top of a T2 weighted MR image with endorectal coil inflated. (B), and (C) are two other data sets acquired during the MRS image acquisition. In image (B) the endorectal coil is inflated with ~100cc of air, while in (C) the endorectal coil is deflated.

5.3.2 Image registration method

Once the data sets have been acquired, a non-linear registration method is employed to account for the differences in tissue deformation of the prostate between the coil inflated and coil deflated situations. The registration method requires contouring of the inflated and deflated image data sets, GTV_{inf}, and GTV_{def} respectively. The inflated *MRSI/MR* images are aligned to the deflated images in the superior/inferior direction so that the prostate extent along the superior/inferior axis in both the inflated and deflated image set anatomically coincide. Following this, an operator performs contour-guided selection of control points, matching the GTV_{inf} to the deflated $GTV_{def.}$

These control points are input into a thin-plate-spline warping algorithm and the resulting mapping is applied to the $MRSI/MR_{inf}$ data set. The resulting data set removes the distorting effect of the inflated endorectal coil. This set of 'corrected' MRSI/MR images can then be registered to the CT images used for treatment planning. This approach is illustrated in the flow chart shown in figure 5-2. Each step will be discussed in more detail in the following sections.

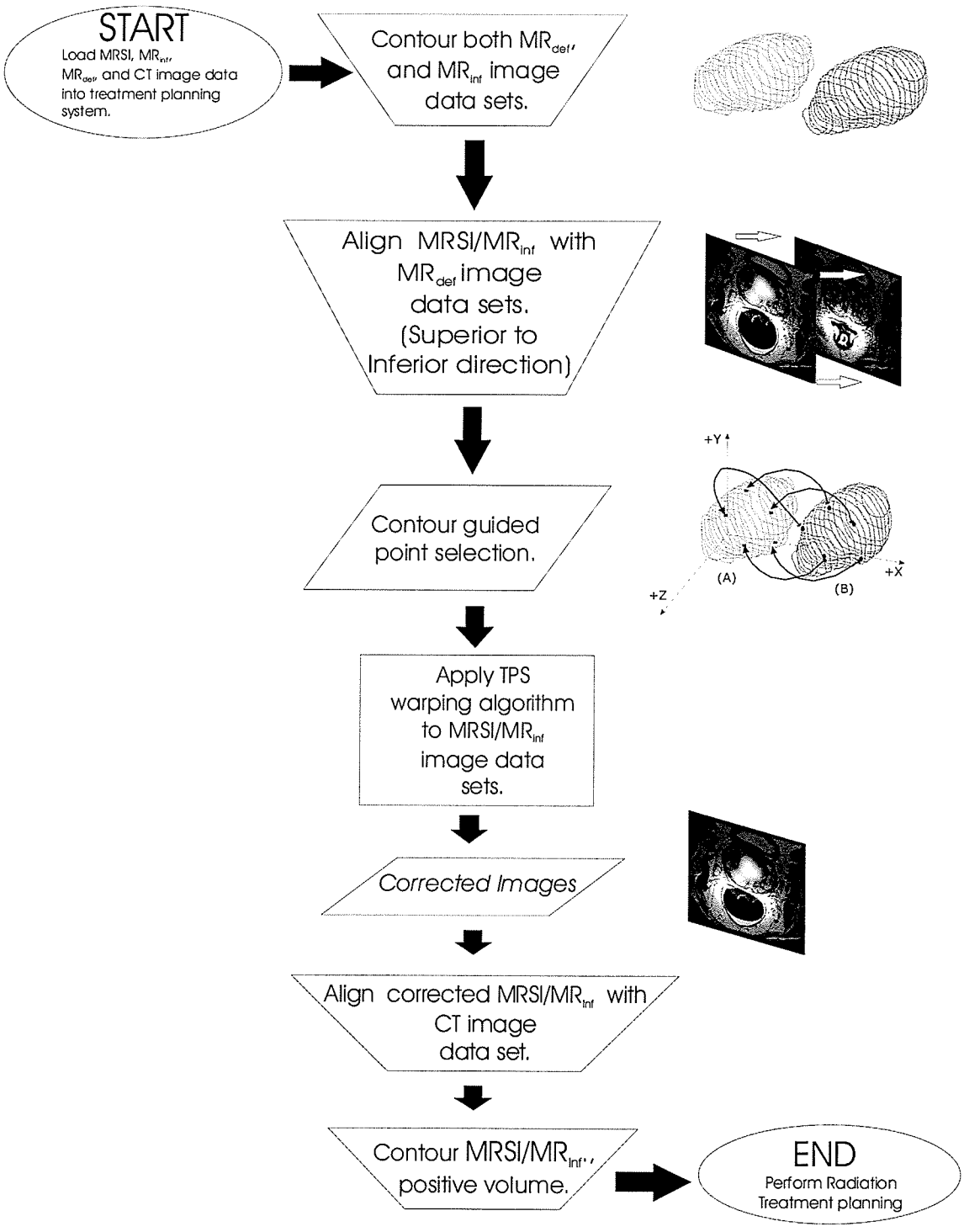

Figure 5-2 Flowchart of the image registration method.

5.3.3 Rigid Body Alignment

In the second step of the process, the MR_{inf} and MR_{def} volumes are aligned along the superficial axis. The T2 weighted images of the prostate with the endorectal coil provide much higher soft tissue contrast of the prostate than normally provided by routine pelvic scans which do not employ an endorectal coil [Ko87]. The increased internal detail of the prostate makes it relatively easy to identify and contour the prostate, even at the apex and base. Consequently, it is straight forward to align the MR_{inf} and MR_{def} in the superior/inferior directions. In this patient data set a shift of 6mm in the superior/inferior direction was required. This is illustrated in figure 5-3.

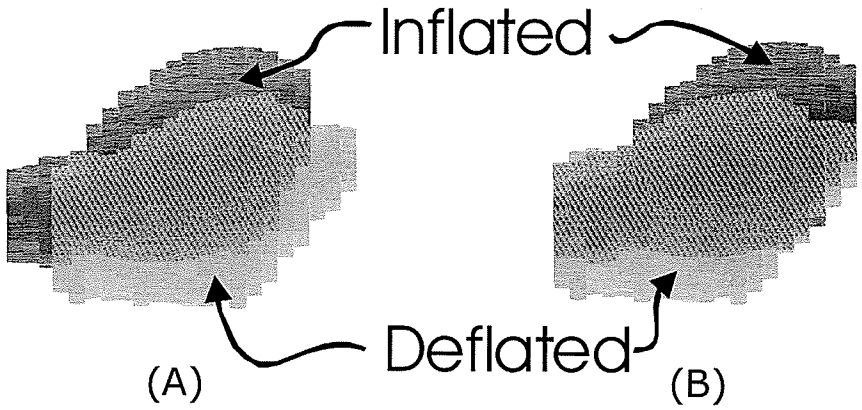

Figure 5-3 The images (A) and (B), are volumetric representations of the prostate GTV's. The GTV_{def}, is shaded in light grey, while the GTV_{inf} is shaded in dark grey. In (A) the prostate GTVs are not anatomically aligned. A 6mm shift in the superior/inferior direction aligns the anatomy of the prostate. Finally in (B) the two volumes are aligned anatomically.

5.3.4 Target delineation and Intra-operator Variability

The purpose of having the RO contour the prostate is two-fold. First, the contours of the prostate will be used to guide the selection of control points. Limiting control point choice to the RO defined contour ensures the dewarping is as anatomically accurate as possible. Secondly, the physician contour of the prostate GTV_{def} and GTV_{inf} form a gold

standard which can be used to assess the accuracy of the registration algorithm. A single RO performed the GTV contouring directly on the inflated and deflated MR image data sets. Over a period of time, the RO contoured both data sets 10 times. These ten data sets can be then used to determine the baseline intra-operator variability that exists in target delineation of the prostate using MR images with an endorectal coil present.

5.3.5 Control points selection

Control points for the TPS algorithm were selected from each transverse slice through the prostate, based on the anatomical structure of the prostate and the contour information. Ten control points $\{X_I, Y_I\}$ were selected from each slice of the MR_{inf} image set, and ten corresponding control points $\{X_0, Y_0\}$ were then selected from each slice of the MR_{def} image set. Once the control points were identified, the *corrected images* could be generated utilizing thin plate splines by interpolating the $\{X_I, Y_I\}$ and $\{X_0, Y_0\}$ points over a regular grid. In this approach, some important assumptions are made: (a) Rotations occurring in-plane and out- of-plane for the prostate are assumed to be negligible. Rotations of approximately spherical organs, such as the prostate, are difficult to detect [Fo01]. (b) The most superior and inferior contours define the superior and inferior boundaries of the prostate with no curvature extrapolation. The uncertainty in this assumption depends on the slice thickness and the number of slices in each reference volume [Sc04]. Figure 5-4 illustrates the control point selection process.

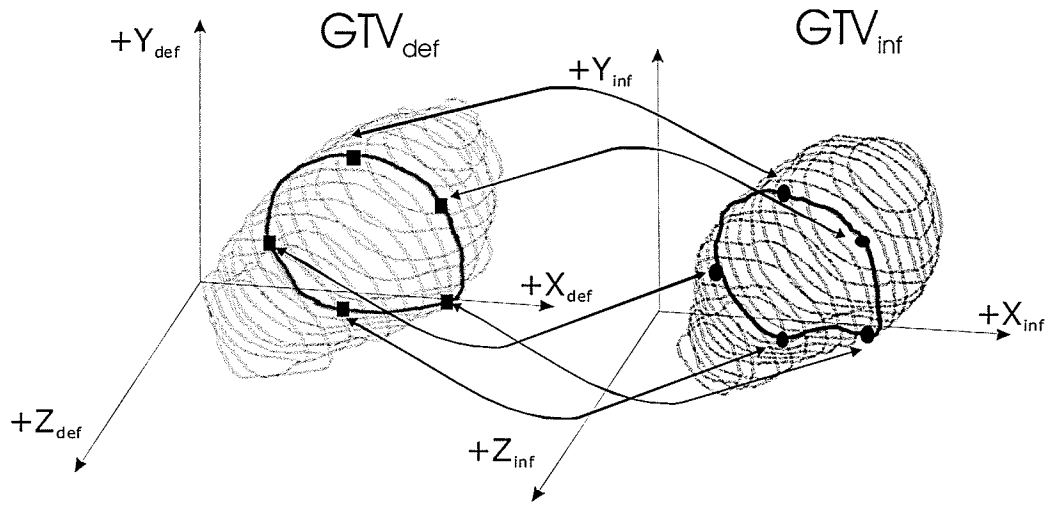

Figure 5-4 The light grey represents the set of contours that make up the GTV_{def}, while the dark grey represents the contours making up GTV_{inf} . "•" and "▪" marks the spot of five example control points $\{X_I, Y_I\}$ that are selected from the GTV_{inf}, and then matched to the corresponding anatomical positions $\{X_0, Y_0\}$ on the GTV_{def}.

5.3.6 Non-rigid transformation/TPS algorithm

The use of thin plate splines (TPS) is proposed to perform the non-linear mapping between image data sets where the coil is inflated and deflated or entirely absent. TPSs are ideal for modeling functions with local distortions which are too complex to be fit with polynomials [Me97][Go03]. Given n points (x_i, y_i) in the plane, a thin plate spline is defined as:

$$f(x,y) = a_0 + a_1 x + a_2 y + \frac{1}{2}\sum_{i=0}^{n-1} b_i r_i^2 \log r_i^2 \tag{5.1}$$

with the constraints:

$$\sum_{i=1}^{n-1} b_i = \sum_{i=1}^{n-1} b_i x_i = \sum_{i=1}^{n-1} b_i y_i = 0 \tag{5.2}$$

where $r_i^2 = (x-x_i)^2 + (y-y_i)^2$ and coefficients $\{a_0, a_1, a_2\}$ are fitting parameters for the TPS function [Ha01]. The TPS is a smooth function that has continuous first partial derivatives. It also grows almost linearly when far away from the points (x_i, y_i). The TPS surface passes through the original points $f(x_i, y_i)$. Once the TPS function is defined, it is applied to the MRS image data set to remove the distorting effect of the inflated endorectal coil. This ensures the prostate anatomy of the deflated endorectal coil, T2

weighted MR image data and the corrected MRS image data are aligned with one another. Final alignment with the CT simulation data set may be achieved using standard rigid body transformations. A sample of the corrected images can be seen in Figure 5-5.

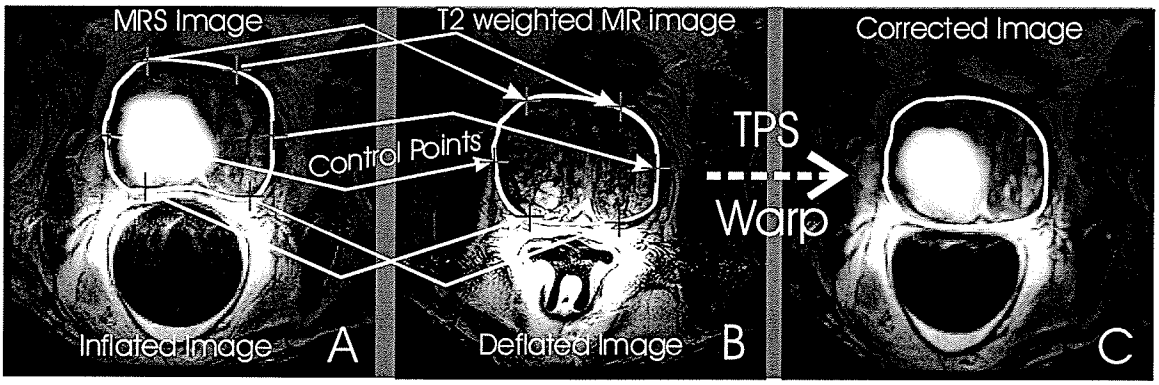

Figure 5-5 "+" marks the spot of the control points $\{X_I, Y_I\}$ that are selected from the MRS image set (inflated image) (A), and then matched to the corresponding anatomical positions $\{X_0, Y_0\}$ on the T2 weighted MR image (deflated image) (B). Once all control points are collected, a thin plate spline warping algorithm is applied to the inflated image to produce the corrected image in (C). In image (A) and (C), the white shaded region within the prostate represents the spectral overlay of increased choline/citrate. (An area in which there may be an intraprostatic lesion.)

5.4 Analysis

A novel method for assessing the accuracy of the image registration is presented. The prostate contours on the corrected image data set are directly compared to the Radiation Oncologist-defined prostate contours on the deflated coil data set (i.e. the gold standard data set). The volumes of complete coincidence, and the volumes that do not coincide were calculated. To assess the variability of control point selection for the non-linear registration method itself, the method was applied 10 times to the patient data set, and the standard deviation of the measured volumes was calculated. However, in order to place these values in context, the baseline variability in the RO defined contours was also estimated. To perform this calculation a sinlge RO contoured both the inflated and deflated prostate volumes 10 times.

5.4.1 Collected Data Summary

Analysis of the physician defined contours provides useful information about the image registration process and volumes of interest. The following data were collected:

- 10 GTV's of the prostate with endorectal coil inflated, and 10 GTV's of the prostate with endorectal coil deflated to form our *Gold Standard Set.*
- 10 GTV structures (10 sets of *corrected images*) generated from the non-rigid image registration method, using one set of contours from the gold standard and performing the non-rigid registration 10 times.

5.4.2 Evaluation of TPS algorithm

To assess the variation observed using the TPS algorithm, the following analysis was performed. Since the GTV's were aligned in the superior/inferior direction, the *corrected images* generated by the TPS algorithm may be compared on a slice-by-slice basis, and by the total volume. In theory, if the warping is performed exactly there should be zero difference between the gold standard GTV's, and the corrected GTV's.

Three quantities of interest are defined: volumes of complete coincidence, and positive and negative discrepancy. The variables corresponding to the volumes are $V_{coincidence}$, $V_{positive}$ and $V_{negative}$ respectively. See figure 5-6 for illustration. The volume of coincidence is defined as:

$$V_{coincidence} = V_{Gold\ Standard} \cap V_{Corrected\ Images} \tag{5.3}$$

where $V_{coincidence}$ is the volume where the gold standard GTV intersects the *corrected* GTV. We define $V_{positive}$, as being the overlapping volume associated with the gold standard volume, and $V_{negative}$, the overlapping volume associated with the corrected images.

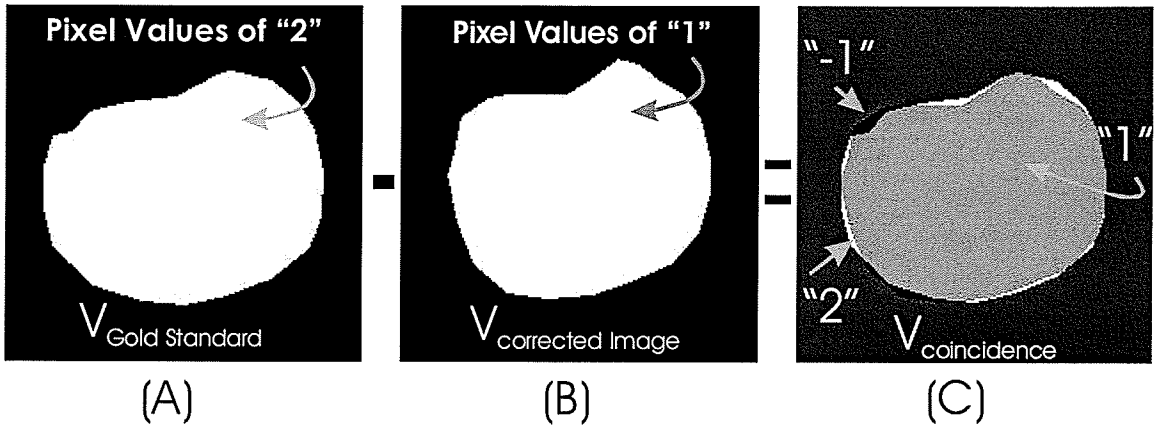

Figure 5-6: To compare two MR slices at the same location, a region filling algorithm uniquely identifies each pixel within the contour. Taking the 'gold standard' contour as the reference set, three unique identifiers are assigned to the difference image of the two filled contours. In (A) the volume of the gold standard is given a unique value of "2", while in (B) the corrected image is assigned a value of "1". The resultant difference of the two volumes gives (C). In (C) the light grey is the region of complete coincidence with values of "1". The regions in (C) that are white and black, are the regions of positive and negative discrepancies, respectively(i.e pixel values of "-1" and "2" respectively). These discrepancies correspond to regions of corrected prostate volume that are outside (white) and inside (black) the gold standard contour.

Accepting that the data follow a normal statistical distribution the standard deviation is then defined as:

$$S_{V_{coincidence}} = \sqrt{\frac{1}{N}\sum_{i=1}^{N}(V_{coincidence,i} - \bar{V}_{coincidence})^2} \tag{5.4}$$

where $\bar{V}_{coincidence}$ is the average coincidence volume over all trials. In this work the number of trials, N, is equal to 10. To measure the above volumes a region filling routine is employed [Go93]. The contours of the gold standard volume, are imported from the treatment planning system. The contours of the inflated prostate are embedded in the image data set. The total volumes for $V_{Gold\ Standard}$ and $V_{Corrected\ Images}$, are obtained by filling the region inside the contours with an unique voxel value, then multiplying the number of voxels in the filled region by the voxel volume. By subtracting the two sets of filled images from one another allows a calculation of the volumes of coincidence and positive/negative discrepancy, as illustrated in figure 5-6.

5.4.3 Intraoperator Variability

To assess the baseline variability in contouring the gross tumour volume for both the inflated and deflated prostate volumes, the same analysis is repeated for all 10 GTV_{inf} and 10 GTV_{def}. In order to perform this calculation, one GTV structure for each of the inflated and deflated sets is used as a reference volume set. Thus for the intraoperator variability assessment, the coincidence volume is,

$$V_{coincidence} = V_{\text{Reference}} \cap V_i \tag{5.5}$$

where V_i is the volume of the i^{th} trial, and $V_{Reference}$ is the volume to be used as the reference. Uncertainty is estimated by the standard deviation of the V_i's around $V_{Reference}$.

The purpose of the above analysis is to evaluate the reproducibility of the non-rigid image registration algorithm in a quantitative manner. Currently there are no standard techniques to evaluate the effect of the image registration on the GTV. In this analysis the physician contours of the deflated and inflated volumes are used as a set of gold standard gross tumour volumes. To put into perspective the accuracy of the proposed image registration method, the reproducibility of the selection of control points and the reproducibility of the GTV contouring by the Radiation Oncologist are assessed in this manner.

5.5 Results

5.5.1 Intraoperator variability

The results of the intra-operator analysis demonstrate that the RO was able to reproduce the total GTV_{inf} and GTV_{def} volumes with a high degree of certainty. This result was expected due to the enhanced contrast of the prostate MR images. The total prostate volume for the deflated gold standard was 107.0±1.2cc while the total prostate

volume for the inflated gold standard is 112.0±2.0cc. The total coincidence volume is 97.2±0.6cc , which translates to a 91% reproducibility. Similarly the reproducibility for the set of inflated prostate images was 89%. In figure 5-7, the plot of the average total volume per slice of both the inflated and deflated cases reveal that the total volume of the prostate is relatively conserved. Figures 5-7b and 5-7c contain the total volume per slice for all 10 trials of both the inflated and deflated cases. In both cases, the ability of the RO to contour the GTV within the slice seems reasonably constant from superior to inferior direction. At the same time the positive and negative discrepancies make up a small portion of the total volume. In the GTV_{def} volume the positive discrepancy was 6.1%, while the negative discrepancy was 8.9%. Similar results were obtained for the GTV_{inf} volume. In this case the positive discrepancy was 5.7% and the negative discrepancy is 11.1%. Welten *et al.,* reported that intraoperator variability can range as high as 10%, for experienced radiologists contouring anatomical structures with MRI image data [We01]. In light of this, these discrepancy values correspond well with literature values.

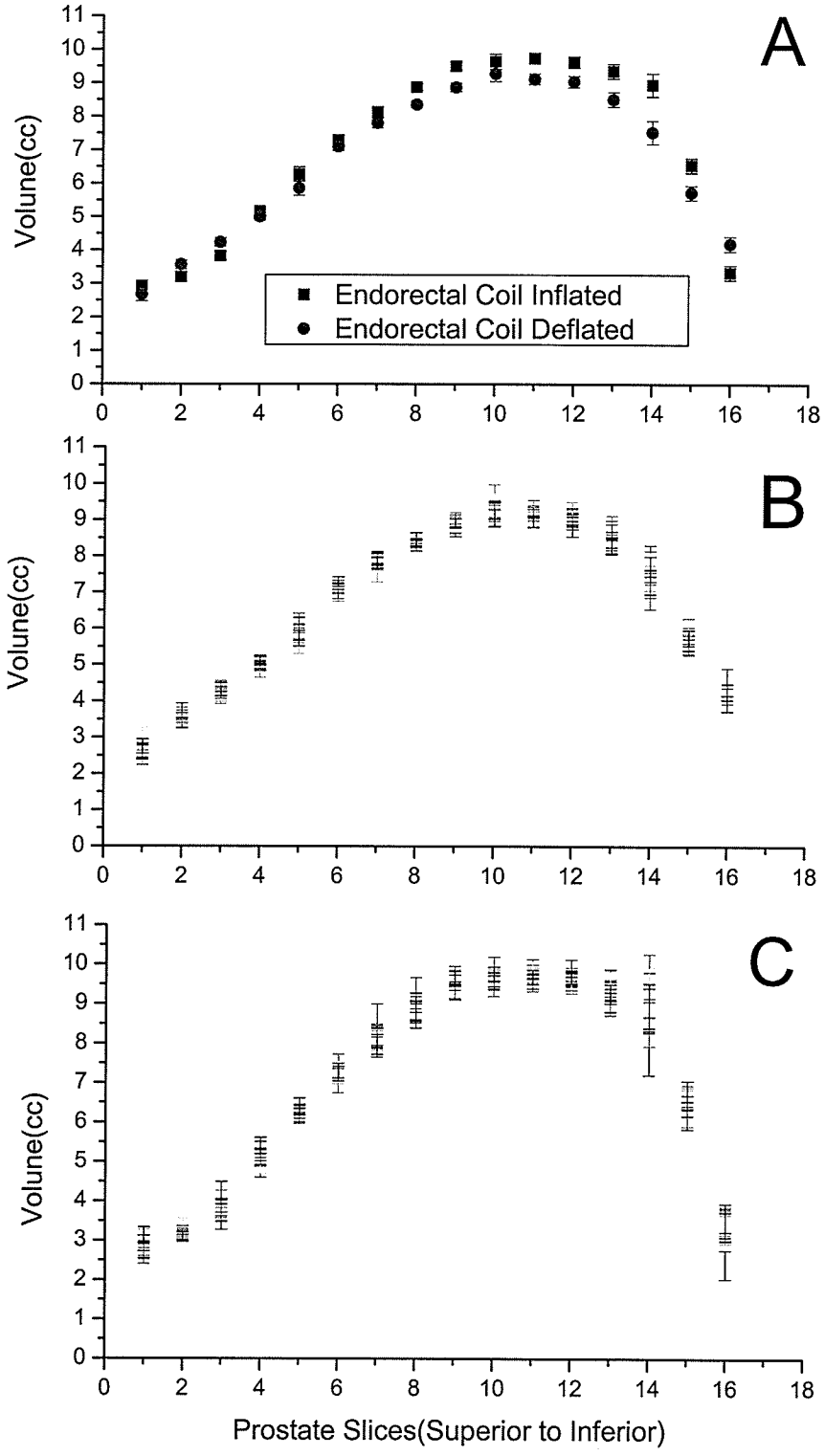

Figure 5-7 In (A) the average volume per slice is presented for the deflated and inflated GTV's volumes. In (B) and (C), all 10 trial volumes per slice are presented for the inflated and deflated GTV volumes.

5.5.2 TPS algorithm Variability

The results of the analysis of the control point selection variability are summarized in Table 5-1. The results show that on average 97% (or 99.5±0.8cc) of the prostate volume is conserved when compared to the gold standard volume. The TPS corrected GTV volumes compare well to the total volume of the gold standard GTV_{def}. The gold standard volume was 103.1 cc, which encompasses most of the TPS corrected volumes, as demonstrated in Figure 5-8. In comparison to the average total TPS volume, which was also 103±1 cc's, the algorithm's ability to conserve the total GTV volume accurately is within error.

The positive and negative discrepancies correspond to only 3.5% and 3.7 % respectively of the TPS total volume. This result is significantly smaller than the discrepancy found in the gold standard volume (~3-5% difference). This may indicate a small systematic error in the TPS warping algorithm. Considering the eventual addition of a margin to account for beam geometry and positional movements (planning target), we can expect that the small discrepancy volumes would have a negligible impact.

		Total Prostate Volume(cc)	**Coincidence Volume(cc)**	**Positive Discrepancy Volume(cc)**	**Negative Discrepancy Volume(cc)**
Intraoperator Variance	Deflated	107.0±1.2	97.2±0.6	6.6±0.6	9.5±0.9
	Inflated	112.0±2.0	99.3±1.0	6.4±1.0	12.5±1.1
TPS Algorithm	Warped Image	103.0±1.0	99.5±0.8	3.6±0.8	3.8±0.5

Table 5-1 The results of the intraoperator variance were based on the result of a single RO contouring both the deflated and inflated prostate volumes 10 times. The TPS warping algorithm, utilizes the contour information based on the RO's prostate delineation, and was tested repeatedly 10 times to evaluate its accuracy.

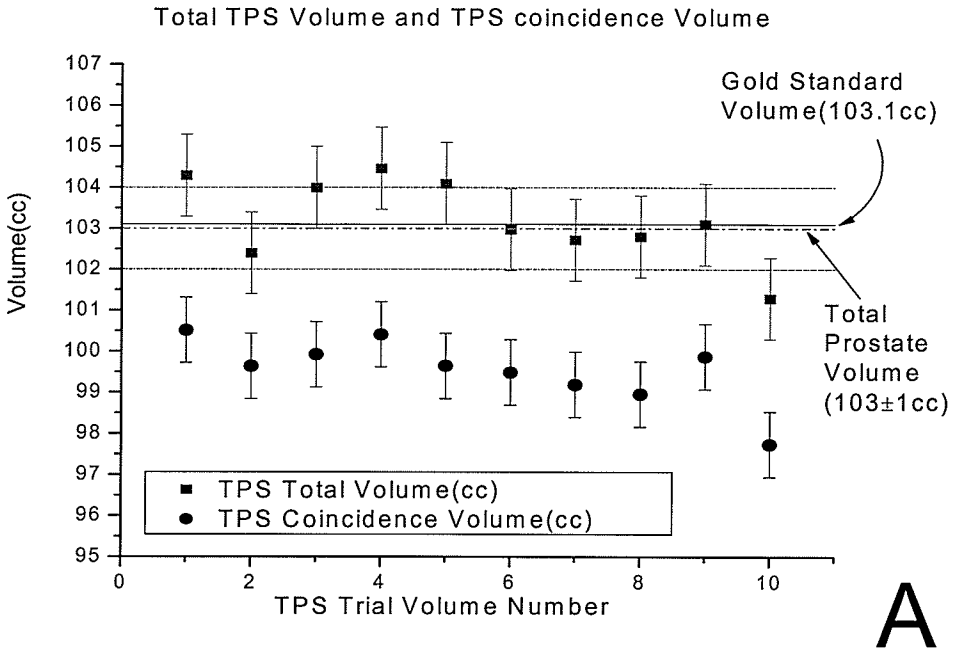

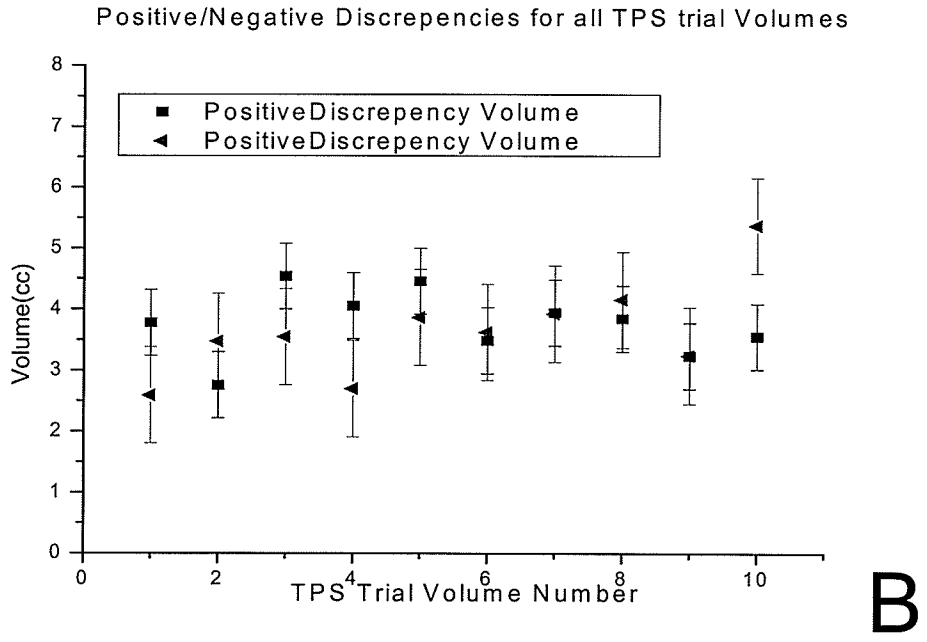

Figure 5-8 In (A) the total TPS volume is presented along with the volume of coincidence. Within error, the total coincidence volume is the same as the gold standard volume. The "gold standard" volumes particular reference volume that was chosen from the data set. In (B) the positive and negative discrepancies per trial are shown, and represents only a small percentage (~3-5%) of the total TPS volume.

5.7 Discussion and Conclusion

In this work we have demonstrated a fast and simple method of incorporating MRS image information into the treatment planning process. Current approaches using deformable models require extensive time to develop, and long computational times to implement over three dimensional volumes. Recent reports indicate calculation times varying from 20-40 minutes [Wu03, Fe03]. These times do not include the time to contour and choose the control points, if needed. The method proposed in this work is very simple and the warping algorithm operates in nearly real time (<10 s). TPS's have been used previously in radiographic imaging to account for 2D variations [Fa03]. Specifically relating to prostate and warping in 3D, Meyer *et al* [Me97] and Fei *et al* [Fe03] report successful application of TPS warping techniques. As well, recent studies investigating this deformation in the prostate have used a phantom based approach [Li03]. While this may provide some useful information in algorithm development, using acquired patient data with the coil inflated and deflated as performed here, provides the most reliable approach to testing any warping algorithm. Having the radiation oncologist performing the contouring of the prostate also provides a clinically relevant gold standard.

The intra-operator variance was found to be ±1.2 cc (or ±1.1%) and ±2.0 cc (or ±1.8%) of the total prostate volume in the deflated coil and inflated coil cases respectively. Comparing the total prostate volume and the coincidence volume, the Radiation Oncologist is able to consistently reproduce 91% and 89% of the deflated coil and inflated coil prostate volumes respectively. The delineation of the edges of the prostate demonstrates some variability that shows up in the positive and negative discrepancy volumes. The average prostate volume reproduced by the warping algorithm was 99.5±0.8 cc, only 3.5 cc different than the gold standard prostate volume. The

variability in the algorithm application was smaller than the intra-operator variability, as indicated by smaller volumes of positive and negative discrepancy. The results indicates that the proposed method is robust with respect to operator selection of the control points required for the warping algorithm. While future work will investigate the feasibility of deformable registration algorithms to solve this problem, the results obtained using a simple and easily implemented thin-plate-spline algorithm as investigated here operates with high reproducibility.

CHAPTER 6

Summary

6.1 Conclusion

Image registration is a method of combining different diagnostic imaging modalities (i.e., PET, CT, MRI, MRS, etc...). Due to recent commercial availability, image registration software was clinically implemented at CancerCare Manitoba in September 2001. The addition of imaging data that is registered to the routine CT simulation data has changed the process by which treatment volumes are delineated. For example, the image registration of MRI to the CT simulation images of the brain, allows a physician to delineate the target volumes directly on the MRI image data set, which has much higher soft tissue contrast than CT. Image registration function's to assist in target localization. It has been previously demonstrated that image registration is a useful step in the treatment planning process, generally leading to increased accuracy of target delineation [Am99]. Clearly, accurate delineation of the tumour volume is essential to ensure that the prescribed dose is delivered to the correct volume. Inaccurate target volume definition may result in lower patient outcome (e.g. reduced life span and/or relapse) [Ro98]. Errors that are introduced in the image registration step will be propagated forward into the treatment planning, and ultimately into the patients treatment. This thesis is composed of three main areas of investigation on issues that encompass the use of image registration in the radiation treatment planning. We investigate various aspects of the accuracy of past, current, and future applications of image registration as used in radiation therapy.

In chapter 3, a phantom was presented to perform quality assurance checks. The phantom contain orthogonal arrays of acrylic rods with spacing designed to be 3.0cm. CT and MR image data was acquired using clinical scanning equipment and parameters

typical of brain patients. The geometric uniformity of the CT and MR phantom image data was assessed by measuring the distance between the rod centers. Average values of 3.00±0.02cm in the CT data set, and 2.98±0.10cm in the MR data set in the transverse direction were obtained. This indicates the CT image data possess excellent geometric uniformity, while the MRI data demonstrate very good geometric uniformity.

Using standard techniques to calculate the image registration error, the fiducial registration error (FRE) was also calculated. For the transverse direction, the FRE was calculated to be 1.0±0.6mm. Therefore, for most intracranial lesions the accuracy of the registration can be within the size of a single voxel. To ensure and monitor geometric accuracy within the imaging modalities, it is recommended that the QA phantom be used for periodic assessments of the image registration process. This will be an important part of the overall QA program for the radiation therapy process.

Following in chapter 4, a retrospective study was performed to evaluate the effect of introducing digital image registration into the treatment planning of brain tumours at CancerCare Manitoba. In this work two clinically utilized methods of performing image fusion for radiotherapy of brain cancer are compared, these being a digital image fusion and a non-digital image fusion technique. Quantification of the improvements in accuracy achieved with the digital image fusion process as compared to the non-digital image fusion process has enabled us to objectively assess these improvements. Shifts between the digital fusion and non-digital fusion target's geometrical centers ranged from 2 mm to 15 mm. Volumetric differences in the targets ranged from 1 cm^3 to 112 cm^3. Had treatment proceeded using the non-digital image fusion technique, it is estimated that maximum geometric misses ranging from 2mm to 36mm would have occurred. There is a significant improvement in target delineation when using digital image fusion as compared to previous, non-digital image fusion methods. The data demonstrate that while volumetric differences between GTV's identified with the two methods may seem small (mostly <20%), geometric centre shifts can be significant (2-17 mm). Resulting maximum geometric miss estimates are even more significant (5-35 mm). Even when compared with the relatively large margins (15-25 mm) used for brain GTV to PTV

expansions these potential geometric misses are significant. Based on the results of this work it is recommended that digital image fusion be used instead of non-digital image fusion in the treatment planning process for all brain tumor patients.

In Chapter 5, the use of a non-rigid registration algorithm was investigated to introduce MRS imaging to the radiation treatment planning of the prostrate. A fast and simple method of incorporating MRS image information into the treatment planning process is presented. Current approaches using deformable models require extensive time to develop, and long computational times to implement over three dimensional volumes. The method proposed in this work is very simple, based on thin-plate-splines (TPS), and operates in nearly real time (<10 s). Thin-plate-spline's have been used previously in radiographic imaging to account for 2D variations [Fa03]. A single radiation oncologist performed repeated contouring of the prostate GTV's, providing a clinically relevant gold standard. By analyzing these contours, the intra-operator variance was found to be ±1.2 cc (or ±1.1%) and ±2.0 cc (or ±1.8%) of the total prostate volume in the deflated coil and inflated coil cases respectively. Comparing the total prostate volume and the coincidence volume, the Radiation Oncologist is able to consistently reproduce 91% and 89% of the deflated coil and inflated coil prostate volumes respectively. The delineation of the edges of the prostate demonstrates some variability that shows up in the positive and negative discrepancy volumes. The average prostate volume reproduced by the warping algorithm was 99.5±0.8 cc, only 3.5 cc different than the gold standard, physician defined prostate volume of 103.1cc. The variability in the algorithm application was smaller than the intra-operator variability, as indicated by smaller volumes of positive and negative discrepancy. The results indicate that the proposed method is robust with respect to operator selection of the control points required for the warping algorithm. The work in this chapter demonstrates the feasibility of incorporating MRSI data into routine radiation treatment planning in the prostate.

6.2 Future Work

The work performed in Chapter 3 and 4 is reasonably self-contained and completed. However, the investigation in Chapter 5 has great potential to be improved upon and brought into routine clinical use. To achieve this, the next step is to investigate the use of deformable models as an alternative and more general solution to this problem. Deformable models are a popular and vigorously researched model-based approach to computer-assisted, medical image analysis. Deformable models have the ability to segment, match and track images of anatomic structures by exploiting constraints derived from the image data together with *a priori* knowledge about the location, size and shape of structures of interest [Te97]. Deformable models are capable of accommodating the often significant variability of biological structures over time and across different individuals. Furthermore, they support highly intuitive interaction mechanisms that allow medical scientists and practitioners to bring their expertise to bear on the model-based image interpretation task as necessary.

The next step in this project's evolution, will be to design a deformable model which provides a more sophisticated and general solution to the problem of incorporating MRS data into clinical treatment planning of the prostate.

References

[Am99] R. Amdur, D.Gladtsone, *et al.* "Prostate seed implant quality assessment using MR and CT Image fusion." *International Journal of Radiation Oncology, Biology, and Physics.* 43: pp.67-72, 1999.

[Am03]American Cancer Society, Inc., "Cancer Facts & Figures 2003" , pp. 3-17, 2003.

[Am91]Y.Amit, U Grenander, and M. Piccioni. "Structural image restoration through deformable templates." *J. Am. Stati. Ass.*, 86(414): pp.376-387, 1991.

[As99]J. Ashburner, and K.J. Friston. "Nonlinear spatial normalization using basis functions." *Human Brain Mapping*, 7: pp.254-266, 1999.

[Ba92] C. J. Baker, M. A. Moerland, R. Bhagwandien, and R. Beersma, "Analysis of machine dependent and object-induced geometric distortion in 2DFT MR imaging,"*Magn. Reson Imaging* 10, pp.597-608, 1992.

[Be99] G. Bednarz, M. B. Downes, B. W. Corn, W. J. Curran, and H. W. Goldman, "Evaluation of the spatial accuracy of magnetic resonance imaging-based stereotactic target localization for gamma knife radiosurgery of functional disorders," *Neurosurgery* 45: pp. 1156-61,1999.

[Bo99] S. Bonavita, *et al.* " Proton MRS in neurological disorders" *Eur J Radiol*, 30: pp125-131, 1999.

[Bo91] F.L, Bookstein. "Thin-plate spline and the atlas problem for Biomedical Images." *In Information Processing in Medical Imaging: Proc, 12th International Conference* (IPMI'91), pp. 326-342, 1994.

[Bo93] F.L. Bookstein, and W.D.K Green. "A feature space for edges in images with landmarks." *J. Math. Imaging and Vision*, 3: pp. 231-261, 1993.

[Br82] T.R. Brown, *et al*, "NMR chemical shift imaging in three dimensions" *Proc. Natl. Acad. Sci.*, 79:pp 3532-3526, 1982.

[Ca02] Peter R. Carrol, and Gary Grossfeld, American Cancer Society Atlas of Clinical Oncology Prostate Cancer, 2002.

[Ca03]Statistics Canada. Cancer Statistics. Ottawa: Health Statistics Division,Catalogue 84-601-X1E, 2003.

[Ch02] H.Chen, and P.K.Varshney. "Registration of multimodal brain images: Some experimental results." *In Proceedings of SPIE Conference on Sensor Fusion: Architectures, Algorithms, and Applications* VI , April 2002.

[Co95] A.Collignon, F.Maes, D.Delaere, D.Vandermeulen, P.Suetens, and G.Marchal. "Automated multi-modality image registration based on information theory." *Information Processing in Medical Imaging* , 1995.

[Co94] D.L. Collins, P. Neelin, T.M. Peters, and A.C. Evans. "Automatic 3D intersubject registration of MR volumes in standardized Tailraich space." *J. Math. Imaging and Vision* 18(2) : pp. 192-205 ,1994.

[Co53] R.Courant, and D.Hilbert, Eds. Methods of Mathematical Physics, vol. 1. Interscience, London, 1953.

[Du76] J. Duchon. "Interpolation des functions de deux variables suivant les principes de la flexion des plaque minces." *RAIRO Analyse Numerique*, 10: pp. 5-12, 1976.

[Ed86] W.A. Edelstein, et al.. "The instrinsic signal-to-noise ratio in NMR imaging." *Magnetic Resonance in Medicine*, 3: pp. 604-618, 1986.

[Fa03] Fantozzi S, Cappello A, Leardini A. "A global method based on thin-plate splines for correction of geometric distortion: an application to fluoroscopic images." *Medical Physics.* Feb. 30(2): pp. 124-31, 2003.

[Fe03] Fei B, Kemper C, Wilson DL. "A comparative study of warping and rigid body registration for the prostate and pelvic MR volumes." *Comput. Med. Imaging. Graph.* 27(4): pp. 267-81, 2003.

[Fi98] Fitzpatrick, J.Michael, B.West, Jay, and R.Maurer, Calvin. "Predicting error in rigid-body point-based registration." *IEEE.Trans.Med.Imag.* 17: pp. 112-124 1998.

[Fo01] Fontenla E, Pelizzari C A, Roeske J C and Chen G T Y. "Numerical analysis of a model of organ motion using serial imaging measurements for prostate radiotherapy." *Phys. Med. Biol.* 46: pp. 2337–58, 2001.

[Fr89] J. Fraum, *et al.* "Localized high resolution proton NMR spectroscopy using stimulated echoes: intial applications to human brain in invivo", *Mag Res Med*, 9: pp. 79-93, 1989.

[Go93] Gonzalez R., and Woods R., "Digital Image Processing", *Addison-Wesley Publishing Company, Inc.*, California, pp 529-535 1993.

[Ha02] Hajnal JV, Hawkes DJ, Hill DG. (eds). "Medical Image Registration." *CRC Press,* Baton Rouge, Florida. June, 2001.

[He04] He Q, Xu RZ, Shkarin P, Pizzorno G, Lee-French CH, Rothman DL, Shungu DC, Shim H. "Magnetic resonance spectroscopic imaging of tumor metabolic markers for cancer diagnosis, metabolic phenotyping, and characterization of tumor microenvironment." *Dis Markers.* 19 (2-3): pp. 69-94, 2004.

[Ho97] N. Hosten, N. Bornfeld, R. Wamuth, "Uveal melanoma: detection of extraocular growth with MR imaging and ultrasound" *Radiology* 202: pp. 61-67, 1997.

[Ho98] N. Hosten, P. Wust, J. Beier, A. Lemke, R. Felix, "MRI-Assisted Specification/Localization of Target Volumes: Aspects of Quality Control" *Strahlentherapie und Onkologie* 174:Suppl II: pp. 13-18, 1998.

[Ka97] K. Kagawa, W. R. Lee, T. E. Schultheiss, *et al.* Initial Clinical Assessmet of CT-MRI Image Fusion Software in Localization of the Prostate for 3D Conformal Radiation Therapy. *International Journal of Radiation Oncology, Biology, and Physics*. 38(2): pp. 319-325, 1997.

[Kh00]V. S. Khoo, E. J. Adams, F. Saran, J. L. Bedford, J. R. Perks, A. P. Warrington, M. Brada, "A Comparison of Clinical Target Volumes Determined by CT and MRI for the Radiotherapy Planning of Base of Skull Meningiomas" *International Journal of Radiation Oncology, Biology, and Physics* 46(5): pp. 1309-1317, 2000.

[Kh00]V. S. Khoo, E. J. Adams, F. Saran, *et al.* A Comparison of Clinical Target Volumes Determined by CT and MRI for the Radiotherapy Planning of Base of Skull Meningiomas. *International Journal of Radiation Oncology, Biology, and Physics.* 36(5): pp. 1309-1317, 2000.

[Ko94]H. M. Kooy, M. Van Herk, P. D. Barnes, E. Alexander III, S. F. Dunbar, N. J. Radiotherapy and Radiosurgery Treatment Planning" *International Journal of Radiation Oncology, Biology, and Physics* 28(5): pp. 1229-1234, 1994.

[Ko92] D. Kondziolka, P. K. Dempsey, L. D. Lunsford, J. R. Kestle, E. J. Dolan, E. Kanal, and R. R. Tasker, "A comparion between magnetic resonance imaging and

computed tomography for stereotactic coordinate determination," *Neurosurgery* 30: pp. 402-407, 1992.

[Ko93] H. M. Kooy, M. Van Herk, P. D. Barnes, *et al.* "Image Fusion for Stereotactic Radiotherapy and Radiosurgery Treatment Planning." *International Journal of Radiation Oncology, Biology, and Physics.* 28(5): pp. 1229-1233, 1993.

[Ko87] Koslin DB, Kenney PJ, Koehler RE, Van Dyke JA. "Magnetic resonance imaging of the internal anatomy of the prostate gland." *Invest Radiol.* 22(12): pp. 947-53, 1987.

[Ku95] Kurhanewicz, J. et al. "Citrate as an in vivo marker to discriminate prostate cancer from benign prostatic hyperplasia and normal prostrate peripheral zone: detection via localized proton spectroscopy." *Urology* 45: pp. 459-466, 1995.

[Ku96] Kurhanewicz J. , Hricak H, Vigneron DB, et al. "Prostate cancer: Metabolic response to cryosurgery as detected with 3D H-1 MR spectroscopic imaging." *Radiology* 200: pp. 489–496, 1996.

[Ku96] Kurhanewicz J. , Vigneron DB, Hricak H, et al. "Three-dimensional H-1 MR spectroscopic imaging of the in situ human prostate with high (0.24–0.7-cm3) spatial resolution." *Radiology* 198: pp.795–805, 1996.

[Ku02] Kurhanewicz J., PhD, Mark G. Swanson, PhD, Sarah J. Nelson, PhD, and Daniel B. Vigneron, PhD, "Combined Magnetic Resonance Imaging and Spectroscopic Imaging Approach to Molecular Imaging of Prostate Cancer", *Journal of Magnetic Resonance Imaging* 16: pp. 451–463, 2002.

[La97]J. P. Lattanzi, D. A. Fein, S. W. McNeeley, A. H. Shaer, B. Movsas, G. E. Hanks, "Computed Tomography – Magnetic Resonance Image Fusion: A Clinical Evaluation of System Lesions" *Radiation Oncology Investigations* 5: pp.195-205, 1997.

[La97] J. P. Lattanzi, D. A. Fein, S. W. McNeeley, *et al.* Computed Tomography Magnetic Resonance Image Fusion: A Clinical Evaluation of an Innovative Approach for Improved Tumor Localization in Primary Central Nervous System Lesions. *Radiation Oncology Investigations.* 5: pp. 195-205, 1997.

[La96] H.Y. Lau, K. Kagawa, W. R. Lee, *et al.* Short Communication: CT-MRI image fusion for 3D conformal prostate radiotherapy: use in patients with altered pelvic anatomy. *The British Journal of Radiology*, 69: pp.1165-1170, 1996.

[Li03] J. Lian et al . "Integrating deformable MRI/MRSI and CT image registration into the prostate IMRT treatment planning." *Int J Radiat Oncol Biol Phys.* 57 : pp.207-217, 2003.

[Ma97] C.R.Maurer, Jr., J.M.Fitzpatrick, M.Y.Wang, R.L.Galloway, R.J.Maciunas, and S.Allen, George. "Registration of head volume images using implantable fiducial markers." *IEEE Trans.Med.Imag.* 4: pp. 8-21, 1997.

[Me97]C.R. Meyer, et al. "Demostration of accuracy and clinical versatility of mutual warped geometric deformations." *Med. Image. Anal.*, 1(3): pp. 195-207, 1997.

[Me79]J. Meingeut. "Multivariate interpolation at arbitrary points made simple." *Zeitschrift für angewandte Mathematik und Physik.* 30: pp. 292-304, 1979.

[Or99]R. C. Orth, P. Sinha, E. Madsen, G. Frank, F. R. Korosec, T. R. Mackie, and M. Mehta, "Development of a unique phantom to assess the geometric accuracy of magnetic resonance imaging for stereotactic localization," *Neurosurgery* 45; pp. 1423-1431, 1999.

[Pa83]S. Park and R. Schowengerdt, "Image Reconstruction by Parametric Cubic Convolution", *Computer Vision, Graphics & Image Processing* 23: pp. 256-270, 1983.

[Ph91] M. H. Philips, M. Kessler, F. Y. Chuang, K. A. Frankel, J. T. Lyman, J. I. Fabrikant, and R. P. Levy, "Image correlation of MRI and CT in treatment planning for radiosurgery of intracranial vascular malformations," *Int. J. Radiat. Oncol., Biol., Phys.* 20881-889, 1991.

[Pi00] D. Pickens. "Magnetic Resonance Imaging." *In Handbook of Medical Imaging: Volume I. Progress in Medical Physics and Psychophysics.* Bellingham, WA:SPIE Press, pages used 373-461, 2000.

[Ro98] J. Rosenman, E. Miller, G. Tracton, *et al* "Image registration an essential part of radiation therapy treatment planning." *International Journal of Radiation Oncology, Biology, and Physics.* 40(1): pp. 197-205, 1998.

[Ro96] K.Rohr, et al. "Pointing based elastic registration of medical image data using approximating thin plate splines." *4th International Conference Visualization in Biomedical Computing (VBC' 96)*, pages used 297-307, 1996.

[Sc04] Schaly B, Kempe JA, Bauman GS, Battista JJ, Van Dyk J. "Tracking the dose distribution in radiation therapy by accounting for variable anatomy." *Phys Med Biol.* 49(5): pp. 791-805, 2004.

[Sh48] C.E.Shannon, Ed. "The mathematical theory of communication (parts 1 and 2)" , *Bell Syst. Tech. J* , 27: pp. 17-27, 948.

[So01] M.Sonka, and J.M.Fitzpatrick, Eds. Handbook of medical imaging: Volume 2 medical image processing and analysis. SPIE Press. New York NY, 2001.

[St96] C.Studholme, D.L.G.Hill, and D.J.Hawkes. "Automated 3d registration of MR and CT images of the head." *Med.Image Anal.* 1: pp. 34-48, 1996.

[St97] C.Studholme, D.L.G.Hill, and D.J.Hawkes. "Automated 3D registration of MR and PET brain images by multi-resolution optimisation of voxel similarity measures." *Med.Phys.* 24: pp. 78-90, 1997..

[Sl80] C.P. Slichter, Principles of Magnetic Resonance, Springer-Verlag, Berlin Germany, 1980.

[Su94] T. S. Sumanaweera, J. R. Adier, Jr., S. Napel, and G. H. Glover, "Characterization of spatial distortion in magnetic resonance imaging and its implications for stereotactic surgery," *Neurosurgery* 35: pp. 696-704, 1994.

[Sz94] R. Szeliski and S. Lavallee. "Matching 3D anatomical surfaces with non-rigid deformations using octree-splines." *In IEEE Workshop on Biomedical Image Analysis*, pages used 144-153, 1994.

[Te97] Terzopoulus D, McInerney T. "Deformable models and the analysis of Medical Images", *Stud Health Technol Inform*, 39: pp. 369-78, 1997.

[Vi95] P.Viola, and W.Wells. "Alignment by maximization of mutual information." *In Proc.5th Int.Conf.Computer Vision* , 1995.

[Wo92]R.P.Woods, S.R.Cherry, and J.C.Mazziotta. "Rapid automated algorithms for aligning and reslicing pet images." *J.Comput.Assist.Tomogr.* 16: pp.154-168, 1992.

[Wo93] R.P.Woods, J.C.Mazziotta, and S.R.Cherry. "MRI-PET registration with automated algorithm." *J.Comput.Assist.Tomogr.* 17: pp. 197-206, 1993.

[Wo98] R.P.Woods,et al. "Automated image registrastration: II.Intersubject validation of linear and nonlinear models." *J.Comput.Assist.Tomogr.* 22(1) : pp. 153-165, 1998.

[Wa96] M.Y.Wang, C.R.Maurer, Jr., J.M. Fitzpatrick, and R.J.Maciunas. "An automatic technique for finding and localizing externally attached markers in CTand MR volume images of the head." *IEEE Tran.Biomed.Eng.* BME-43, 1996.

[Wa96] L. Walton, A. Hampshire, D. M. Forster, and A. A. Kemeny, "A phantom study to assess the accuracy of stereotactic localization, using Tl-weighted magnetic resonance imaging with the Leksell stereotactic system," *Neurosurgery* 38: pp. 170-178, 1996.

[We01] C. Welten, J. Menten, M. Feron, *et al.* "Interobserver variations in gross tumor volume delineation of brain tumors on computed tomography and impact of magnetic resonance imaging." *Radiotherapy and Oncology*, 60: pp. 39-39, 2001.

[Wo93] Wolbarst, Anthony. The Physics of Radiology. Appleton and Lange, pages used 333-334, 2001.

[Wu03] Wu X, Yu CX, DiBiasea SJ, Gullapallib R. "The application of deformable image registration for MRS in prostate treatment planning." *Int J Radiat Oncol Biol Phys.* Oct 1 57(2 Suppl): pp. 207-208, 2003.

[Xi01] Xia P., et al. "Forward or inversely planned segmental multileaf collimator IMRT and sequential tomotherapy to treat multiple dominant intraprostatic lesions of prostate cancer to 90 Gy." *Int. J. Radiat. Oncology Biol. Phys.* 51: pp. 244-254, 2001.

[Yu99] K.K.Yu , Scheidler J, Vigneron DB, et al. "Prostate cancer: Prediction of extracapsular extension with endorectal MR imaging and three-dimensional proton MR spectroscopic imaging." *Radiology* 213: pp. 481–488, 1999.

[Yu01] Cheng Yu, Zbigniew Pertovich, and Micheal L. J. Apuzzo. "An image fusion study of the geometric accuracy of magnetic resonance imaging with the Leksell stereotactic localization system." *Journal of Applied Clinical Medical Physics*, 2: pp. 1124-1136, 2001.